

Master Thesis

**Design of an H<sub>2</sub>-O<sub>2</sub> fired  
Solid Oxide Fuel Cell  
Gas Turbine Test Set Up**

Dhruv Malhotra

ME55035  
Thesis Report

**Design of an H<sub>2</sub>-O<sub>2</sub> fired Solid Oxide Fuel  
Cell-Gas Turbine test set up**

by

**Dhruv Malhotra**

to obtain the degree of Master of Science in Mechanical Engineering at the Delft University of Technology,  
to be defended on 15-11-22.

Student number: 5302315  
Thesis Committee: Prof. dr. ir. Sikke Klein TU Delft, Supervisor  
Dr. ir. Lindert van Biert TU Delft, Supervisor  
Dr. ir. M. Ramdin TU Delft

an electronic version of this thesis is available at <https://repository.tudelft.nl/>



# Abstract

The issue of climate change has fostered the innovation of new technology in an attempt to curb the rising emissions, with the energy sector being one of the biggest contributors of carbon emissions. Renewable Energy has shown promise in reducing the emissions by up to 32 %. However the problem of intermittency of renewable energy sources is still a big reason why they aren't more mainstream. Therefore, hydrogen has been seen as an energy carrier to provide integration amongst the various sectors of energy generation, transportation, household heating and industrial use. The use of hydrogen as a fuel for re-electrification and power production can be done via IC engines, gas turbines and fuel cells.

This thesis is interested in the possible applications of re-electrification of hydrogen using a system consisting of an SOFC and a gas turbine. It aims to design a small lab scale, test-setup of such a power cycle. The setup would consist of a small gas turbine and a solid oxide fuel cell.

To that end, this thesis introduces the importance of hydrogen as an energy storage medium followed by the advantages of the SOFC-GT systems in providing higher thermal efficiencies. This is followed by the introduction of the H<sub>2</sub>-O<sub>2</sub> power cycles, namely the Graz and the Toshiba cycles. From previous research done at TU Delft, a basic schematic of the system has been shown, consisting of an SOFC, a combustor, and gas turbine, heat exchangers and an ejector for re-circulative cooling of the SOFC. This is the setup that has to be designed and so the theory behind the components is presented.

Firstly, the theory behind solid oxide fuel cells, and their modelling is presented. The cooling of the SOFC has been looked into in greater detail. This is followed by the theory of combustion and turbulence modelling. Two combustor types, a swirl based and a micromix have been considered. Out of these the micromix has been chosen because of its superior mixing capabilities. Finally, the theory behind ejectors, heat exchangers and sizing of turbomachinery is presented. This concludes the theoretical background of the study.

A 0-D model of the SOFC is made based on the Sunfire/Staxera Mk-200 ISM with the 3YSZ KeraCell 11 by Kerafol. This model is then used as a basis of design for the entire thermodynamic H<sub>2</sub>-O<sub>2</sub> cycle. The designed thermodynamic cycle has an overall efficiency of 67.28 %. LHV of hydrogen.

The micromix combustor design is introduced next. A conceptual micromix geometry is presented following which, 2 different configurations are scaled and designed using the theory of jets in cross flow. The two configurations are compared after performing a CFD analysis using the  $k - \epsilon$  model with equilibrium chemistry for combustion. The comparison is based on mixing performance, pressure drop and temperature contours.

Following the design of the combustor, the supplementary components such as the heat exchangers and the ejector are designed. The turbine is selected as a small radial turbocharger with a pressure ratio of 8 and is sized using the Balje diagrams. material recommendations are given for the combustor and high- temperature heat exchangers.

The final H<sub>2</sub>-O<sub>2</sub> thermodynamic cycle is presented with the updated component designs. The final thermal efficiency is found to be 64.09 % LHV.

Finally, a basic control scheme is developed for the system and the start-up procedure is briefly discussed.

# Acknowledgements

Throughout my journey in this thesis project, I have received immense support and encouragement, and I would like to take this opportunity to thank the following people.

I would like to begin by expressing my profound gratitude towards Prof. dr. ir Sikke Klein, whose constant support, guidance and tutelage has made this research possible. I would also like to give my appreciation to Dr. ir. Lindert van Biert for always being ready to help tackle and discuss any and all questions that I had.

My heartfelt appreciation also goes out to all my friends, who have always been there for me, no matter what.

Finally, I would like to thank my parents, for without them, I would not be here today. They are the source of my strength and pride. Even though we are apart by thousands of miles, they have always shown their love and affection, boosting my morale in uncertain times and giving me the will to carry on.

*Dhruv Malhotra  
Delft, November 2022*

# Contents

<b>1</b>	<b>INTRODUCTION</b>	<b>1</b>
1.1	Background . . . . .	1
1.2	Hydrogen for Power Generation . . . . .	2
1.2.1	SOFC-GT cycles . . . . .	3
1.3	H <sub>2</sub> - O <sub>2</sub> cycles . . . . .	3
1.3.1	Research at TU Delft . . . . .	4
1.4	Description of the System To Be Designed . . . . .	6
1.5	Research Objective . . . . .	7
<b>2</b>	<b>LITERATURE STUDY</b>	<b>9</b>
2.1	Introduction . . . . .	9
2.2	SOFC Theory . . . . .	9
2.2.1	Basic Working of a Fuel Cell . . . . .	9
2.2.2	Solid Oxide Fuel cell . . . . .	10
2.2.3	Classification . . . . .	11
2.2.4	Performance . . . . .	13
2.2.5	SOFC Cooling . . . . .	14
2.2.6	Mathematical Models for designing an SOFC . . . . .	16
2.3	Combustion Theory . . . . .	16
2.3.1	Premixed and Non-Premixed Combustion . . . . .	16
2.3.2	Laminar Non-Premixed Combustion . . . . .	18
2.3.3	Turbulent Non-Premixed Combustion . . . . .	19
2.3.4	Realizable $k - \epsilon$ Turbulence Model . . . . .	22
2.4	Turbulence-Chemistry interaction . . . . .	23
2.4.1	Infinite Chemistry Model . . . . .	23
2.4.2	The Probability Density Function Modelling Approach . . . . .	24
2.5	Combustor Type for H <sub>2</sub> -O <sub>2</sub> combustion . . . . .	25
2.6	Ejector . . . . .	28
2.6.1	Basic Working . . . . .	28
2.6.2	Model type . . . . .	29
2.7	Heat exchangers . . . . .	29
2.7.1	Types . . . . .	29
2.7.2	Basic Design Procedure . . . . .	31
2.8	Turbomachinery . . . . .	32
2.8.1	Types . . . . .	32
2.9	Conclusion . . . . .	34
<b>3</b>	<b>DESIGN OF THE THERMODYNAMIC CYCLE AND ITS COMPONENTS</b>	<b>35</b>
3.1	Methodology of Approach . . . . .	35
3.2	SOFC Design . . . . .	35
3.2.1	Mass Balance . . . . .	36
3.2.2	Energy Balance . . . . .	36
3.2.3	Electrochemical Model . . . . .	36

3.2.4	Initialising parameters . . . . .	38
3.2.5	Results . . . . .	39
3.3	Thermodynamic Cycle Design . . . . .	40
3.3.1	Initialising Parameters . . . . .	42
3.3.2	Results . . . . .	42
<b>4</b>	<b>MICROMIX COMBUSTOR DESIGN</b>	<b>44</b>
4.1	Basic Requirements and Design Constraints of a Combustor . . . . .	44
4.2	Jets in Crossflow . . . . .	44
4.3	Geometry Design . . . . .	45
4.3.1	Results . . . . .	47
4.4	CFD Analysis . . . . .	49
4.4.1	Mesh Setup . . . . .	49
4.4.2	Initialising Parameters . . . . .	49
4.4.3	Results . . . . .	50
<b>5</b>	<b>DESIGN OF SUPPLEMENTARY COMPONENTS</b>	<b>55</b>
5.1	Heat exchanger Model . . . . .	55
5.1.1	Heat Exchanger Selection . . . . .	55
5.1.2	Results . . . . .	58
5.2	Ejector . . . . .	58
5.2.1	Results . . . . .	60
5.3	Turbine Sizing . . . . .	63
5.3.1	Results . . . . .	63
5.4	Material recommendations . . . . .	65
5.4.1	Combustor . . . . .	65
5.4.2	Heat Exchangers . . . . .	66
<b>6</b>	<b>SYSTEM CONTROL</b>	<b>67</b>
6.1	Updated Thermodynamic Cycle . . . . .	67
6.2	System Control Scheme . . . . .	68
<b>7</b>	<b>CONCLUSIONS AND RECOMMENDATIONS</b>	<b>70</b>
7.1	Conclusions . . . . .	70
7.2	Recommendations . . . . .	71
<b>A</b>		<b>76</b>
A.1	Finite Chemistry Model . . . . .	76
A.2	SOFC Validation . . . . .	77

# List of Figures

1.1	GHG baseline emissions - 2010-2050 [39] . . . . .	1
1.2	Re-electrification using hydrogen produced via electrolysis. The excess renewable energy is used for performing electrolysis and the produced hydrogen can then be stored or sent directly to a gas turbine for producing electricity.[45] . . . . .	2
1.3	The adapted Graz cycle by Sanz et. al[44] . . . . .	3
1.4	A schematic of the Toshiba cycle [15] . . . . .	4
1.5	Process Flow Diagram of the U-Graz Cycle [45] . . . . .	5
1.6	Process Flow Diagram of the 3 SOFC Oxy-cooled U-Graz Cycle [45] . . . . .	5
1.7	Oxy-fueled Brayton-Rankine cycle for an inland shipping vessel [13] . . . . .	6
1.8	Basic schematic of the thermodynamic cycle . . . . .	6
1.9	Basic schematic of the thermodynamic cycle with recirculative cooling . . . . .	7
2.1	Schematic Diagram of the Working of a Fuel Cell [46] . . . . .	10
2.2	Electrolyte, Anode and Metal Supported SOFCs[46] . . . . .	11
2.3	Planar SOFC [46],[29] . . . . .	12
2.4	Tubular SOFC[29] . . . . .	13
2.5	Implementation of oxygen recirculation to maintain the temperature of the SOFC . . . . .	15
2.6	A schematic of an ejector [8]. A higher outlet pressure at (7) can be generated compared to (4) by utilising a high pressure fluid at (1) . . . . .	15
2.7	Implementation of oxygen recirculation with an ejector . . . . .	15
2.8	Flame Propagation in premixed combustion . . . . .	17
2.9	Species Distribution of Non-Premixed Combustion [54] . . . . .	17
2.10	A schematic of Co-flow [60] and Counter flow [20] Non-Premixed Flames . . . . .	18
2.11	Energy Cascade in Turbulent Flows [57] . . . . .	20
2.12	Stationary Turbulence and transient turbulence [60] . . . . .	21
2.13	Overview of the Modelling Process. The flow is modelled using the RANS equations. The RANS equations are closed using the closure models, in this case the $k - \epsilon$ model. The density for the RANS equations are obtained from the reaction modelling using the infinite (fast) chemistry model. The turbulent viscosity $\mu_t$ is obtained by solving the RANS equations. This $\mu_t$ is used to solve the mixture fraction equation and complete the reaction modelling. . . . .	24
2.14	The schematic represents the probability of finding the scalar $w$ in a particular range at various locations of an fuel-oxidiser mixture [60] . . . . .	25
2.15	A swirl stabilised $H_2-O_2$ Burner developed by Tanneberger et al. at TU Berlin [54] . . . . .	26
2.16	2 Distinct flame shapes being formed at various values of steam dilution- Jet flame ( $\Omega = 4.2$ ) and Swirl Stabilised flame ( $\Omega = 7.9$ ). The contour lines on the right are lines of zero-axial velocity due to the flame swirling around the contour. $y/D$ is the normalised diameter of the flame and $x/D$ is the normalised length, where $D$ is the diameter of the combustion chamber.[54] . . . . .	26
2.17	Two micromix concepts for $H_2$ combustion developed by Dahl et al.[10]- Matrix type and two-diemnsional type . . . . .	27
2.18	A schematic of micromix combustion of hydrogen in air. the air guiding height controls the amount of air into the combustor. [16] . . . . .	27
2.19	A constant pressure type ejctor (left) and a constant area type ejector(right) [25] . . . . .	28
2.20	A basic schematic of a shell and tube heat exchanger [13] . . . . .	30
2.21	Basic schematic of a gasket plat heat exchnager [13] . . . . .	30

2.22	A welded plate heat exchanger [13]	31
2.23	Standard Temperature Diagram of a Heat exchanger	32
2.24	A basic schematic of an axial and a radial turbine. In an axial turbine, the fluid flows parallel to the axis of the rotor, whereas in a radial turbine, it flows in the radial direction.	33
2.25	A brief overview of the differences between axial and radial flow turbines[13]	33
2.26	Balje Diagram for single stage turbines. The X axis represents the specific speed $n_s$ and the Y axis represents the specific diameter $d_s$ [1]	34
3.1	PEN Structure of the SOFC	36
3.2	FC I-V characteristics [29]	38
3.3	60 cell Mk-200 SOFC on the left and the Integrated Stack Module for housing the SOFC on the right from Sunfire/Staxera [53]	38
3.4	Process flow diagram of the H <sub>2</sub> -O <sub>2</sub> thermodynamic cycle	40
3.5	Process Flow Diagram of the designed H <sub>2</sub> -O <sub>2</sub> thermodynamic cycle	43
4.1	Top view (left) of the conceptual micromix combustor geometry displaying the jet injection holes and the cross-flow injection holes. The cut section (right) of the conceptual micromix combustor geometry displaying how the fuel and oxidiser streams enter the combustor through the injection holes and mix to form steam.	45
4.2	The oxygen jet with velocity $u_j$ completely penetrates the hydrogen crossflow with velocity $u_{cf}$ . The maximum penetration $Y$ is equal to the crossflow diameter $d_{cf}$ .	46
4.3	Hole pressure loss factor vs discharge coefficient	47
4.4	Isometric view of the Micromix combustor geometries - configuration 1 (left) and configuration 2 (right)	48
4.5	Cut-section view of the Micromix combustor geometries - configuration 1 (left) and configuration 2 (right)	48
4.6	Mesh-configuration 1	50
4.7	Mesh-configuration 2	50
4.8	Contours of Velocity - configuration 1(left) and configuration 2(right). configuration 1 has higher velocities through the injection holes as compared to configuration 2.	51
4.9	Contours of Mixture Fraction- configuration 1(left) and configuration 2(right). configuration 1 has some unmixed oxygen near the walls due to the deflection of the oxygen jet. This is not present in configuration 2	52
4.10	Mean mixture fraction vs axial position - configuration 1	52
4.11	Mean mixture fraction vs axial position - configuration 2	53
4.12	Contours of Temperature - configuration 1(left) and configuration 2(right). configuration 1 has jets placed near the combustor walls while configuration 2 has centrally mounted jets.	53
5.1	Evaporating unit 1 in the O <sub>2</sub> re-circulation loop	55
5.2	Evaporating Unit 2 downstream of the turbine (top) and condensing unit downstream of the turbine (bottom)	56
5.3	Constant Pressure Mixing type Ejector	59
5.4	Inlet Isentropic Mach Number vs Suction Pressure	61
5.5	Isentropic Inlet mach number vs Outlet pressure and outlet temperature	61
5.6	Design curves for an industrial Ejector curves[12]	62
5.7	Specific Speed vs Shaft Speed plot made in the $N_s$ range 0.1-1	64
5.8	Bosal P4 Plate Heat Exchanger [4]	66
6.1	Updated Process Flow Diagram of the designed H <sub>2</sub> -O <sub>2</sub> thermodynamic cycle	67
6.2	Highlighted areas of control in the Process Flow Diagram	68
6.3	Basic instrumentation diagram of the H <sub>2</sub> -O <sub>2</sub> thermodynamic cycle	69
A.1	SOFC I-V curves - pressure variation at a constant temperature. The experimental curves are marked <i>exp</i> and the modelled curves are marked <i>mod</i> .	78



A.2 SOFC I-V curves - temperature variation for a constant pressure. The experimental curves are marked *exp* and the modelled curves are marked *mod*. . . . . 79

# List of Tables

2.1	Comparison between various types of Heat Exchangers . . . . .	31
3.1	Inlet Parameters obtained from [2] . . . . .	39
3.2	Assumed inlet Parameters . . . . .	39
3.3	Results of the H <sub>2</sub> -O <sub>2</sub> thermodynamic cycle . . . . .	40
3.4	Parameters for initialising the design of the H <sub>2</sub> -O <sub>2</sub> thermodynamic cycle . . . . .	42
3.5	Results of the designed H <sub>2</sub> -O <sub>2</sub> thermodynamic cycle . . . . .	43
4.1	Geometric and Inlet parameters of the designed H <sub>2</sub> -O <sub>2</sub> micromix combustor . . . . .	49
4.2	Input conditions for the combustor . . . . .	49
4.3	Mesh statistics of updated geometry . . . . .	50
4.4	Total pressure drop across configuration 1 and 2 for hydrogen and oxygen . . . . .	51
5.1	Design specifications of the plate heat exchangers in the O <sub>2</sub> recirculation loop . . . . .	58
5.2	Design specifications of the plate heat exchangers upstream of the turbine . . . . .	58
5.3	Combined area and pressure drop of the heat exchangers . . . . .	58
5.4	Inlet parameters used for designing the ejector . . . . .	60
5.5	Ejector design results . . . . .	62
5.6	Inlet values of turbine . . . . .	63
5.7	Comparison of all possible shaft diameters and powers . . . . .	64
5.8	Results of Turbine Design . . . . .	65
5.9	Comparitive properties of HS188 and Hastelloy X . . . . .	65
6.1	Assumptions taken while designing the thermodynamic H <sub>2</sub> -O <sub>2</sub> cycle . . . . .	67
6.2	Results of the updated H <sub>2</sub> -O <sub>2</sub> thermodynamic cycle . . . . .	68
A.1	Input values for the 0-D model . . . . .	77

# Nomenclature

## Abbreviations

<i>ARSM</i>	Algebraic Reynolds Stress Models
<i>BPHE</i>	Brazed Plate Heat Exchanger
<i>CCGT</i>	Combined Cycle Gas Turbine
<i>CFD</i>	Computational Fluid Dynamics
<i>DNS</i>	Direct Numerical Simulation
<i>DRSM</i>	Differential Reynolds Stress Models
<i>EVM</i>	Eddy Viscosity Models
<i>FAR</i>	Fuel-Air Ratio
<i>FCV</i>	Flow control valve
<i>GHG</i>	Green house gasses
<i>GPHE</i>	Gasket Plate Heat Exchanger
<i>GT</i>	Gas turbines
<i>HEX</i>	Heat Exchanger
<i>HPT</i>	High Pressure turbine
<i>HRSR</i>	Heat recovery steam generator
<i>HTT</i>	High temperature turbine
<i>HVAC</i>	Heating, Ventilation and Air-Conditioning
<i>LES</i>	Large Eddy Simulation
<i>LHV</i>	Lower Heating Value
<i>LMTD</i>	Log Mean Temperature Difference
<i>LPT</i>	Low Pressure turbine
<i>MWI</i>	Modified Wobbe Index
<i>PCV</i>	Pressure control valve
<i>PDF</i>	Probability Density Function
<i>PEN</i>	Positive-Electrode-Negative
<i>RANS</i>	Reynolds Averaged Navier-Stokes Equations

*SOFC* Solid oxide fuel cell  
*STHE* Shell and Tube Heat Exchanger  
*STP* Standard Temperature Pressure  
*TIT* Turbine inlet temperature  
*UNEP* United Nations Environment Program  
*WPHE* Welded Plate Heat Exchanger

### **Subscripts**

*ad* adiabatic  
*cf* crossflow  
*ch* channel  
*char* characteristic  
*cond* condenser  
*cr* critical  
*d* diffuser  
*eq* equivalent  
*evap* evaporator  
*i* inner  
*jet* jet  
*l* liquid  
*n* nozzle  
*o* outer  
*pl* plate  
*sat* saturation  
*w* at wall  
*act* activation losses  
*a* for anode  
*cell* pertaining to cell in SOFC  
*c* for cathode  
*diff* diffusion losses  
*ohm* ohmic losses

### **Symbols**

$\alpha$  Charge transfer coefficient  
 $\chi$  Scalar dissipation rate

$D_s$	Impeller diameter
$\Delta G$	Gibbs free energy of the reaction
$\Delta H_f$	Enthalpy of reaction
$\Delta Q$	Duty or heat load
$\Delta T_{lm}$	Log mean temperature difference
$\delta$	Thickness of electrode
$\delta$	Thickness
$\varepsilon$	Rate of dissipation of Turbulent Kinetic Energy
$\eta$	efficiency
$\eta_{LHV}$	Thermal efficiency for LHV of fuel
$\gamma$	Ratio of specific heats
$\gamma_a$	Pre-exponential factor/fit coefficient (anode)
$\gamma_c$	Pre-exponential factor/fit coefficient (cathode)
$\kappa$	Electrical conductivity
$\lambda$	Thermal conductivity
$\mu$	Dynamic viscosity of the flow
$\mu_t$	Turbulent viscosity term
$\Omega$	Angular velocity
$\omega$	Entrainment ratio
$\phi$	Chevron angle
$\rho$	Density of the fluid
$\sigma_\varepsilon$	Turbulent prandtl number for Turbulent dissipation rate
$\sigma_k$	Turbulent prandtl number for Turbulent KE
$\theta$	Angle
$\xi$	Mixture fraction
$A$	Area of heat transfer
$AR$	Aspect ratio
$C_\mu$	a function of the strain and vorticity tensors
$C_D$	Discharge coefficient
$d$	diameter
$E_0$	Open Circuit Potential
$E_a$	Activation energy for the electrode
$E_{nernst}$	Nerst Potential

$F$	Faraday's Constant
$f$	fanning friction factor
$G$	Mass Flux
$g$	Acceleration due to gravity
$G_b$	Turbulent Kinetic Energy via bouyancy
$G_k$	Turbulent Kinetic Energy via velocity gradients
$h$	Specific Enthalpy
$h_i$	Inner film coefficient
$h_o$	Outer film coefficient
$h_{id}$	Inner fouling factor
$h_{od}$	Outer fouling factor
$j$	Current Density
$j_l$	limiting current density
$j_0$	Exchange current density for the electrode
$K$	Ratio of the jet velocity to the velocity at the inlet of the annulus
$k$	Turbulent Kinetic Energy
$L$	Length
$M$	Mach number
$n$	Number of electrons
$P$	Power
$p$	Partial pressure
$Pr$	Prandtl number
$Q$	Heat extracted
$q$	charge
$R$	Cross jet momentum ratio
$r$	resistance
$Re$	Reynolds's number
$S$	Number of elements
$s_l$	Velocity of the flame
$T$	Temperature
$t$	Time
$u$	Flow velocity
$U_0$	Overall heat transfer coefficient

$V$	Cell voltage
$w$	Mass proportion of the element in the species
$W_t$	Wall thickness
$x$	Quality
$Y$	Penetration depth
$Z$	Elemental fraction

# Chapter 1

## INTRODUCTION

### 1.1 Background

A critical problem being faced by society is that of Climate Change. According to the OECD Environmental Outlook to 2050 report, the dangers of unchecked climate change include, but are not limited to, threat to water, food, health, land, natural capital and physical capital [39]. The main cause for this climate change has been attributed to the rising emissions of Green House Gases (GHGs). According to the report [39] an 80 % increase in global energy demand is predicted by 2050 which will cause an increase in 50 % more GHG emissions. Out of this 50 %, 70 % will be caused due to increase in CO<sub>2</sub> levels from energy use. A plot of the rising emissions can be seen in Figure 1.1.

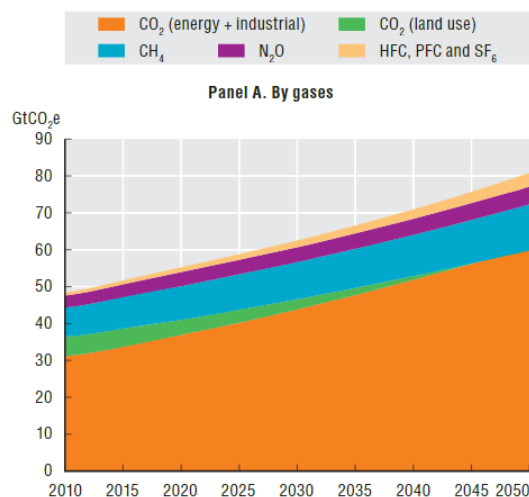


Figure 1.1: GHG baseline emissions - 2010-2050 [39]

The report further claims that if stricter control on GHG and CO<sub>2</sub> emissions is not applied then the average global temperature increase will be 3 to 6 °C higher than pre-industrial levels by the end of the century. This is much higher than the maximum 2 °C rise set by the Paris Agreement in 2015 [37].

Similarly, the Climate Change Report-2014 [40] states that the energy sector was the biggest contributor to GHGs in the year 2010 at 35 %. In 2020, Fawzy et al. [14] stated that according to the United Nations Environment Program (UNEP) in 2018, 37.5 GtCO<sub>2</sub> out of 55.3 GtCO<sub>2</sub> (roughly 68 %), was from the use of fossil fuels for energy generation and industrial activities. These worrying trends indicate the immediate need for the de-carbonisation of the energy sector.

According to Brandon et al. [7] the International Energy Agency suggests that Renewable energy will be the second largest contributor to CO<sub>2</sub> reductions at 32 %, preceded only by efficiency improvements at 38 %. However, one of the major shortcomings of Renewable Energy has been its intermittency. This is because



solar and wind energy are not available consistently everywhere, year round. Therefore, in times of excessive production, this energy must be stored somewhere so that it can be used again in times of inhibited production.

## 1.2 Hydrogen for Power Generation

To solve the issue of intermittency of renewable energy, Maggio et al. [36] note that hydrogen can be a key player in transforming the fossil fuel based energy sector to a renewable energy based sector. The excess energy generated can be used for electrolysis resulting in the formation of hydrogen. In this way, hydrogen can be used as a medium for long term storage of energy [36]. This stored hydrogen could then be transported and used for power generation. The power generation can be done via fuel cells, IC Engines, Diesel Generators or gas turbines [7]. The following schematic illustrates by Schouten et al. illustrates this concept in the case of a gas turbine.

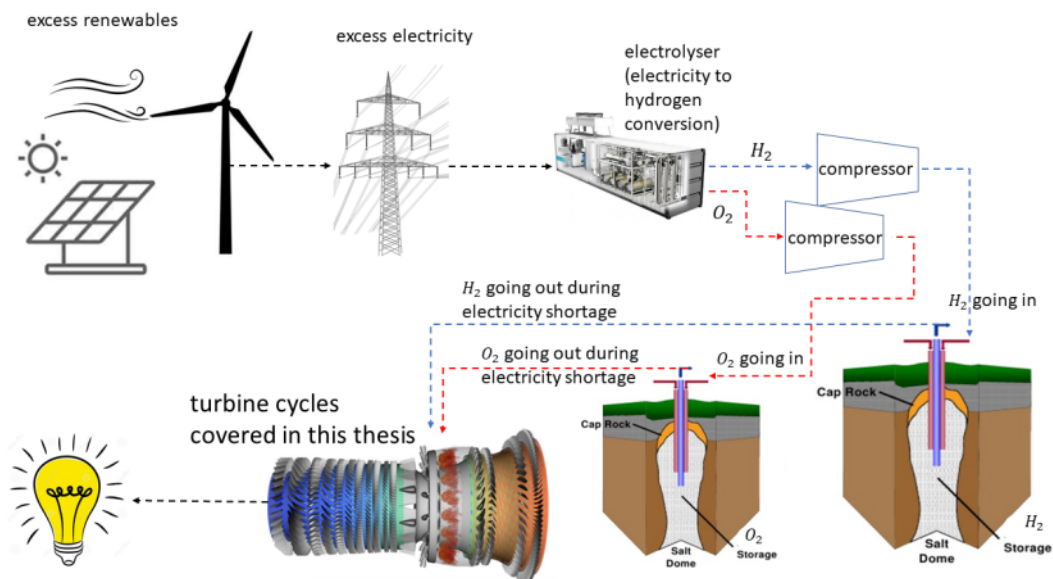


Figure 1.2: Re-electrification using hydrogen produced via electrolysis. The excess renewable energy is used for performing electrolysis and the produced hydrogen can then be stored or sent directly to a gas turbine for producing electricity.[45]

Since hydrogen is carbon neutral, it has the potential of becoming a clean fuel. It possesses a very high gravimetric energy density (energy /mass) and wide flammability limits[30]. The major drawback is the low volumetric energy density (energy/volume) and a low boiling point, thus requiring large, insulated tanks for storage and transportation [30].

Using hydrogen in gas turbines instead of fossil fuels can have several advantages, other than lowering CO emissions. According to Haque et al. [21], the fuel flexibility of a gas turbine depends on several factors such as fuel type and composition, oxidiser type and composition, flame stabilisation, loading condition and the Modified Wobbe Index (MWI). Hydrogen enriched fuels showed a higher Lower Heating Value (LHV) for the same MWI. This effectively means that a hydrocarbon based fuel can be simply replaced with a hydrogen enriched fuel having the same MWI, but a higher LHV. Thus they indicate greater fuel flexibility as compared to hydrocarbon Based fuels [21]. In this way, fuel flexible gas turbines can pave the way for de-carbonisation of energy production.

A report by ETN Global [58] highlights various companies that already have gas turbines running on H<sub>2</sub> blended fuels and are reporting lower carbon and NO<sub>x</sub> emissions. This is being done by redesigning and retrofitting combustors. The report further highlights that the scalable nature of GTs could also pave the way for decentralised power generation systems. [58][3].

### 1.2.1 SOFC-GT cycles

As noted by Brandon et al.[7], amongst the many ways of power generation using hydrogen, one way is by using fuel cells. Fuel cells generate electricity due to the oxidation-reduction or redox reactions occurring between the fuel and oxidiser. Depending upon the type of fuel cell, the efficiency occurs in the range of 40 to 90 % [47]. Furthermore, the integration of fuel cells and gas turbines is an interesting concept and has gained significant attention since the development of the Solid Oxide Fuel Cells (SOFC). These SOFCs require high temperatures to run since the electrolyte they use is a solid and only becomes conductive at high temperatures. Typically in these SOFCs, around 65 % LHV of the fuel gets converted [36] to electricity while the remaining 35 % of the energy is released as heat in the exhaust streams. These high temperature exhaust streams can be used to run a Gas Turbine.

One evaluation of the SOFC-GT concept by Bohn et al.[3] states that this system has the potential to reach a thermal efficiency of 75 %. This is much higher compared to a state of the art Combined Cycle Gas Turbine which only goes upto 65 % [61]. The reason for this can be attributed to the fact that a GT cycle has the highest exergy losses in the combustion chamber. If an SOFC can utilise the heat of the fuel upstream of the combustor then the cycle efficiency will increase. Since the fuel utilisation in an SOFC is in the range of 85 to 90 % [46], the remaining fuel that can be burned inside a combustor downstream.

The first proof of concept of the SOFC-GT system was built in 2002 by Siemens Westinghouse [22], with an SOFC and a Micro Gas Turbine. The system had an overall output of 220 kW, with 200kW coming from the SOFC and 20 kW coming from the Micro Gas Turbine. The overall efficiency of the system was 55 % [3]. Despite the zero carbon emission, NO<sub>x</sub> emissions are still a prevalent issue in such systems. Therefore one way to make Gas Turbines completely emission free is by using pure oxygen instead of air.

Therefore an oxy-fuel cycle, combined with the SOFC can lead to a system which is carbon neutral, NO<sub>x</sub> free and highly efficient.

### 1.3 H<sub>2</sub> - O<sub>2</sub> cycles

The most well known H<sub>2</sub> - O<sub>2</sub> cycles currently present are the Graz cycle [26] and the Toshiba cycle [15]. The Graz cycle consists of a high temperature Brayton cycle coupled with a low temperature Rankine cycle. In essence, it is similar to a conventional CCGT system. This cycle has been adapted for burning H<sub>2</sub> and O<sub>2</sub> by Sanz et al. [44] since it originally burned natural gas with oxygen [26]. This adapted cycle is shown below.

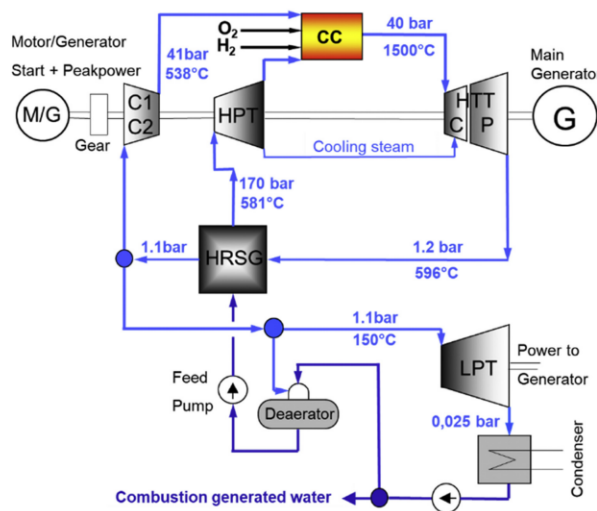


Figure 1.3: The adapted Graz cycle by Sanz et. al [44]

Hydrogen and oxygen are sent to the combustor where they are burnt to form high temperature steam. This steam expands in the high temperature turbine and the exhaust is then sent to a HRSG. From here, the steam is

split into 2 parts, one goes to the compressor, where it is compressed and sent to the combustor to cool it and the other goes to a low pressure turbine, where it expands and is then condensed. The condensate is then sent back to the HRSG where it is heated and sent to a HPT, thus closing the loop. The cycle reaches a maximum thermal efficiency of 70.35 % LHV [44].

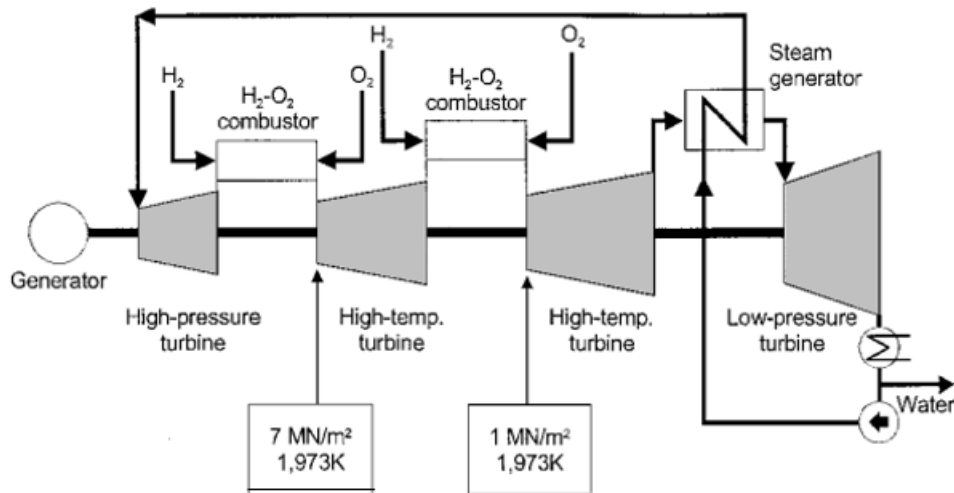


Figure 1.4: A schematic of the Toshiba cycle [15]

The Toshiba cycle developed by Fukuda et al.[15] consists of 2 high temperature turbines and 2 combustors arranged in an alternating order as shown in Figure 1.4. The hydrogen and oxygen are burnt in the first combustor and the steam is expanded in the first turbine. Then the steam is reheated and sent to the second turbine. The exhaust of the second turbine is sent to a HRSG where it is used to produce more steam by boiling water. The steam is then sent to a LPT and at its exit is condensed. The condensate is pumped back to the HRSG, where it boils to form steam, which is then expanded in a HPT and sent to the combustors, thus closing the loop. The cycle reaches a maximum thermal efficiency of 61.7 % HHV equaling 72.9 % LHV[15],[45].

### 1.3.1 Research at TU Delft

Schouten et al.[45] worked on improving the existing oxy-fuel cycles. An exergy analysis was used to compare both the Graz and the Toshiba cycles, in order to choose a cycle to work on. The Graz cycle was chosen and improved to achieve an efficiency of 74.9 %. Then, by performing another exergy analysis on the improved Graz cycle, the effects of addition of an SOFC were investigated and the ideal location was found to be upstream of the combustor. This result was a 3.2 % increase in the efficiency of the cycles due to the compensation of the exergy loss in the combustor, since most of the fuel being was used in the SOFC. Four variants of the U-Graz cycle were made, namely; U-Graz with 1 SOFC (steam cooled), U-Graz with 3 SOFCs (steam cooled), U-Graz with 1 SOFC (oxygen cooled) and a U-Graz with 3 SOFCs (oxygen cooled). The 3 SOFCs were placed in series as shown in Figure 1.6.

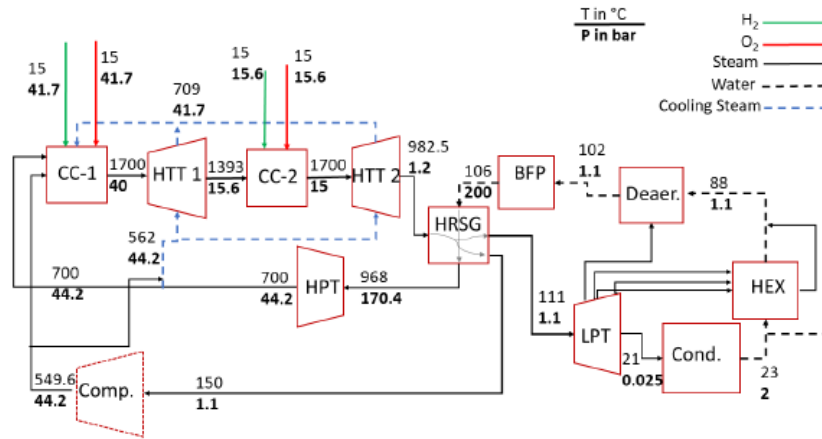


Figure 1.5: Process Flow Diagram of the U-Graz Cycle [45]

Between the cooling of the SOFC with steam re-circulation vs oxygen re-circulation, it was found that oxygen re-circulation was superior in terms efficiency, power density and overall simplicity of the cycle. Also, the issue of dealing with the formation of mixtures of oxygen and steam in the SOFC, is avoided for oxygen cooling (Section 2.2.5 for further details). Additionally, the 3-SOFC U-Graz cycle with oxygen cooling proved to have an efficiency of 83.8 %.

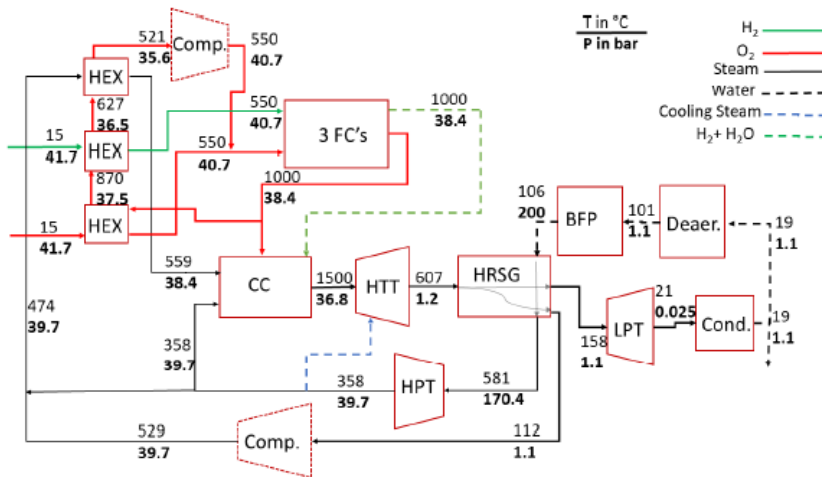


Figure 1.6: Process Flow Diagram of the 3 SOFC Oxy-cooled U-Graz Cycle [45]

Evertse's [13] contribution was the design of an SOFC integrated, oxy-fueled CCGT, where the Brayton and Rankine cycles were coupled via a single pressure heat recovery steam generator (HRSG). The design of the basic thermodynamic cycle is shown in Figure 2.16. This cycle was meant for running an inland shipping vessel with a power output of 3 MW. The exergetic efficiency of the basic design was calculated at 73.09 % and thermal efficiency of 71.79 %. To further improve the efficiency, the HRSG of the cycle was improved by an exergy analysis and the cycle was redesigned. The efficiency was increased to 73.47 %. Additionally, a preliminary design and sizing of the main components of the cycle was done. These included the compressor, HTT, HPT, the heat exchangers and the SOFC.

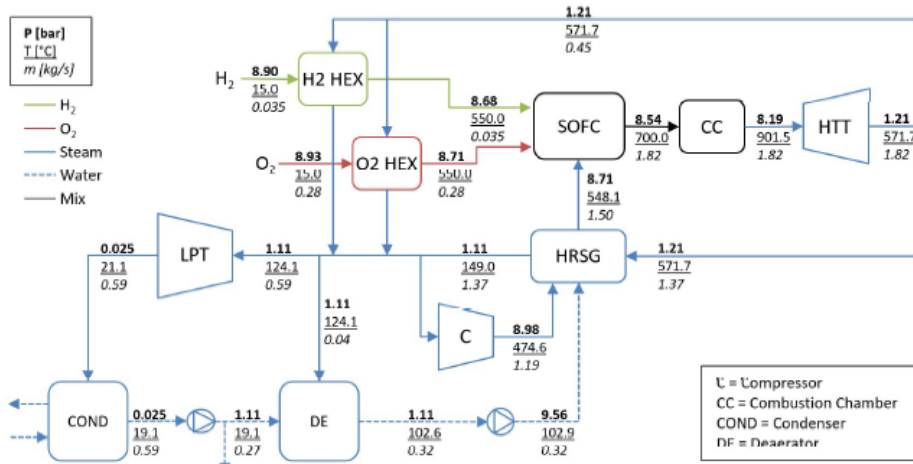


Figure 1.7: Oxy-fueled Brayton-Rankine cycle for an inland shipping vessel [13]

## 1.4 Description of the System To Be Designed

The goal of this thesis is to **design a lab scale test set up, consisting of an integrated hydrogen-oxygen fired SOFC-GT Cycle**. Based on the work by Schouten et al.[45] and Evertse et al [13], the basic layout of the thermodynamic cycle and the main components can be determined. This is shown in the basic schematic in Figure 1.8.

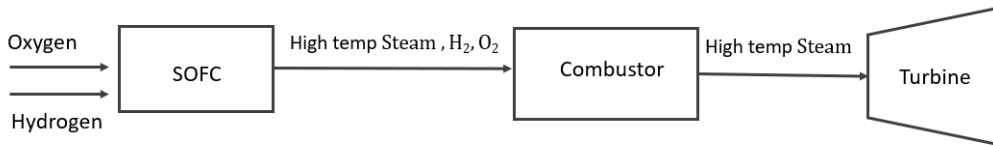


Figure 1.8: Basic schematic of the thermodynamic cycle

- The SOFC: The SOFC generates electricity using hydrogen as fuel and oxygen as the oxidiser. It provides high temperature streams to the combustion chamber. These high temperature exhaust streams go to the combustor.
- The combustor: The combustor acts as an afterburner to utilise the hydrogen fuel in the outlet streams of the SOFC. These streams enter the turbine at the required Turbine Inlet Temperature.
- The heat exchangers: The Heat Exchanger is useful for the thermal management and proper heat distribution throughout the cycle.
- The turbine: Produces power from the exhaust gasses.

Further, to cool the Solid oxide Fuel Cell, a recirculative loop of oxygen cooling can be employed. This is based on the findings of Schouten et al. al[45] as noted previously in Section 1.3 and further expanded on in Section 2.2.5. This cycle is shown in Figure 1.9.

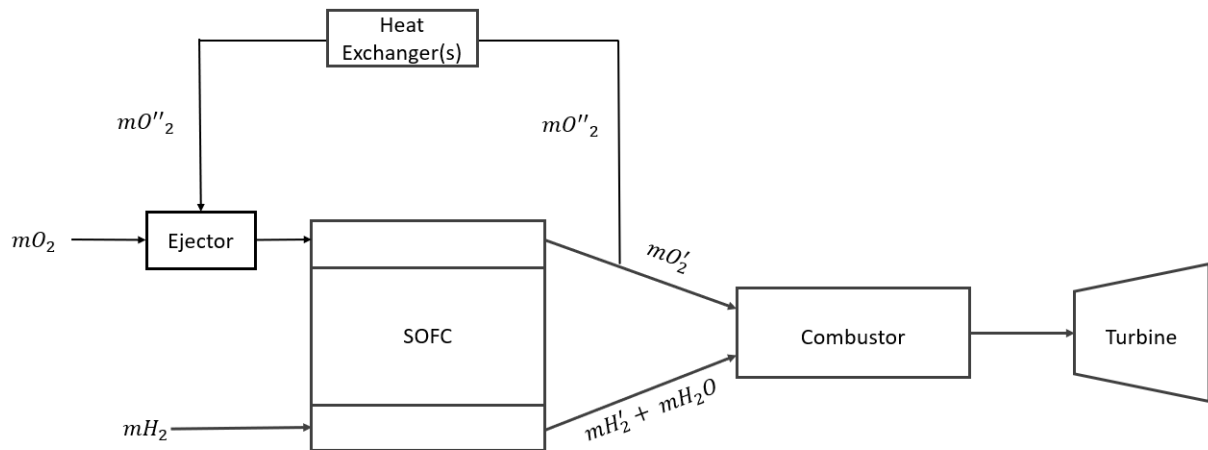


Figure 1.9: Basic schematic of the thermodynamic cycle with recirculative cooling

## 1.5 Research Objective

As stated earlier, the goal of this thesis is to **design a lab scale test set up, consisting of an integrated hydrogen-oxygen fired SOFC-GT Cycle**. By doing so, it aims to lay the technical foundations of a fully functioning lab test set up in TU Delft in the near future.

The research question of this thesis is:

**How can we make an overall basic design of the hot section of the H<sub>2</sub>-O<sub>2</sub> fired SOFC-GT lab scale test set up ?**

Further sub-questions are:

- How can we technically realise the oxygen re-circulation loop for the SOFC ?
- How can a basic H<sub>2</sub>-O<sub>2</sub> combustor be designed for this cycle ?
- How can such a system be controlled?

The report outline is as follows:

- **Chapter 2: LITERATURE STUDY:** This chapter presents the basic working, construction, types, performance and cooling of solid oxide fuel cells, followed by the types of mathematical models used to design them. The chapter continues with the basics of combustion, basics of turbulence and selection of combustors for H<sub>2</sub>-O<sub>2</sub> combustion. The chapter also elaborates on the working of the ejector (for recirculative cooling), types of heat exchangers and the basics of turbomachinery. The chapter concludes with a summary of the important design choices made during the literature review.
- **Chapter 3: DESIGN OF THE THERMODYNAMIC CYCLE AND ITS COMPONENTS:** This chapter introduces the design procedure and various mathematical equations used for designing the SOFC and the thermodynamic cycle, followed by their results.
- **Chapter 4: MICROMIX COMBUSTOR DESIGN:** This chapter deals with the design of a micromix type H<sub>2</sub>-O<sub>2</sub> combustor. Two configurations are designed and compared by performing a simple CFD simulation.
- **Chapter 5: DESIGN OF SUPPLEMENTARY COMPONENTS:** This chapter contains the design procedures followed for the design of the heat exchangers, ejector and the turbine.

- **Chapter 6: SYSTEM CONTROL:** This chapter introduces the final updated thermodynamic cycle. This is followed by a simple description of how the system can be controlled during start-up followed by a simple control scheme and a basic instrumentation diagram of the system.
- **Chapter 7: CONCLUSIONS AND RECOMMENDATIONS:** Contains the conclusions of the research followed by recommendations based on the current research.

# Chapter 2

## LITERATURE STUDY

### 2.1 Introduction

This chapter introduces the literature studied regarding the theory and selection of mathematical models for designing the various components outlined in the previous chapter in Fig 1.9.

### 2.2 SOFC Theory

A fuel cell is a device capable of generating electrical energy through electrochemical reactions between the fuel and the oxidiser. This process is similar to a battery, the major difference being that a battery has a fixed internal storage of the fuel and oxidiser, but a fuel cell has a continuous supply of the fuel and oxidiser. This is quite clear in the original name given to the device by its inventor as a 'Gas Battery', as stated by Sharaf et al in [47].

The major advantage of a fuel cell is that it is not limited by the Carnot efficiency since it is not a heat engine. Additionally, since no combustion is involved, it generates power with the only emission being steam (if only hydrogen and oxygen are given as inlets). These advantages have sparked a great interest in the research on fuel cells as a device for generation of clean energy.

#### 2.2.1 Basic Working of a Fuel Cell

The basic working of a fuel cell can be explained by its three main components: the anode (fuel electrode), the cathode (oxidiser electrode) and the electrolyte. The fuel is oxidised at the anode, leading to the release of electrons, that travel through the load over to the cathode. This is where the electrons reduce the oxidiser, leading to the formation of an anion that travels back to the anode, where it oxidises more fuel and forms a continuous loop as is shown in Figure 2.1.



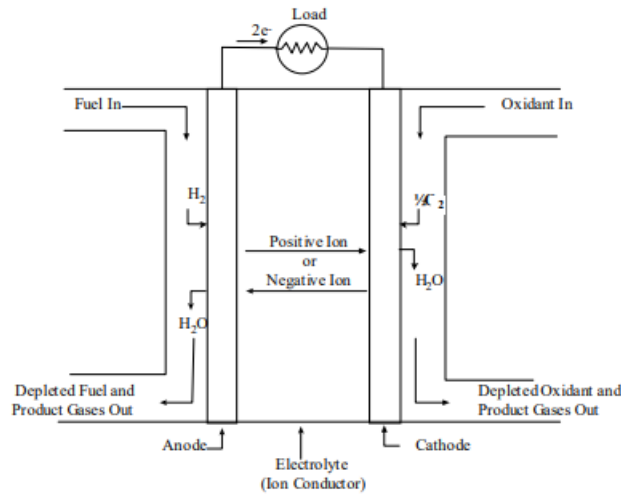


Figure 2.1: Schematic Diagram of the Working of a Fuel Cell [46]

This happens due to the spontaneous nature of the Redox reactions that occur at the electrode-electrolyte interface, making the Fuel Cell a Galvanic Cell. Thermodynamics attributes this behavior to the negative Gibbs free energy of the reactions. Since the potential of these reactions is positive, the Gibbs free energy is negative owing to Equation 2.1

$$\Delta G = -nFE_0 \quad (2.1)$$

where  $\Delta G$  is Gibbs free energy of the reaction,  $n$  is number of electrons,  $F$  is Faraday's Constant and  $E_0$  is the Reversible Open Circuit Voltage. Thus the reactions are spontaneous.

Though the fuel cell does not suffer from the limitations of the Carnot Efficiency, it is still not 100 % efficient. The reason for this is the heat generated during the reaction. The enthalpy of the reaction ( $\Delta H_f$ ) is the maximum amount of heat that can be generated from the combustion of the reactants. However, since no combustion is taking place inside the fuel cell, the maximum available energy is the Gibbs Energy of the reaction ( $\Delta G$ ) at that temperature. Thus the maximum efficiency of the fuel cell is defined in terms of the maximum available enthalpy as follows:

$$\eta = \frac{\Delta G}{\Delta H_f} \quad (2.2)$$

Reported values of the efficiency of the fuel cell vary between various types of fuel cells. The overall range encompassing all values is 40-90 %.[47]

### 2.2.2 Solid Oxide Fuel cell

A solid Oxide fuel cell is a complete solid state device that uses a ceramic material that conducts the oxide ion, as an electrolyte. Due to this, only the gaseous and solid phases exist in an SOFC. This makes it simpler in construction than the other types of fuel cells [29].

The operating range of the SOFC is usually 600 to 1000 °C, since the solid electrolyte becomes conductive for oxygen ions above that temperature [46]. The high temperature operation, possible due to the solid nature of the electrolyte allows the SOFC to be applied to hybrid systems containing gas turbines in order to use the heat contained in the exhaust gasses.

Therefore the exit composition, flow rates, pressure and temperature of the products are important parameters that need to be calculated so as to be able to design the combustor downstream. The SOFC of concern has the

following reactions:



The oxygen entering the cathode gets reduced to form the  $O^{2-}$  ion which then travels through the electrolyte to oxidise the  $H_2$  to form water and 2 electrons. These 2 electrons travel through the load connected outside and to the other side to reduce more oxygen ions to form  $O^{2-}$  ions, thus completing the loop.

### 2.2.3 Classification

The SOFC can be classified according to the following two criteria:

#### Based on Construction

- High Temperature SOFC (Electrolyte Supported SOFC):  
The high temperature SOFC is the design in which the electrolyte layer is also the load bearing layer of the PEN (Positive Electrode-Electrolyte-Negative Electrode) structure. This has been the traditional design for the SOFC. The electrolyte layer is thicker than the anode and cathode. This leads to a higher ohmic resistance. Therefore a higher operating temperature is required in order to achieve the required amount of mass transport for the  $O^{2-}$  ions. The minimum operating temperature for this type of SOFC is 800 °C.
- Intermediate Temperature SOFC (Anode Supported SOFC):  
These SOFCs have a thinner electrolyte layer which leads to lower operating temperatures. Thus, in some designs the anode is made the load bearing layer and hence it is the thickest. This also allows for using cheaper materials. The operating range of these cells is between 650-800 °C.
- Low Temperature SOFC (Metal Supported SOFC):  
These SOFCs have a porous metal substrate as the load bearing layer. The anode, electrolyte and the cathode are all deposited over this substrate as thin layers. This leads to low temperature operation and lower costs since the ceramics get replaced by a steel substrate. The challenge with this design is ensuring that the metal substrate does not rust, melt or creep. The operating range for these cells is 500-700 °C.

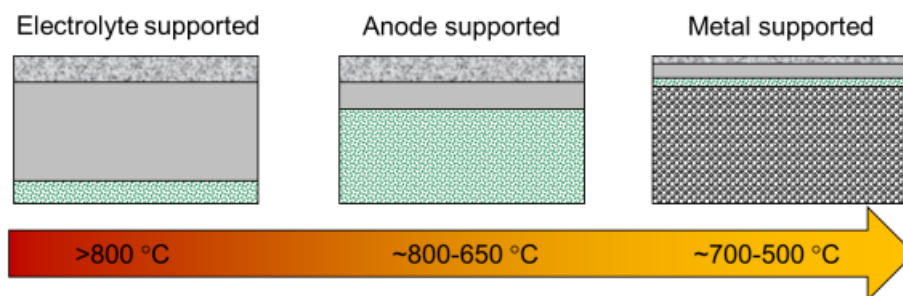


Figure 2.2: Electrolyte, Anode and Metal Supported SOFCs [46]

#### Based on geometry

The 2 most used configurations are the tubular and the planar configuration. There also exists other less common configurations such as the Bell and Spigot configuration [46] and the ring type configuration [29].

- Planar SOFC:

The planar SOFC consists of thin flat plates over which the electrochemical layers are deposited. These are separated by Bi-polar plates which allow the an electrical connection between multiple multiple cells while still keeping them separated. This separation is created so that the fuel and oxidiser gasses can be supplied to each cell and their is no crossover of gasses between the cells. The bipolar plates have gas channels on the inner side. This is called an internal manifold. This is the path that the gasses take as they travel between the sandwiched bipolar plate and the electrodes. The fuel and oxidiser can flow in a co-flow, counter-flow or a cross-flow arrangement. Here a cross-flow arrangement can be seen in figure 2.3. The planar SOFC has a higher power density than its tubular counterpart. This is due to the fact that the electrons travel a much longer distance as they have to traverse the circumference of the tubular SOFC leading to lower voltages due to higher ohmic losses. The planar SOFC is also more economical to manufacture, as compared to the Tubular SOFC. This is due to the use of the Electrochemical Vapour Deposition and Plasma spraying being used for the electrolyte and the electrodes respectively.[46].However, the planar SOFC has issues with the fabrication of flat, thin layer cells and adequate gas seals. The issue of sealing arises since the planar SOFC is open from the sides and hence the gasses can leak out of the internal manifolds. This problem is alleviated in the tubular SOFC due to its one end being closed.

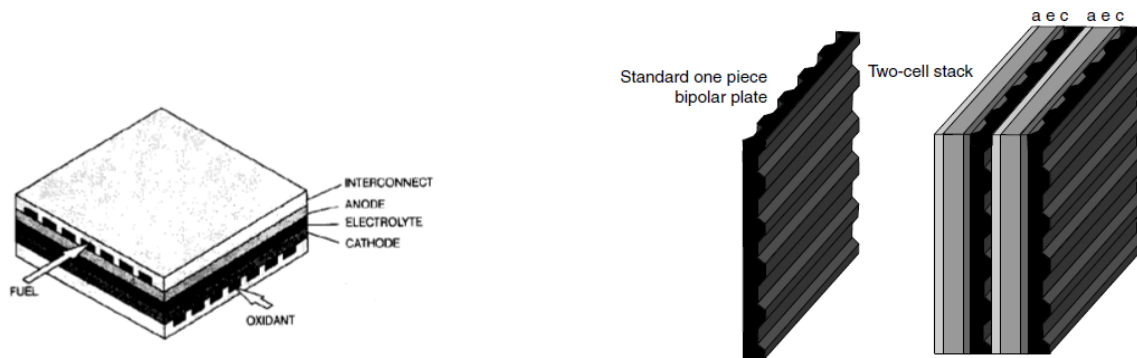


Figure 2.3: Planar SOFC [46],[29]

- Tubular SOFC:

The tubular fuel cell consists of a tubular support structure over which the electrolyte and the electrodes are deposited. It could be cathode supported, anode supported or electrolyte supported as expanded upon previously. The tubular SOFC was first designed by Seimens Westinghouse (then Westinghouse)[22] in the mid 1970s. This design had a porous support tube that was 2 mm and a length of 30 cm. This design had issues in regards to the lack of oxygen diffusion towards the cathode. This design was later improved by shifting to an Anode Supported Design and an increased length of 100 cm[41] and the current length is 150 cm [29]. The Tubular SOFC solves the problem of sealing in the Planar SOFC as its one end is closed. The basic operation of a tubular SOFC as explained in [29] and [46] is as follows: A thin tube is used to feed air into the cathode. Due to re-circulation in the SOFC, the air gets preheated to the operating temperature due to heat generated within the cell. The fuel flows over the Anode, which is the outside of the tube. Once the air passes through the closed end of the SOFC, it comes back up and then mixes with the fuel after flowing through the fuel cell back up to the open end. The fuel and air react and form steam, since the SOFC is operating at a very high temperature ( $> 800\text{ }^{\circ}\text{C}$ ). This steam also contains unreacted hydrogen. The amount of hydrogen contained depends upon the fuel utilisation of the cell. This combination of gases forms the exhaust gases which then escape out of the fuel cell manifold. The excess unreacted air escapes out of another outlet. Sometimes, depending upon the design, there may only be one exhaust. Then hydrogen, steam and air all leave as a single stream of exhaust gases as shown in Figure 2.4. A part of the excess air is recirculated to preheat the incoming air.



Figure 2.4: Tubular SOFC[29]

## 2.2.4 Performance

The performance of an SOFC or that of an SOFC stack have been extensively researched both experimentally and through models. Wilich et al. [62], Lemanski et al. [31] and Schouten et al. [45] have provided important observations regarding the behaviour of an SOFC via their models. Further, Zhou et al. [64] experiments on a pressurised SOFC have also provided important insights.

- Effect of Pressure: By increasing the pressure of the SOFC stack or even for a single cell, the power density increased. This is on account of the increased Nernst voltage for Hydrogen-Oxygenation reaction (2.6) given as follows:

$$E_{nernst} = E_0 + \frac{RT}{nF} \ln \frac{p_{H_2O}}{p_{H_2} p_{O_2}} \quad (2.6)$$

where  $E_0$  is the Open Circuit Potential as given in Equation 2.1,  $T$  is the temperature at which the reaction is occurring,  $R$  is the Universal Gas Constant,  $n$  is the number of electrons taking part in the redox reaction and  $P$  is the partial pressure.

Therefore, as the pressure increases, the partial pressures of the Hydrogen and Oxygen increase. This gives rise to a higher Nernst Potential and thus a higher Power density for a fixed temperature. Liese et al. in [5] state that pressurised SOFC-GT systems offer better efficiency as compared to un-pressurised SOFC-GT systems and a possibility of reduced cost.

- Effect of temperature: The cell voltage ( $V_{cell}$ ) increases with increasing temperature. This effect can again be understood by looking at the expression for  $V_{cell}$  in Equation 3.20. The Nernst Potential term ( $E$ ) decreases with the increasing temperature. This is because for the hydrogen oxygenation reaction, with the increase in temperature,  $\Delta G$  becomes less and less negative. Since  $\Delta G = \Delta H - T\Delta S$ , where  $\Delta H$  and  $\Delta s$  are both negative. At higher temperatures, the  $-T\Delta S$  term becomes more and more positive. Thus, the  $\Delta G$  term becomes less and less negative. Hence, from Equation 2.1, it can be seen that the Open Circuit Voltage  $E_0$  decreases and along with it the Nernst Voltage (Refer Equation 2.6). However, when the loss terms are considered, then diffusion losses term ( $V_{diff}$ ) increases with increasing temperatures because of the direct proportionality of the temperature as seen in Equation 3.19. The ohmic losses ( $V_{ohm}$ ) and the activation losses terms ( $V_{act}$ ) decrease with the increasing temperature. The ohmic losses are decreased because of the increased conductivities of the anode, electrolyte and cathode as in Equation 3.14. The activation losses are decreased due to the increased exchange current densities as in Equation 3.13. Since the ohmic loss term dominates, a decrease in it causes the total loss term to also drop. However, the losses term decreases faster than the nernst potential term. This leads to an overall increase in the cell voltage term (Refer Section 3.2.3 for all equations).

- Effect of higher concentration of reactants: The power density  $P$  increased due to higher fractions of hydrogen and oxygen. Using pure hydrogen and oxygen gave the highest power density. This again can be seen from the expression of the Nernst Potential as in Equation 2.6, where the higher partial pressures of both the reactants will give a higher output voltage.
- Effects of fuel re-circulation: Higher values of fuel utilisation gave lower voltages and subsequently lower power densities at constant temperatures. This is due to the decreasing amount of fuel present at the electrodes for a continued reaction leading to Concentration Over Potentials ( $V_{diff}$ ) as in Equation 3.19.

From these observations, it can be implied that a higher pressure and higher temperature can lead to a higher power density on account of reduced ohmic, activation and diffusion losses. This higher power density can lead to an increase in efficiency of the SOFC-GT system.

### 2.2.5 SOFC Cooling

The recirculative cooling of the SOFC was looked at with greater detail. This SOFC liberates heat due to the exothermic nature of the reaction taking place inside it. This leads to the heating up of the outlet streams to a temperature that is higher than the inlet stream. Therefore, SOFCs need to be continuously cooled in order to keep them in the operating temperature range. Operating the SOFC at a temperature out of its operating range could lead to degraded performance plus the ever present chance of thermally induced stresses arising from differential thermal expansion of the various components[46].

The SOFCs are cooled by the re-circulating gases in the internal reformer or by using excess air. In this case, since pure hydrogen and oxygen are being used, the need of a reformer is removed. Therefore, the SOFC temperature can be regulated by providing excess oxygen at the cathode. For integrating such an SOFC with a gas turbine in the envisioned  $H_2-O_2$  cycle, adding other coolants like nitrogen or carbon dioxide would not have been acceptable since these would cause the issue of emissions in the form of  $NO_x$  and CO. Therefore only oxygen and steam can be used for a hydrogen-oxygen cycle. As stated earlier in Section 1.3, this idea was explored by the previous work by Schouten et al. [45] and 2 ways of cooling were considered:

- Diluting the oxygen flow with steam: For this case, the Nernst voltage was lower, because the steam dilution causes the partial pressure of oxygen to be much less at the cathode (Equation ??). The same reason is why anode side (fuel side) cooling is not optimal. The same observation was also made by Evertse [13]. Additionally, Schouten et al. [45] noted that this cycle was more complex, since providing steam at a high pressure and temperature required a more complex Heat Exchanger network followed by limited flexibility in terms of changing parameters. Also, the complexity arose because of the mixtures of oxygen and steam in the SOFC.
- Flooding the cathode with excess oxygen: Here the effect was that the Nernst Potential was higher as compared to the steam dilution option, but an extra compressor was needed for a higher flow. Apart from a higher Nernst Potential Schouten [45] noted a higher Power Density for this method of cooling. Part of this oxygen was being recirculated through a network of Heat exchangers and fed back to the SOFC as shown in Figure 1.6.

Furthermore, Lemanski et al. [31] noted that, at higher oxidiser utilisation ratios, the efficiency of the SOFC dropped for a fixed fuel utilisation. This is because, the increase in air (or in this case oxygen) utilisation demands the increase in fuel utilisation. Stoichiometrically, the amount of oxygen required for the reaction is only half the amount of hydrogen required as in Equation 2.1. Therefore, the excess oxygen can very well be used for maintaining the temperature difference of the SOFC. Additionally, the oxygen stream will be preheated before entering the SOFC. This method of cathode gas recirculation has shown to increase efficiency in SOFC-GT cycles as shown by Chen et al. [8]. Plus, re-circulation would give the added advantage of being able to closely control the amount of oxygen entering and leaving the SOFC. This would give greater control over the amount of oxygen entering the combustor downstream. This system is shown in Figure 2.5.

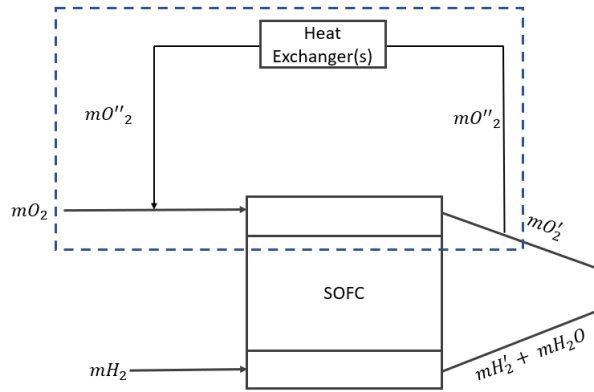


Figure 2.5: Implementation of oxygen recirculation to maintain the temperature of the SOFC

This can be done by using an ejector. An ejector works by suction. The hot gas flows into the convergent divergent nozzle at a high pressure and it is accelerated through the nozzle. Due to this acceleration, at the outlet of the nozzle, a pressure drop occurs which causes the creation of a suction pressure at the bottom of the ejector. This pulls in fresh fluid from the bottom. The fresh cold fluid and the hot fluid mix in the mixing section. An ejector is shown in Figure 2.6.

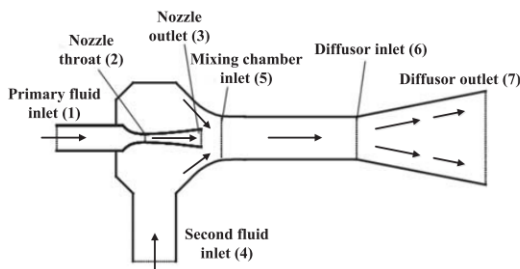


Figure 2.6: A schematic of an ejector [8]. A higher outlet pressure at (7) can be generated compared to (4) by utilising a high pressure fluid at (1)

By using the ejector, the need for a compressor could be removed. An additional temperature drop can be obtained by using a heat exchanger, if needed. Further, the mixing of the inlet and the recirculated stream can take place within the ejector itself. This would also be beneficial in-terms of cost and size. The is system is shown in Figure 2.7.

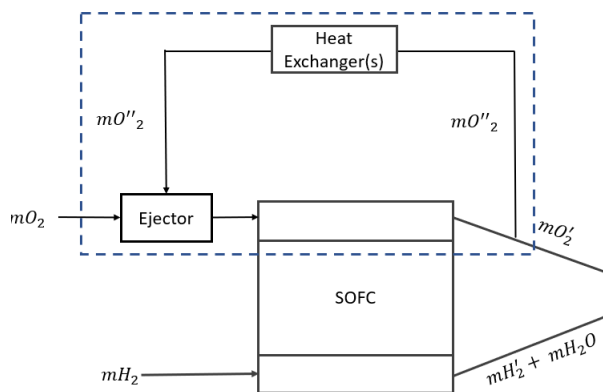


Figure 2.7: Implementation of oxygen recirculation with an ejector

## 2.2.6 Mathematical Models for designing an SOFC

One of the major portions of this project deals with designing the SOFC. This section provides a basic overview of the various mathematical models used for designing an SOFC in literature.

Based on complexity, the SOFC models can be categorised as:

- 0-D model: A 0-D model forms the stack part of the system level model which consists of all the subsystems along with the stack such as compressors, heat exchangers, blowers pumps etc [6]. A 0-D model can best be described as a 'black box'. The electrochemistry and the structure are all fixed at a single point and do not vary spatially. Therefore, the only point of concern is how the incoming reactants (inputs) get transformed into the products (outputs) through the spatially invariant equations of the electrochemical model.
- Cell Level Models : Cell level models are concerned with the behaviour of individual cells. The governing equations for such models are the mass, momentum, energy and charge transport equations. Depending on how many dimensions are chosen, there are 1-D models, 2-D models and 3-D models. These models can be used to study the electrochemistry, the thermal management, the transport of mass and charges, the internal reforming etc. depending upon the goal of the problem. [6]
- Stack-Level Models: Stack level Models are used to model the behaviour of several cells connected in a stack. Therefore they are essentially used to determine the optimum geometry and manufacturability with constraints such as the materials used and the configuration for the cells. They are usually modelled using commercial CFD packages.[6]
- Micromodels: Micromodels are concerned with the electrochemistry occurring at the atomistic or molecular scale.

All the models can be steady state or transient. A transient model should be selected if one wishes to capture transient phenomena such as mass and energy transport variations during start-up and shutdown. If one wishes to study the time invariant operation during continuous operation for a given length of time, then the steady state model should be selected.

For the purposes of this thesis, a 0-D model has been chosen to model the fuel cell. This is because, the internal variations of the thermodynamic and electrochemical parameters are not known to significantly affect the stack performance on the system level[63]. Since the integration of the fuel cell with the combustor and the other components of the cycle is of prime importance here, this is a system level model. Therefore, for the sake of simplicity the internal variation of the thermodynamic and electrochemical parameters can be ignored as their study is not the prime objective here.

As stated in Section 2.2.2 the exit composition, flow rates, pressures and temperature of the products will form the boundary conditions of the combustor and the other system components. A 0-D model can be used to calculate these values with acceptable accuracy while keeping the computation time less.

## 2.3 Combustion Theory

The current section discusses the basics of combustion, the basics of turbulence and a brief overview of combustors suitable for H<sub>2</sub>-O<sub>2</sub> combustion.

### 2.3.1 Premixed and Non-Premixed Combustion

Combustion can be simply defined as the burning of a fuel with the help of an oxidiser (usually the oxygen in the air). In premixed combustion, the fuel and the oxidiser are first mixed together in a combustible mixture and then burnt. The ratio of the fuel to the oxidiser (Fuel-Air Ratio or FAR) can be easily controlled beforehand. Lean premixing (when the value of the FAR < 1) ensures that the flame temperatures are lower. Since the probability of formation of NO<sub>x</sub> increases with increasing temperatures, lean premixing ensures that the

formation of  $\text{NO}_x$  is reduced, by closing controlling the FAR. Further the formation of soot and CO can be avoided. Stability of pre-mixed combustion is characterised by the flow velocity of the fuel-oxidiser mixture ( $u$ ) and the velocity of the flame ( $s_f$ ). This is shown in Figure 2.8. However, the disadvantages include the possibility of flame flashback and blow-off. Flame Flashback occurs when the flow velocity ( $u$ ) is lower than the flame velocity ( $s_f$ ), causing the flame to travel upstream till it reaches the point of injection. This causes damage to the combustor.

Blow-off occurs when the flow velocity ( $u$ ) is greater than the flame velocity ( $s_f$ ) causing the flame to get advected downstream and possibly extinguished. These phenomena lead to a set of strict upper and lower stability limits.

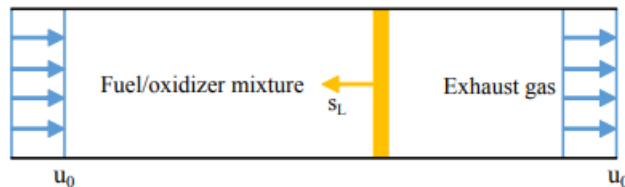


Figure 2.8: Flame Propagation in premixed combustion flame[54]

In non-premixed combustion, the fuel and the oxidiser are separate entities, which are brought into the combustion chamber, where they react and burn as they mix through diffusion. The mixture of fuel and oxidiser formed has density variations, that is, some parts are more rich in fuel content whilst other parts are richer in oxidiser content as shown in Figure 2.9. In between, the range, lies the stoichiometric Fuel Oxidiser ratio. This is where the flame front is formed. Due to the exothermic nature of combustion, the heat released causes the products to expand. Due to this expansion, the products diffuse into the fresh fuel and oxidiser on either sides of the flame front. Simultaneously, fresh fuel and oxidiser diffuse towards the flame front to compensate for the loss in the concentration of the reactants. This is how the flame is sustained. Thus, the rate at which the reactants mix and the rate at which they react are the 2 factors that characterise the stability of Non-Premixed combustion. Since the reaction rate is the highest at stoichiometric conditions, the flame front is usually formed there and the flame is anchored unlike pre-mixed combustion. Therefore, the possibility of flashback is very low leading to a wider set of stability limits [21].

The disadvantage of non-premixed Combustion is the generation of high concentrations of soot due to the presence of non-stoichiometric conditions in the the fuel rich section. Additionally, the formation of the flame front at the stoichiometric conditions gives rise to a high flame temperature, which leads to high  $\text{NO}_x$  emissions. Two well known configurations of non-premixed combustion can be seen in Figure 2.10.

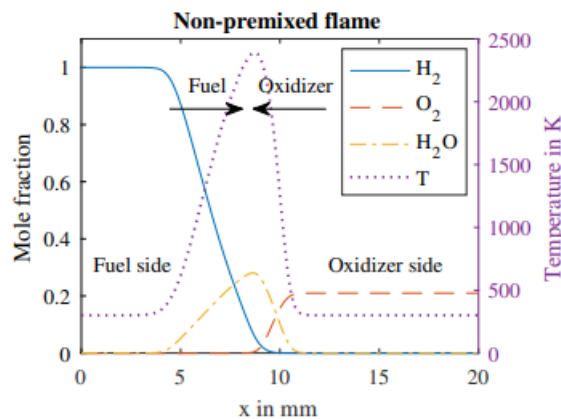


Figure 2.9: Species Distribution of Non-Premixed Combustion [54]

Both the types of combustion can be further classified into laminar and turbulent types based on the flow



conditions.

In the context of this project, where hydrogen and pure oxygen are to be used, it is a valid question to ask which combustion method will be most suitable. Though the gas turbine manufacturers have mostly shifted to lean premixed combustion on account of lower emissions and better ability to control FAR and lower temperatures[21], in the current context of hydrogen, non-premixed combustion has the following advantages:

- The danger of combustion outside the combustion chamber due to premixing of high temperature oxygen and hydrogen is avoided.
- There is a higher chance of flashback in premixed combustion. Due to the flame anchoring in Non-Premixed Combustion, the chances of this phenomena taking place are very low.
- The combustion is controlled by the rate of mixing and the rate of reaction. Therefore it becomes easier to control the mixing, since they come in 2 separate streams from the SOFC.
- The concern of emissions associated with non-premixed combustion in general, can be ignored in this case since the fuel is carbon neutral and the oxidiser is  $N_2$  free. Thus there will be no carbon and  $NO_x$  emissions.

Thus, in the subsequent section non-premixed combustion has been explored more in depth.

### 2.3.2 Laminar Non-Premixed Combustion

As stated earlier, the flow velocity of the flame formed is laminar in nature. There are mainly 2 types of Gaseous laminar Diffusion flows:

- Co-flow : Here both the fuel and the oxidiser flow in the same direction through an annular tube, where they diffuse downstream and react. Due to the parallel flow of the reactants, a thin flame front is formed which contains rapid and sharp changes in the concentration and temperature of the species, setting up large gradients as the mixing takes place. This forms the flame which is identified by its luminescence. This co-flow arrangement can be seen in Figure 2.9.
- Counter flow: In this type, the fuel and oxidiser are on opposite sides. They diffuse into each other through molecular diffusion. Upon mixing, a stagnant flame front is formed. The release of heat energy and the formation of the products is followed by their diffusion into the oxidiser and fuel in both directions of the flame front. A simplified schematic is shown in Figure 2.10;

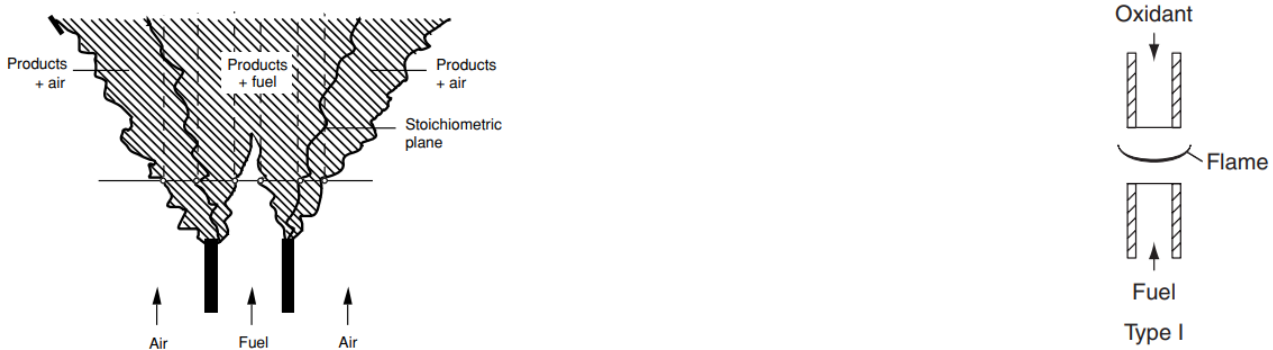


Figure 2.10: A schematic of Co-flow [60] and Counter flow [20] Non-Premixed Flames

In order to study Non-Premixed Combustion it is imperative to quantify the mixing of the fuel and oxidiser. This is because whether the mixture formed will be stoichiometric or not will depend upon the rate and amount of mixing. Hence, a quantity known as the mixture fraction has been defined. The mixture fraction is a useful

quantity which helps to determine the amount of mixing at different points in a Non-Premixed flame. First a quantity known as the Elemental fraction is defined as follows:

$$Z = \sum_{i=1}^S \mu_{ij} w_j \quad (2.7)$$

where S is number of elements,  $\mu_{ij}$  is mass fraction of reactants or species and  $w_j$  is mass proportion of the element in the species

This elemental mass fraction, indicates the contribution of each element to the species multiplied by the fraction of species in each stream, the streams being either fuel(1) or oxidiser (2).

The normalised elemental fraction gives the mixture fraction:

$$\xi = \frac{Z_i - Z_{i2}}{Z_{i1} - Z_{i2}} \quad (2.8)$$

where 1 is in reference to stream 1 (fuel) and 2 is in reference to stream 2 (oxidiser)

$\xi$  varies from 0 to 1 as:

- for the pure fuel = 1
- for the pure oxidiser = 0.

This effectively tells the composition of the mixtures at each point in the mixed stream, as this coordinate can only vary between 0 and 1. If it is assumed that the diffusivities of all reacting species are equal, then the mixture fraction of all elements would be equal to each other. Thus the mixture fraction would only vary from location to location and not between different elements. This essentially highlights the successful quantification of the combustion only in terms of a mixing variable.

Therefore, a stoichiometric mixture fraction can be defined  $\xi_{stoic}$  for Non-Premixed combustion. Parallel to premix combustion, lean and rich fuel mixtures can be defined as: if  $\xi_{stoic} < \xi < 1$  then the mixture is fuel rich, else if  $1 > \xi_{stoic} > \xi$ , then the mixture is lean.

Since in a chemical reaction, elements are neither created nor destroyed, the mixture fraction is always conserved and hence there is no source term in its transport equation, which is given as follows [60], does not have a source term.

$$\frac{\partial \rho \xi}{\partial t} + \nabla \cdot (\rho \xi u) - \nabla \cdot (\rho D \nabla (\xi)) = 0 \quad (2.9)$$

The first term indicates the change in the mixture fraction and density with time. The second term indicates the advection and the third term indicates the diffusion.

### 2.3.3 Turbulent Non-Premixed Combustion

From the theory of Non-Premixed Laminar Combustion developed in the previous section, the turbulent counterpart can now be explored. Before that, some basic concepts of turbulence have been presented.

#### Turbulence and its Statistical Treatment

Turbulence can be described as the transition of a flow from ordered, regular motion to a random chaotic motion. This transition is quantified by the Reynolds number, which is defined as:

$$Re = \frac{\rho u L_{char}}{\mu} \quad (2.10)$$

where  $\rho$  is density of the fluid,  $u$  is velocity of flow,  $L_{char}$  is characteristic length scale flow the flow geometry and  $\mu$  is dynamic viscosity of the flow. Common characteristics of Turbulent Flow include:

- Random or chaotic motion with extreme sensitivity to initial conditions.
- A wide range of length scales (smallest to largest eddies)
- Enhanced mixing.

The third characteristic is of special importance for engineering applications such as diesel engines, combustors, furnaces etc.[60]

The basic working behind turbulent flow can be explained by the phenomena termed as Energy Cascading. The large eddies formed extract energy from the mean flow and transfer their energy to the smaller eddies which in turn transfer theirs to even smaller eddies. The smallest eddy then dissipates this energy to the mean flow via viscous dissipation. This is shown below in Figure 2.11

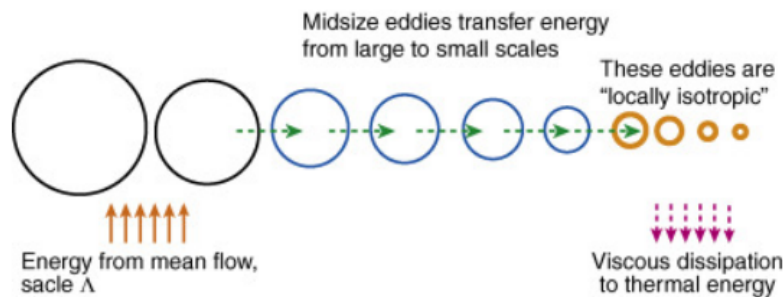


Figure 2.11: Energy Cascade in Turbulent Flows [57]

## Turbulence Modelling

It is fair to say that the exact solution has not been developed for turbulence, however a number of numerical solutions do exist, and the most well known ones can be characterised from [9] as follows:

- Direct Numerical Simulation (DNS)
- Large Eddy Simulation (LES)
- Reynolds Averaged Navier-Stokes Equations (RANS)
  - Differential Reynolds Stress Models (DRSM) : Use 1 Differential Equation to model the Reynolds Stresses e.g. Turbulent KE Model
  - Algebraic Reynolds Stress Models (ARSM): Use 1 Algebraic Equation to model the Reynolds Stresses. e.g. Prandtl's mixing length model.
  - Eddy Viscosity Models ( $k - \omega, k - \epsilon, k - \tau$ ): Use 2 coupled partial differential equations to model the Reynolds stresses. e.g. Turbulent KE and Dissipation rate Model ( $k - \epsilon$ )

Of these, DNS provides the best possible picture of turbulence, since it resolves all the different length and time scales for all the eddies formed, without the use of empirical formulation. However the computational power required is very high and therefore it can only be used for simpler flows with low Reynolds numbers [9]. LES is the next best method in terms of accuracy and resolution. The difference between DNS and LES lies in the fact that LES only considers the length scales of the larger eddies in detail whereas the time and length scales for the smaller eddies are averaged.

However a lot of the solvers of commercial packages are based on the Reynolds Average Navier-Stokes equations [60], which come by due to the statistical treatment of the Navier-Stokes equations. To reduce the computational cost even further, both the time and length scales for all eddies are averaged. In the context of this thesis, the overall design of the combustor is of much more importance than the microscopic study of the turbulent combustion process. Therefore, the statistical averaging of the RANS equations offers a good balance of precision and computational cost. Hence, the RANS equations have been considered in further sections.

## RANS Equations

Reynolds Decomposition is the basis of the statistical treatment of the NS equations. It basically represents a quantity in terms of its average and fluctuation as follows:

$$q = \bar{q} + q' \quad (2.11)$$

where  $\bar{q}$  is average of the quantity and  $q'$  is the fluctuation of  $q$

The average of the quantity can be stationary or vary with time. This can be seen from the following graphs and formulae:

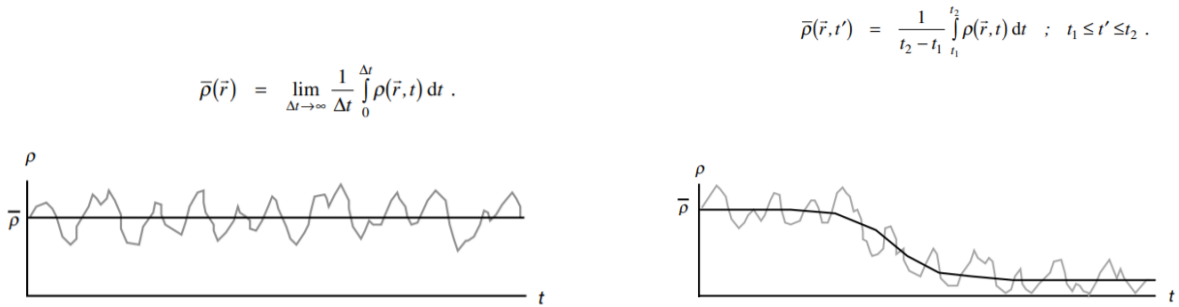


Figure 2.12: Stationary Turbulence and transient turbulence [60]

In the case of transient turbulence, in order to capture all the instantaneous fluctuations, the time period  $t'$  must be selected such that it is larger than the fluctuation time  $t_1$  but smaller than the overall time period of observation  $t_2$ .

Another important concept is the Favre Average. This is a density weighted average of any quantity, given as:

$$\tilde{q} = \frac{\overline{\rho q}}{\bar{\rho}} \quad (2.12)$$

Any parameter can be written as a sum of its Favre average ( $\tilde{q}$ ) and the fluctuation ( $q''$ ) using Reynolds decomposition.

$$q = \tilde{q} + q'' \quad (2.13)$$

Now, it can be illustrated how this statistical treatment is helpful for solving turbulence.

The RANS equations are obtained by substituting the flow parameters in the form of their mean and their fluctuating components in the Navier-Stokes Equations. This leads to a set of equations with mean parameters accompanied by a set of fluctuating parameters. These parameters are unknown and are in the form of the dependant variables and are termed as Apparent or Reynolds stresses. Consider the RANS Momentum equation formed by decomposing the velocity using Equation 2.13:

$$\frac{\partial \bar{\rho} \tilde{v}}{\partial t} + \nabla(\bar{\rho} \tilde{v} \times \tilde{v}) + \nabla(\bar{\rho} + \overline{\rho v'' \times v''}) = \bar{\rho} g \quad (2.14)$$

The  $\overline{\rho v'' \times v''}$  term is the Reynolds Stress also known as the Apparent Stress or Turbulent transport.

## Eddy Viscosity Models

Now in order to model the turbulent flow, the apparent stresses should be known. Since they are unknown, they are approximated by using the gradient transport assumption which states that mean of the turbulent fluctuations of a variable ( $\overline{v'' \times v''}$ ), flows down the gradient of the mean of that variable ( $\nabla \tilde{v}$ ). This can be seen as:

$$\overline{\rho v'' \times v''} = \bar{\rho} \mu_t \nabla \tilde{v} \quad (2.15)$$

Here a new term known as the turbulent viscosity ( $\nu_t$ ) is introduced. The issue is that until the value of  $\mu_t$  is calculated, the RANS equations cannot be closed. Therefore, to do that, The RANS models are used. Out of the RANS models, these days Eddy Viscosity Models (EVMs) are mostly preferred over DRSM and ARSM as they are considered obsolete [60].

The main RANS Equations as given in [60] with the gradient transport assumption are: Mass Conservation, Species(Concentration) Conservation, Momentum Conservation, Energy (Enthalpy) Conservation and Element (mixture fraction) Conservation respectively.

$$\frac{\partial \bar{\rho}}{\partial t} + \nabla \cdot (\bar{\rho} \bar{v}) = 0 \quad (2.16)$$

$$\frac{\partial \bar{\rho} \bar{w}_i}{\partial t} + \nabla \cdot (\bar{\rho} \bar{w}_i \times \bar{v}) - \nabla \cdot (\bar{\rho} \mu_T \nabla \bar{w}_i) = \bar{M}_i \bar{\omega}_i \quad (2.17)$$

$$\frac{\partial \bar{\rho} \bar{v}}{\partial t} + \nabla (\bar{\rho} \bar{v} \times \bar{v}) - \nabla \cdot (\bar{\rho} \mu_T \nabla \bar{v}) = \bar{\rho} \bar{g} \quad (2.18)$$

$$\frac{\partial \bar{\rho} \bar{h}}{\partial t} - \frac{\partial \bar{\rho}}{\partial t} - \nabla \cdot (\bar{\rho} \bar{v} \bar{h}) + \nabla \cdot (\rho \mu_T \nabla \bar{h}) = \bar{q}_r \quad (2.19)$$

$$\frac{\delta \bar{\rho} \bar{\xi}}{\delta t} - \nabla \cdot (\bar{\rho} \bar{\xi} \bar{u}) - \nabla \cdot (\bar{\rho} \mu_t \nabla (\bar{\xi})) = 0 \quad (2.20)$$

Out of the EVMs given in Section 2.3.3, for modelling the non-premixed turbulent combustion, the Realizable  $k - \varepsilon$  model by Shih et al. [48] has been selected. This selection is based on good agreements of the modelling results with experimental data as seen in literature [34],[54],[16]. The Realizable  $k - \varepsilon$  model has been explained in detail in Section 2.3.4.

Since the theoretical foundation for turbulence has been set, the subsequent sections deal with the models regarding the mixing and chemistry in Non-Premixed Turbulent Combustion.

### 2.3.4 Realizable $k - \varepsilon$ Turbulence Model

The Realizable  $k - \varepsilon$  model given by Shih et al. [48] solves the equations for the turbulent kinetic energy  $k$  and the turbulent dissipation rate  $\varepsilon$  to calculate the turbulent viscosity through a modified equation. This value of turbulent viscosity can then be used to close the RANS equations as shown in Equation 2.15 in Section 2.15.

The turbulent viscosity is calculated by the following formula:

$$\mu_t = \rho C_\mu \frac{k^2}{\varepsilon} \quad (2.21)$$

Here, the value of  $C_\mu$  is not a constant and is a function of the strain and vorticity tensors. The full treatment of  $C_\mu$  can be found here [48]. To calculate the turbulent viscosity, the value of  $k$  and  $\varepsilon$  must be calculated via the transport equations for turbulent Kinetic energy and the turbulent dissipation rate, which are given as follows:

$$\frac{\partial (\rho k)}{\partial t} + \tilde{\nabla} \cdot (\rho k \tilde{u}) = \tilde{\nabla} \cdot (\mu + \frac{\mu_t}{\sigma_k}) \tilde{\nabla} k + G_k + G_b - \rho \varepsilon \quad (2.22)$$

$$\frac{\partial \rho \varepsilon}{\partial t} + \tilde{\nabla} \cdot (\rho \varepsilon \tilde{u}) = \tilde{\nabla} \cdot (\mu + \frac{\mu_t}{\sigma_k}) \tilde{\nabla} \varepsilon + \rho C_{1\varepsilon} S \varepsilon - \rho C_{2\varepsilon} \frac{\varepsilon^2}{k + \nu \varepsilon^2} + C_{1\varepsilon} \frac{\varepsilon}{k} C_{3\varepsilon} G_b \quad (2.23)$$

where  $G_k$  = production of turbulent KE via velocity gradients,  $G_b$  = production of KE via bouyancy,  $\rho \varepsilon$  = dissipation of turbulent KE due to  $\varepsilon$ ,  $\sigma_k$  = turbulent prandtl number for Turbulent KE  $\sigma_\varepsilon$  = turbulent prandtl number for Turbulent dissipation rate

The constants  $C_{1\varepsilon} = 1.44$ ,  $C_{2\varepsilon} = 1.92$ ,  $\sigma_k = 1$ ,  $\sigma_\varepsilon = 1.3$  have been experimentally determined and validated [48]. These values are used as default values in ANSYS Fluent.

## 2.4 Turbulence-Chemistry interaction

### 2.4.1 Infinite Chemistry Model

The interaction between turbulence and chemistry is complex. To capture this interaction accurately in a combustion reaction, it is essential to pick the right chemistry model. In the context of this research, the infinite chemistry model also known as the chemical equilibrium model has been chosen. The reasons for doing so are:

- The combustion of hydrogen and pure oxygen at high temperatures is very reactive, especially given that the typical SOFC outlet stream will be above the autoignition temperature of hydrogen (> 585 °C). Therefore, the reaction rate will be much faster than the mixing.
- The major advantage of a finite chemistry model is the accurate prediction of formation of soot and NO<sub>x</sub>. However in this case it is not applicable, as the only product formed will be steam in all cases. Therefore, the finite chemistry model is not needed.

The Infinite Chemistry model takes the following assumptions to simplify the physics behind the combustion reaction:

- Diffusivities of all scalars are equal, thus all species mix the same and hence their mixture fractions are the same. (Section 2.3.2)
- The species react instantly to equilibrium upon mixing.
- Lewis number = 1, thus the heat diffuses at the same rate as the concentration for all species.
- There is no heat loss i.e. the combustion is adiabatic.

By taking these assumptions, it is simply implied that the combustion is characterised by the amount of mixing since the reaction rate is much higher than the mixing rate and hence the mixing amount is the limiting factor. Or the Damkohler number  $\gg 1$  (reaction time scale/diffusion time scale). Additionally it is assumed that the moment the mixing takes place, combustion takes place and the products are formed. Hence, predicting the mixing of turbulent flows with variable densities is simplified to keeping track of the mixture fraction  $\xi$ . This can be done by solving the mixture fraction transport equation given by Equation 2.9. There is no source term in the mixture fraction transport equation, as it is a conserved scalar.

Since the combustion is assumed to be adiabatic and at a constant pressure, the total enthalpy change of the system is zero for a steady state process. Therefore, the total enthalpy can be expressed in terms of the mixture fraction by using a total enthalpy balance as follows:

$$h_1(\xi) + h_2(1 - \xi) = h \rightarrow \xi = \frac{h - h_2}{h_1 - h_2} \quad (2.24)$$

where  $\xi$  now denotes the ratio in which the fuel(1) and oxidiser(2) are mixing at a particular location and instant in time to give the total enthalpy of the mixture( $h$ )

Once the enthalpy is calculated, the temperature can be calculated. This temperature is the Adiabatic Flame Temperature ( $T_{ad}$ ). Using this temperature, the density of the mixture can be calculated by using the ideal gas, since at high temperatures, the gasses can be assumed to be ideal.

$$pV = nRT_{ad} \rightarrow \rho = \frac{\mu p}{RT} \quad (2.25)$$

where  $p$  = pressure of the gas,  $V$  = volume occupied by the gas,  $n$  = number of moles of the gas mixture,  $R$  = Universal gas constant,  $T_{ad}$  = adiabatic flame temperature,  $\mu$  = molar mass of the gas mixture  
Thus in this way, the mixture fraction can be used to calculate all scalar variables of the mixture.

## 2.4.2 The Probability Density Function Modelling Approach

The mixture fraction transport equation only models the mixing of the flow and not the turbulent momentum. Therefore, the momentum equation also needs to be solved. Thus, this is a system of coupled differential equations. Since turbulence is involved, RANS equations are to be considered. The RANS Momentum Equation has already been given in Equation 2.14. Similarly, the RANS Mixture Fraction equation also needs to be considered as follows[60]:

$$\frac{\delta \bar{\rho} \tilde{\xi}}{\delta t} + \nabla \cdot (\bar{\rho} \tilde{\xi} \tilde{u}) - \nabla \cdot (\bar{\rho} \mu_t \nabla (\tilde{\xi})) = 0 \quad (2.26)$$

From this equation, it can be seen that the advection ( $\bar{\rho} \tilde{\xi} \tilde{u}$ ) and Turbulent Diffusion ( $\nabla \cdot (\bar{\rho} \mu_t \nabla (\tilde{\xi}))$ ) terms affect the overall change in the density and mixture fraction ( $\frac{\delta \bar{\rho} \tilde{\xi}}{\delta t}$ ). This qualitatively means that the fuel and oxidiser streams diffuse into each other while advecting forward. This gives rise to mixing and an overall change in the mean mixture fraction and the mean density.

This change in mean density is reflected in the momentum equation since both the equations are coupled. This can be seen in Figure 2.13, which depicts the overall track of the turbulent modelling process.

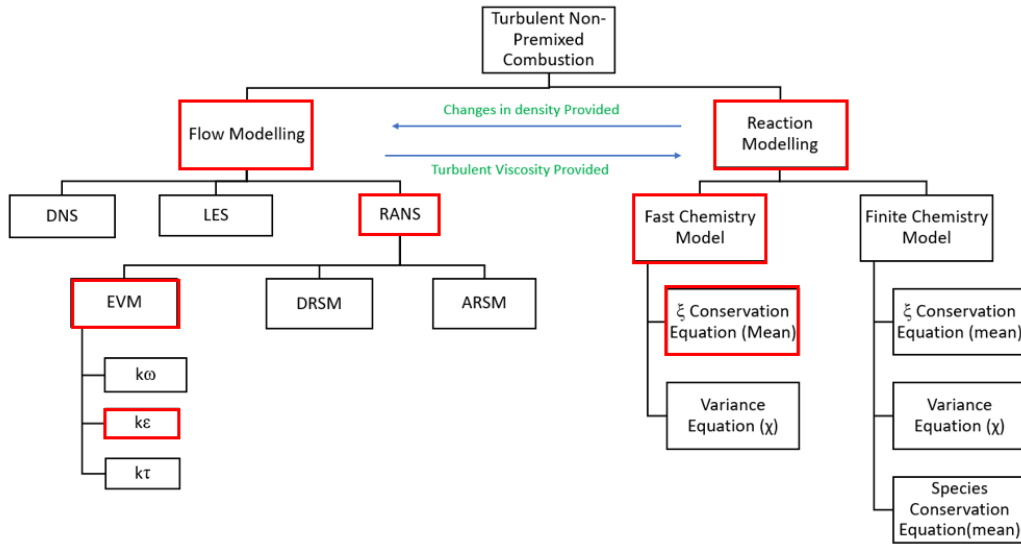


Figure 2.13: Overview of the Modelling Process. The flow is modelled using the RANS equations. The RANS equations are closed using the closure models, in this case the  $k - \epsilon$  model. The density for the RANS equations are obtained from the reaction modelling using the infinite (fast) chemistry model. The turbulent viscosity  $\mu_t$  is obtained by solving the RANS equations. This  $\mu_t$  is used to solve the mixture fraction equation and complete the reaction modelling.

Further the turbulent viscosity term ( $\mu_t$ ) in this equation, needs to be calculated by the Realizable  $k - \epsilon$  model (Section 2.3.4) for the momentum equation. To solve these coupled equations, and get the mean values of the scalars, a probability density function can be used. A probability density function of a variable  $x \in [a, b]$  is defined as the probability of finding that variable between  $a$  and  $b$ . Since it denotes probability, the PDF can only have values between 0 and 1. By multiplying the variable with the probability of its location and integrating over the whole range, the mean of the variable can be very easily found as:

$$1 = \int_a^b P(x) dx \quad (2.27)$$

$$\bar{x} = \int_a^b x P(x) dx \quad (2.28)$$

The PDF also takes into account the fluctuation of the properties in terms of their deviation from the mean value. Thus, if the shape of the PDF is known (or assumed) and constrained to 2 variables, the mean and the

variance ( for a  $\beta$  distribution or a Normal Distribution) can be used to calculate the mean of the parameters and their variation from these mean values. The variance equation for the mixture fraction is given as follows:

$$\nabla \cdot (\bar{\rho} \tilde{\xi}''^2) - \nabla \cdot (\bar{\rho} \mu_t) = 2\bar{\rho} \mu_t \nabla^2 \bar{\xi} - \overline{2\rho D \nabla^2 \xi''} \quad (2.29)$$

Using the gradient transport assumption,  $\overline{2\rho D \nabla^2 \xi''} = 2D \nabla^2 \bar{\xi} = \chi$

The scalar dissipation rate ( $\chi$ ) gives a measure of the mixing rate at the molecular level. This mixing gives rise to the fluctuations. These fluctuations are expressed as deviations from the mean values by the variance.

Once the mean ( $\bar{\xi}$ ) and variance ( $\xi''^2$ ) of  $\xi$  have been calculated by solving Equations 2.26 and 2.29 a PDF can be generated ( $\tilde{P}(\xi)$ ). Then all scalars can be calculated in terms of there mean and variance since they are all functions of the mixture fractions.

$$\tilde{T} = \int_0^1 (T(\xi)) \tilde{P}(\xi) d\xi \quad (2.30)$$

$$\tilde{\rho} = \int_0^1 (\rho(\xi)) \tilde{P}(\xi) d\xi \quad (2.31)$$

$$\tilde{T}''^2 = \int_0^1 (T(\xi) - \tilde{T})^2 \tilde{P}(\xi) d\xi \quad (2.32)$$

$$\tilde{\rho}''^2 = \int_0^1 (\rho(\xi) - \tilde{\rho})^2 \tilde{P}(\xi) d\xi \quad (2.33)$$

$$P(\tilde{\xi}) = \frac{1}{\rho} \int_0^\infty \rho P(\rho, \xi) d\xi \quad (2.34)$$

The following schematic represents the PDF of an air-fuel mixture at different locations.  $w$  represents the scalar being observed.

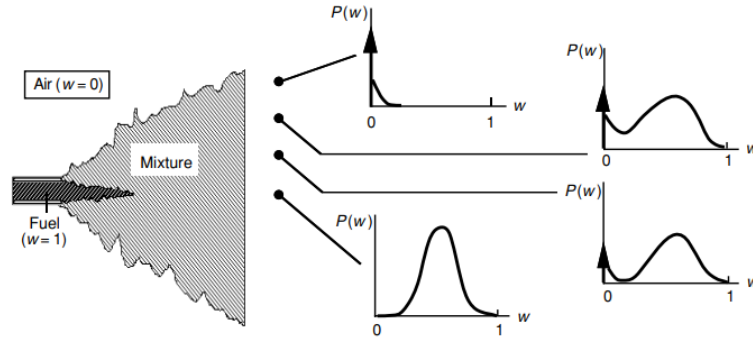


Figure 2.14: The schematic represents the probability of finding the scalar  $w$  in a particular range at various locations of an fuel-oxidiser mixture [60]

The following flowchart is a representation of the relations between the various equations being used to model the Non-Premixed Turbulent Combustion.

Due to the assumptions taken, the model has the following shortcomings as stated in [60].

- Flame extinction is not taken into consideration since the reaction kinetics are assumed as infinitely fast.
- $\text{NO}_x$  amounts are erroneously predicted and soot is not predicted at all due to the infinite chemistry assumption.

These are solved by the Finite Chemistry Model, which has been explained in more detail in Appendix A.1.

## 2.5 Combustor Type for $\text{H}_2\text{-O}_2$ combustion

In the context of Non-Premixed pure hydrogen-oxygen combustion, the amount of literature is sparse. Since the choice of the type of combustor is an important one. To facilitate maximum mixing, two major choices become apparent:



- A swirl Stabilised burner: The swirl stabilised burner uses the concept of swirling the fuel and oxidiser streams to cause mixing on a macro scale. Tanneberger et al. [54] from TU Berlin did an extensive PhD thesis for the testing of a Non-Premixed H<sub>2</sub>-O<sub>2</sub> burner. They developed a non-premixed swirl stabilised burner. For cooling and dilution steam was chosen. This burner is shown in Figure 2.15.

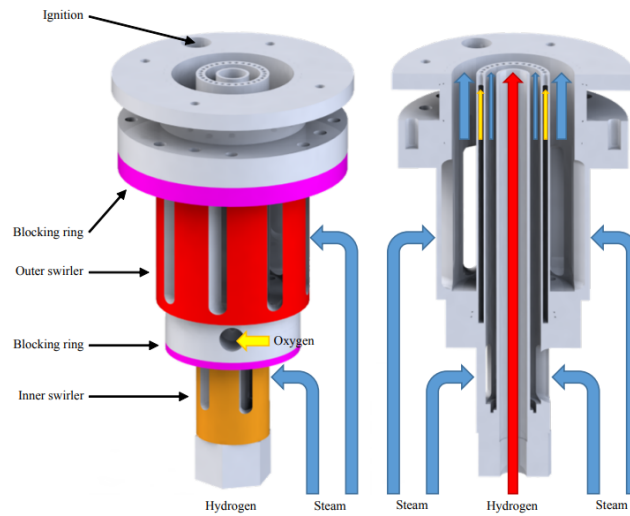


Figure 2.15: A swirl stabilised H<sub>2</sub>-O<sub>2</sub> Burner developed by Tanneberger et al. at TU Berlin [54]

The steam was given a degree of swirl however the hydrogen and oxygen streams entered axially without any swirl. Flame stability was observed by varying the amount of steam and the swirl intensity of steam. It was observed that 2 separate flame shapes were being formed, a jet flame at low steam dilution and a swirl stabilised one at high steam dilution as shown in Figure 2.16. (Steam Dilution ratio  $\Omega$  = Amount of steam/ amount of hydrogen and oxygen)

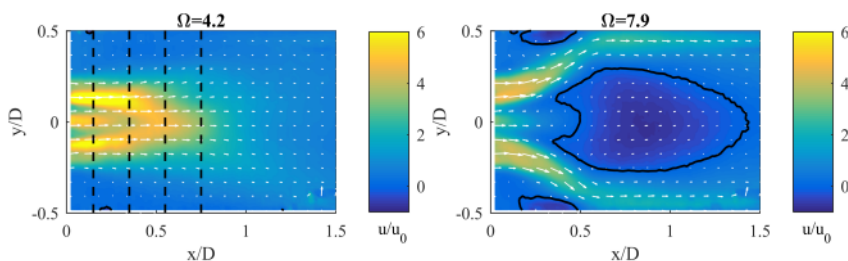


Figure 2.16: 2 Distinct flame shapes being formed at various values of steam dilution- Jet flame ( $\Omega = 4.2$ ) and Swirl Stabilised flame ( $\Omega = 7.9$ ). The contour lines on the right are lines of zero-axial velocity due to the flame swirling around the contour.  $y/D$  is the normalised diameter of the flame and  $x/D$  is the normalised length, where  $D$  is the diameter of the combustion chamber.[54]

This behaviour can be explained by the fact that at high steam dilution, the vortex formed by the steam was strong enough to make a swirl stabilised flame whereas for low steam dilution the swirl given to the oxygen stream was not strong enough to cause the swirl and hence a basic jet flame was formed. The author concluded that a change in burner geometry would be required to ensure a constant flame shape throughout the entire range. The changes suggested were either to add swirl to all 3 streams or to remove the swirl completely and inject the streams axially. This conclusion implies that the flame shape remaining constant over the entire range of the stability limits is crucial to the operation of the combustor as a slight drop in efficiency was noted during the transition from jet to the swirl stabilised flame. A possible explanation for this could be the instability of the flame during the transition from Jet flame to Swirl Stabilised Flame. Further, low dilution ratios showed the best combustion efficiency and high swirl intensity showed the best stability, albeit at the expense of pressure loss. At very high dilution ratios, combustion efficiency dropped and un-burnt residuals of H<sub>2</sub> and O<sub>2</sub> were observed in the exhaust.

- A micromix burner: Developed by FHA Aachen University [10], a micromix burner uses the concept of small jets in cross flow to mix the fuel and the oxidiser on a micro scale, hence the name micromix. Rapid mixing on such a small scale leads to a higher mixing intensity[11].

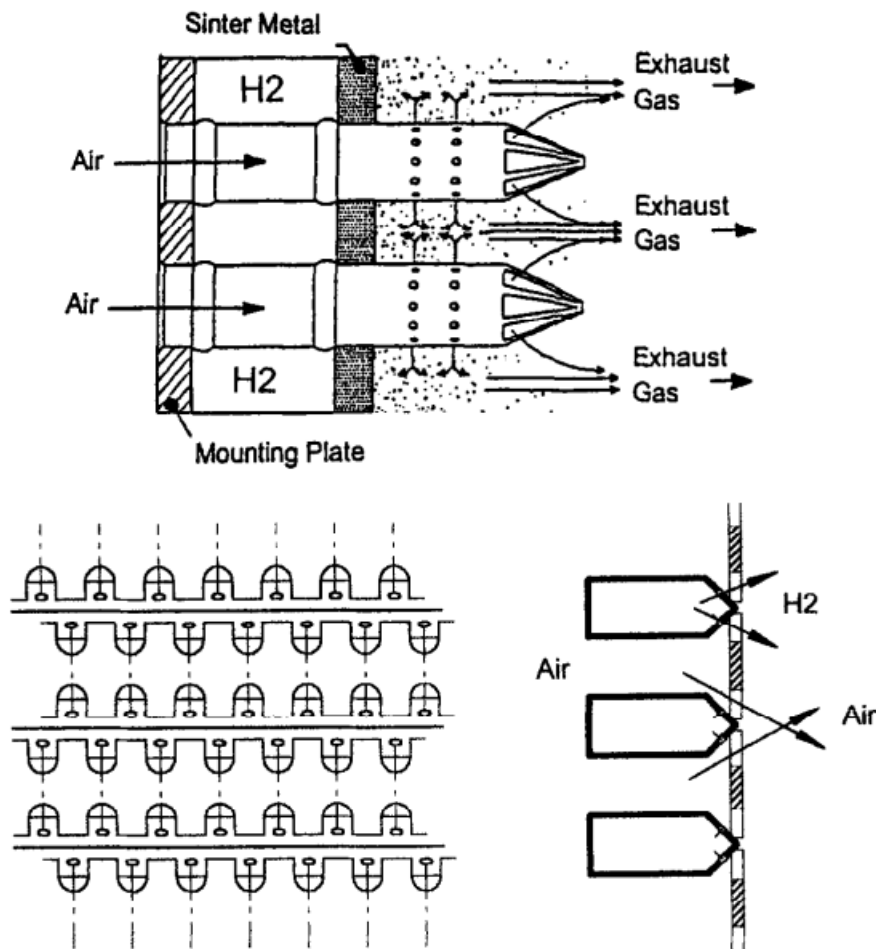


Figure 2.17: Two micromix concepts for H<sub>2</sub> combustion developed by Dahl et al.[10]- Matrix type and two-dimensional type

The micromix burner uses the concept of Jets in crossflow. Jets in cross flow are used in many industrial applications such as boilers, burners, furnaces and especially in gas turbines due to their superior mixing ability as compared to parallel mixing of jets.

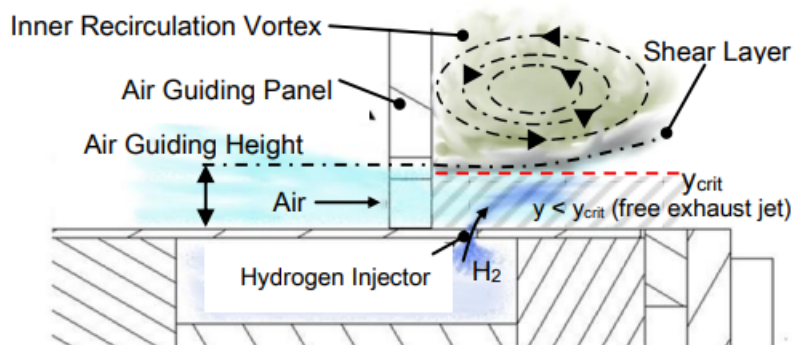


Figure 2.18: A schematic of micromix combustion of hydrogen in air. the air guiding height controls the amount of air into the combustor. [16]

Funke et al.[16] developed a non-premixed type combustor for hydrogen-air combustion. The burner showed extremely low  $\text{NO}_x$  emissions and a short stable flame [16]. Micromix combustors have been used to combust hydrogen in air since with their superior mixing capabilities at high temperatures, the amount of non-stoichiometrically burnt fuel is less, and therefore the amount of  $\text{NO}_x$  is less.

In the context of this research,  $\text{NO}_x$  emissions are not of prime concern since pure oxygen is being used instead of air. Therefore the strong the mixing capabilities of the micromix burner are advantageous to achieve perfect stoichiometric combustion.

## 2.6 Ejector

### 2.6.1 Basic Working

The ejector, also known as a "Jet Pump" [28], is a device that has long been used for the recirculation of fluids in refrigeration systems and HVAC systems [56] it has also found applications in electrode gas re-circulation for SOFCs such as in the research by Chen et al.[8], Maclay et al. [35], Genc et al.[19] to name a few. As stated in Section 2.2.5, the ejector works by creating a suction. The primary gas is accelerated through the primary nozzle, and at the exit, it creates a large pressure drop. This pressure drop causes the secondary fluid to be sucked into the mixing chamber. This can be seen in Figure 2.19, where two types of ejectors are shown. The ratio between the mass flow of the secondary and the primary fluids is known as the entrainment ratio. This is given by:

$$\omega = \frac{m_{secondary}}{m_{primary}} \quad (2.35)$$

The ejector can be of constant area type or constant pressure type. These are shown in the figure below.

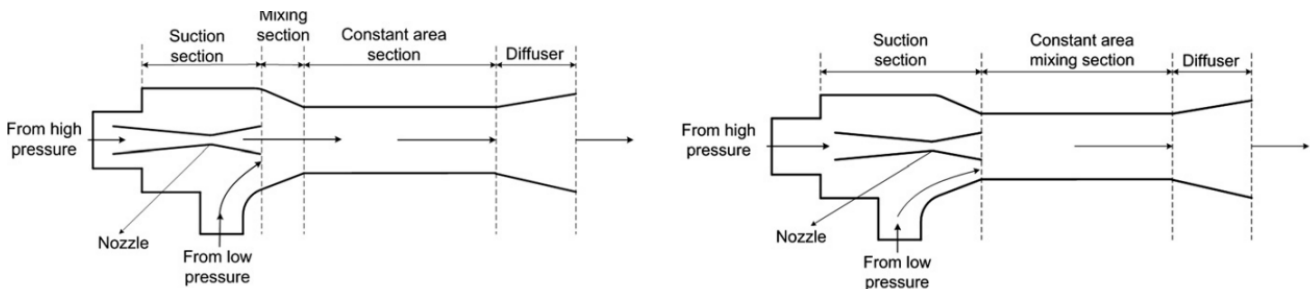


Figure 2.19: A constant pressure type ejector (left) and a constant area type ejector(right) [25]

In a constant pressure type ejector, the mixing section is converging and the secondary and primary streams mix at a constant pressure. This can be seen in Figure 2.19 on the left side. In the constant area type ejector, the mixing section has a constant area of cross section and the mixing of the two streams does not occur at a constant pressure. This is evident from the constant area section marke in Figure 2.19 on the right. Keenan et al.[28] showed that constant pressure type ejectors perform better than constant area types ejectors due to their ability to sustain higher backpressure, where the back pressure is the pressure at the outlet of the diffuser. Therefore, here only constant pressure type ejectors have been described.

In order to entrain a large amount of fluid through the secondary inlet a larger pressure drop needs to be created. Therefore, super sonic ejectors are employed wherein both the fluids at the entrance of the constant pressure mixing region attain sonic (or supersonic) velocity. As the mixing occurs in this constant pressure mixing region, the mixed flow also exits at a sonic (or supersonic) velocity. Upon entering the constant area section, the mixed fluid is suddenly slowed to subsonic velocities leading to the formation of transverse shocks. These lead to a large pressure rise. The equation for mach number after the transverse shock ( $M_k$ ) and the

consequent pressure rise ( $P_k$ ) is given by:

$$M_k = \left[ \frac{\frac{2}{\gamma-1} + M_j^2}{\frac{2}{\gamma-1} \gamma M_j^2 - 1} \right]^{0.5} \quad (2.36)$$

$$P_k = P_j \frac{M_j}{M_k} \frac{1 + \frac{M_j(\gamma-1)}{2}}{1 + \frac{M_k(\gamma-1)}{2}} \quad (2.37)$$

where  $M_j$  and  $P_j$  are the mach number and pressure before the shock respectively.

This transverse shock does not occur in the case of a sub-sonic ejector, however the decrease in velocity due to mixing, does lead to a relatively smaller rise in static pressure, nonetheless. Further pressure is recovered in the diffuser section at the end of the ejector. Since super sonic ejectors have higher entrainment ratios as compared to the subsonic ejectors, only this type has been considered here.

## 2.6.2 Model type

Keenan et al. was the first to work on ejectors and give a comprehensive 1-D mathematical model. Since then, his model has been largely used as a basis for other more sophisticated and complex models [35],[52]. In this study, the objective is to model the ejector as a part of the SOFC-GT cycle. Therefore a simple 1-D mathematical model can be used to describe the operation as well as to configure the geometry of the ejector for the required entrainment ratio. The model used by Maclay et al.[35] and Sun et al. [52] based on the work of Keenan et al.[28] has been used in this study. The model has been explained in greater detail in Section 5.2. A comprehensive review of the various models present can be found here [56].

## 2.7 Heat exchangers

Heat exchangers are devices that are used to transfer heat from one fluid to another in a thermodynamic cycle. This section introduces the most common types of heat exchangers that are available. Each heat exchanger has limits to their applicability and hence it becomes imperative to compare those limits in order to select the most suitable heat exchanger.

### 2.7.1 Types

- Shell and Tube heat Exchanger (STHE): The Shell and Tube Heat Exchanger consists of an outer shell which houses a bundle of tubes. The tubes can be straight, running through the length of the shell or they can be in the form of a U bend. The heat transfer between the fluids occurs over the surface of the tubes, as one fluid flows through the shell and the other flows through the tubes.

The main advantages of this type of heat exchanger are that its excellent for high pressure operation, has well developed fabrication methods, can be manufactured from a variety of materials and is easy to maintain and clean[50]. The operational limits of the shell and tube heat exchangers are between -200 °C to 750 °C and upto a 200 bar pressure [13]

Some of the major disadvantages of these heat exchangers is the lower heat transfer area per volume available as compared to plate type heat exchangers and that the minimum temperature pinch temperature usually does not go lower than 5 K.

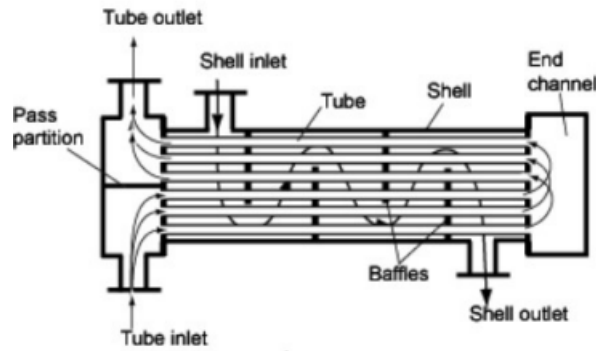


Figure 2.20: A basic schematic of a shell and tube heat exchanger [13]

- Gasket Plate Heat exchangers (GPHE): The plate heat exchangers consist of corrugated metal plates, which are rectangular in shape, pressed against each other, with gaskets at each end. Each pair of plates, has edge gaskets in between them, forming separate channels for the fluids entering at the top and bottom of each plate respectively. The edge gaskets also ensure that the fluids do not mix. Hence, the heat transfer takes place over the common plate in between the 2 fluids. Due to the presence of the corrugations, turbulence is induced into the fluids through vortices, swirling flows, and separation of boundary layers [59]. This induced turbulence leads to a higher heat transfer coefficients than in the shell and tube heat exchangers. This leads to Plate heat exchangers being about 30% the total area and 20 % the total volume of shell and tube heat exchangers and having a minimum approach temperature as low as 1 K[59]. The major disadvantage of plate heat exchangers is that they are not suitable for operating above 25 bar and 160 °C, due to the sealing limitations of the gaskets.

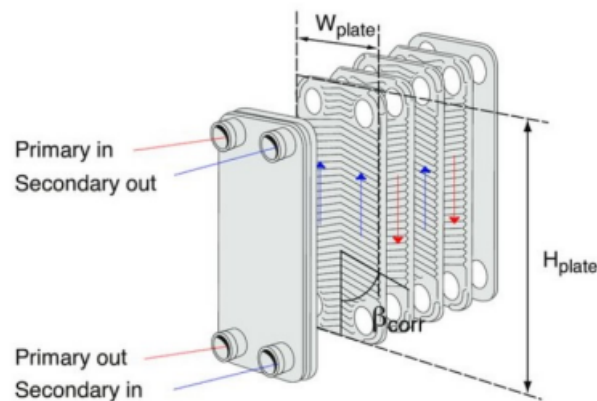


Figure 2.21: Basic schematic of a gasket plat heat exchnager [13]

- Welded Plate heat exchanger (WPHE): The welded plate heat exchanger eliminates the need for gaskets by sealing the plates at the edges using laser welds, with the plates being sandwiched between 2 end plates, fixed inside a frame [59]. This increases their structural integrity as well as the operational limits, which increase upto 40 bar and 350 C. The elimination of the gaskets, also allows the plates to expand and contract with temperature changes, thus increasing the overall high temperature fatigue strength. The disadvantages of this type of plate heat exchanger is the loss in flexibility to adjust the area of the plates, or changing the number of plates, since they are fixed. Additionally, this makes cleaning and maintenance difficult.

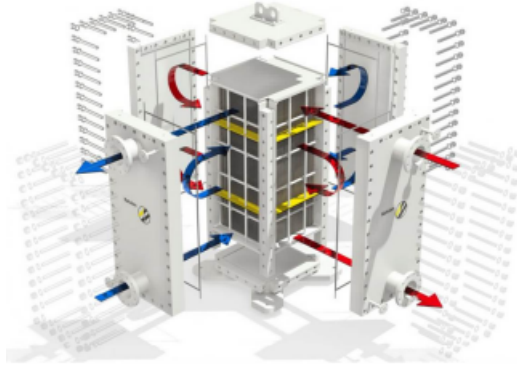


Figure 2.22: A welded plate heat exchanger [13]

- **Brazed Plate Heat Exchangers(BPHE):** Brazed Plate heat Exchangers are similar to WPHEs as they are also gasket free. The difference is that BPHEs are also frame free. They are usually compact (less than 1 m) and are used extensively in refrigeration systems and HVAC systems as evaporators and condensers[59].

A brief comparison of the various types of heat exchangers is given as follows:

Type	Pressure (bar)	Temperature (°C)	Min. Pinch Temperature (°C)
Shell and Tube HEX	200	-200 - 750	5
Gasket Plate HEX	25	30 - 160	1
Welded Plate HEX	40	-200 - 350	1
Brazed Plate HEX	30	-195 - 225	1

Table 2.1: Comparison between various types of Heat Exchangers

Higher temperatures can be sustained than given here, however the construction materials for the heat exchangers must be high temperature resistant materials such as titanium alloys or nickel-based super alloys.

### 2.7.2 Basic Design Procedure

The following is the basic design procedure that is common for all heat exchangers. This procedure is taken from Sinnot and Towler [50].

- **Specification of the duty/heat load ( $\Delta Q$ ):**The first step in designing a Heat exchanger is to find the area required for the specified duty and the rate of heat transfer. Therefore the basic heat transfer equation would be :

$$\Delta Q = U_0 A \Delta T_{lm} \quad (2.38)$$

where  $Q$  is the amount of heat to be added or removed (also known as the duty or the heat load), where  $U_0$  is the Overall heat transfer coefficient,  $A$  is the Area of heat transfer and  $\Delta T_{lm}$  is the Log mean temperature Difference (LMTD) which is defined as:

$$\frac{\Delta T_1 - \Delta T_2}{\ln\left(\frac{\Delta T_1}{\Delta T_2}\right)} \quad (2.39)$$

The LMTD signifies the driving force behind the heat exchanger. As the  $\Delta T_1$  and  $\Delta T_2$  values come closer, the heat transfer decreases and vice versa. The  $\Delta T_1$  and  $\Delta T_2$  values are defined for the co-current and counter-current pipe heat exchangers as shown in Figure 2.23.

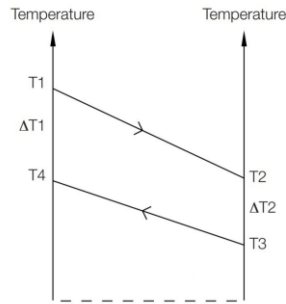


Figure 2.23: Standard Temperature Diagram of a Heat exchanger

- Collection of the physical properties of the fluids: All the physical properties of the fluids such as the density, viscosity, specific heat etc are to be collected at the relevant pressures and temperatures.
- Selection of the type of Heat exchanger: The type of heat exchanger is selected.
- Assumption of  $U_0$ : A value of the overall heat transfer coefficient is assumed.
- Calculation of LMTD: The LMTD is calculated as shown in equation 2.23.
- Calculation of the required Area  $A$ : After the calculation of the LMTD and the assumption of  $U_0$ , equation 2.38 can be solved for the area of the heat exchanger.
- Calculation of the actual  $U_0$ : The actual value of  $U_0$  can be calculated via the following equation for shell and tube Heat exchangers:

$$\frac{1}{U_0} = \frac{1}{h_o} + \frac{1}{h_{od}} + \frac{d_o \ln\left(\frac{d_o}{d_i}\right)}{2\lambda_w} + \frac{d_o}{d_i} \left( \frac{1}{h_{id}} + \frac{1}{h_i} \right) \quad (2.40)$$

And using the following equation for Plate heat exchangers:

$$\frac{1}{U_0} = \frac{1}{h_o} + \frac{1}{h_{od}} + \frac{W_t}{2\lambda_w} + \frac{1}{h_{id}} + \frac{1}{h_i} \quad (2.41)$$

where  $h_o$  is the Outer Film Coefficient ( $\frac{W}{m^2K}$ ),  $h_i$  is the Inner film Coefficient ( $\frac{W}{m^2K}$ ),  $h_{od}$  is the outer fouling factor ( $\frac{W}{m^2K}$ ),  $h_{id}$  is the inner fouling factor ( $\frac{W}{m^2K}$ ),  $d_o$  is the tube outer diameter ( $m$ ),  $d_i$  is the tube inner diameter ( $m$ ),  $\lambda_w$  is the thermal conductivity of the tube wall ( $\frac{W}{mK}$ ),  $W_t$  is the Wall thickness

- Comparison of the 2 values and iteration until convergence: Now the assumed value of  $U_0$  is compared with the calculated value of  $U_0$ . If they are different, then the calculated value of  $U_0$  is used in a second iteration and the area is recalculated. This iteration keeps going till the value of  $U_0$  converges and stops changing after each iteration.

## 2.8 Turbomachinery

A turbomachine is a device that transfers the energy of a moving fluid to or from a rotor. In case it transfers the energy to a rotor, it is known as a compressor. In case it extracts energy from a fluid flowing through it, it is known as a turbine. Here, the turbine will be explored in greater detail.

### 2.8.1 Types

There are a number of turbines such as an axial turbine, a radial turbine, a mixed flow turbine, or a hydraulic turbine. however, the 2 most common types of turbines used for power generation are the axial and radial turbines. These are shown in the figure below.

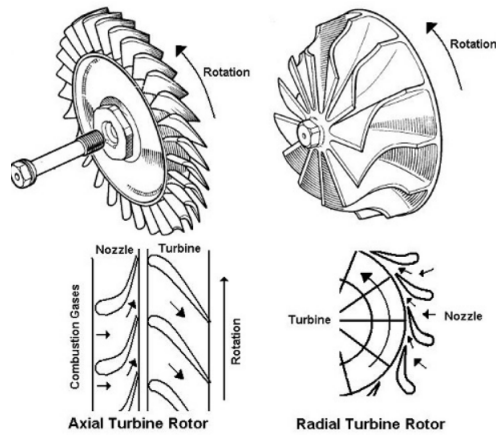


Figure 2.24: A basic schematic of an axial and a radial turbine. In an axial turbine, the fluid flows parallel to the axis of the rotor, whereas in a radial turbine, it flows in the radial direction.

A short comparison table by Evertse et al. shows the differences between the 2 turbine types.


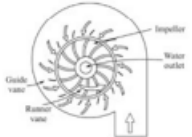
Turbine specifics	Axial flow	Radial flow
		
Pressure ratio per stage	Low	High
Overall pressure ratio	+++	+
Maximum pressure ratio	High	Low
Airflow	High	Low
Size	+	+++
Simplicity	+	+++
Investment costs	+	+++
Efficiency range	>5 MW	<5 MW

Figure 2.25: A brief overview of the differences between axial and radial flow turbines[13]

As can be seen from the table, axial flow turbines are suitable for operations with low pressure ratios per stage but with an overall high pressure ratio. The design of the axial flow turbine is also simpler and it provides a greater power output and is suitable for outputs greater than 5 MW. On the contrary, the radial flow turbine is suitable for applications requiring a higher pressure ratio per stage and a lower pressure ratio overall. It is also more suitable for applications requiring less than 5 MW. Therefore, given the small size of the current system, it is highly likely that a small radial turbine is suitable for the application.

The preliminary sizing can be done via the Balje diagrams. These diagrams were presented by Balje et al.[1] in the year 1962 and have since become part of the standard procedure for the preliminary sizing of turbomachinery. The Balje diagram consists of curves of constant efficiency as a function of the specific speed ( $N_s$ ) and the specific diameter ( $D_s$ ). By selecting an appropriate range for  $N_s$ , the corresponding efficiency curve and  $D_s$  can be found. The Balje diagrams for single stage turbines is as shown in Figure 2.26.



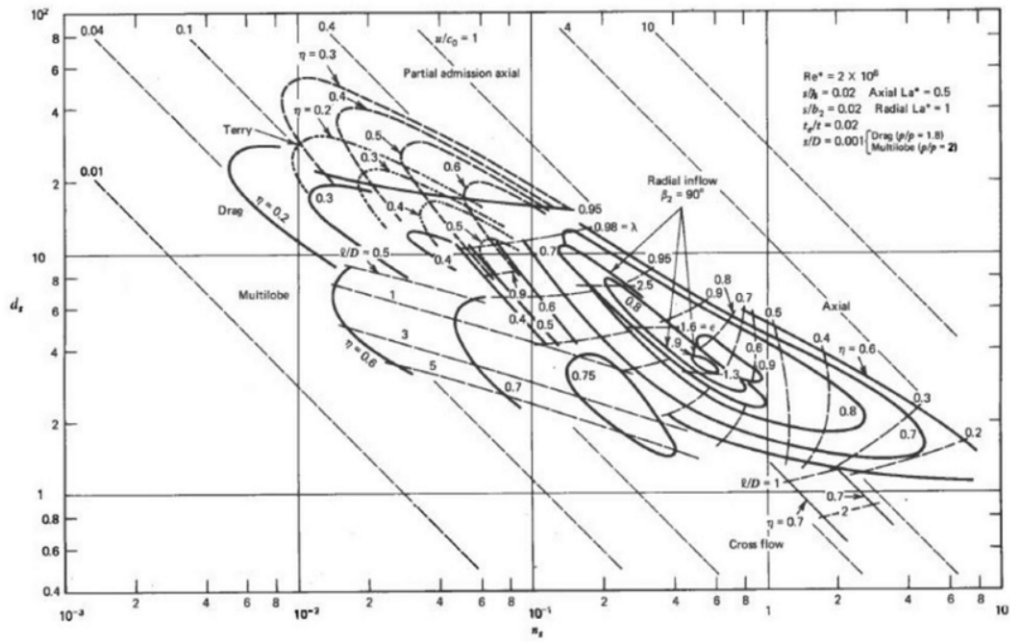


Figure 2.26: Balje Diagram for single stage turbines. The X axis represents the specific speed  $n_s$  and the Y axis represents the specific diameter  $d_s$ [1]

The design procedure for the turbine has been covered in greater detail in Section 5.3.

## 2.9 Conclusion

This chapter presented the relevant basic theory on SOFCs, combustion, ejectors, Heat exchangers and turbomachinery. The basic mathematical models for modelling the components have also been chosen. These choices can be summarised as follows:

- Non-Premixed combustion for pure Hydrogen-Oxygen using a micromix geometry.
- A O-D model for the SOFC.
- An Oxygen re-circulation loop for pre-heating the incoming oxygen and for maintaining the temperature of the SOFC using an ejector
- Integration with a heat exchangers

## Chapter 3

# DESIGN OF THE THERMODYNAMIC CYCLE AND ITS COMPONENTS

### 3.1 Methodology of Approach

This chapter contains the detailed description of the 0-D SOFC model and the H<sub>2</sub>-O<sub>2</sub> thermodynamic cycle. The SOFC has been modelled first since it is the first step to designing the system, as the SOFC sets the inlet boundary conditions and the basic size. This is followed by the design of the thermodynamic cycle by solving the system level mass-energy balances. The results are presented at the end of each section.

### 3.2 SOFC Design

The modelling approach for the fuel cell can be briefly explained as:

- **Structure:** The structure can be modelled as a lumped PEN structure (Positive-Electrode-Negative) as shown below in Figure 3.1. The PEN structure approach makes it easier to model the mass balances over the electrode-electrolyte interface and the overall energy balance.
- **Mass balances:** The mass balances through the PEN structure can be modelled by breaking it down into the air channel (cathode), the fuel channel (anode) and the electrolyte. The output compositions can be determined to enable integration with the combustor. The mass balances shown below are for the case of pure hydrogen and pure oxygen as in Equation 2.3.
- **Electrochemical Model:** The electrochemical model is used to calculate the voltage of the cell. This is done by calculating the various losses as stated above and then calculating the final cell voltage. The power can then be found using the voltage and the current density.
- **Energy Balances:** The energy balance over the entire PEN structure is performed. The SOFC temperature is held constant and equal to the outlet temperature of the anode and cathode. Solving the energy balance helps to calculate the amount of oxygen re-circulation needed to maintain the temperature of the SOFC by cooling it.

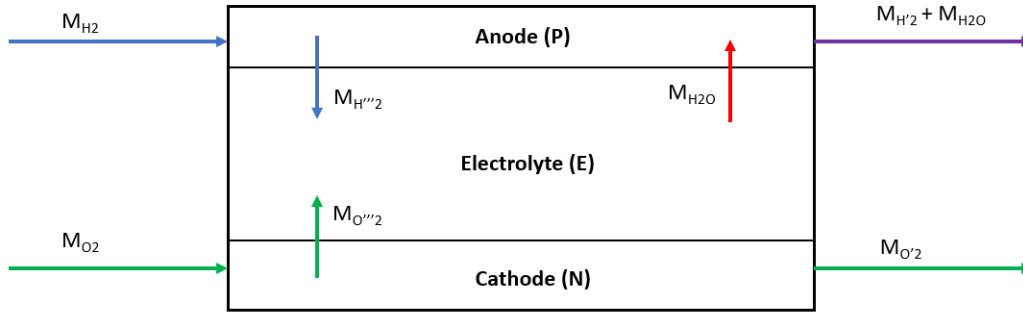


Figure 3.1: PEN Structure of the SOFC

### 3.2.1 Mass Balance

$$\text{Anode} : M_{H_2} = M_{H_2O} + M_{H_2}'' \quad (3.1)$$

$$\text{Cathode} : M_{O_2} - M_{O_2}'' = M_{O_2}' \quad (3.2)$$

$$\text{Electrolyte} : M_{O_2}'' + M_{H_2}'' = M_{H_2O} \quad (3.3)$$

where  $M_{H_2}$  is the inlet molar of hydrogen,  $M_{O_2}$  is the inlet molar flow of oxygen,  $M_{H_2}'$  is the outlet molar flow of hydrogen,  $M_{O_2}'$  is the outlet molar flow of oxygen,  $M_{H_2O}$  is the outlet molar flow of steam,  $M_{O_2}''$  is the amount of oxygen utilised and  $M_{H_2}''$  is the amount of hydrogen utilised

$M_{H_2}''$  can be determined from Faraday's equation 3.4 as:

$$M_{H_2}'' = \frac{j}{nF} \quad (3.4)$$

Where  $n$  is the number of electrons in the Equation 3.1. Then the amount of oxygen ( $M_{O_2}''$ ) used =  $\frac{1}{2} M_{H_2}''$  and the amount of steam  $M_{H_2O} = M_{H_2}''$  as per Equation 3.1.

### 3.2.2 Energy Balance

Assuming no heat loss, the following heat balance can be made:

$$M_{H_2} * h_{H_2} + M_{O_2} * h_{O_2} = (M_{H_2O} + M_{H_2}') * h_{mix} + M_{O_2}' * h_{O_2} + P \quad (3.5)$$

$P$  is the Power in Watts,  $h_{H_2}$  is the inlet molar enthalpy of Hydrogen,  $h_{O_2}$  is the inlet molar enthalpy of Oxygen and  $h_{mix}$  is the molar enthalpy of mixture of Hydrogen and Steam. All molar enthalpy values have the units of  $\frac{J}{mol}$ .

The temperature of the outgoing streams can be calculated from the above energy balance. The Enthalpies can be calculated from the temperature dependant Shomate equation [49].

### 3.2.3 Electrochemical Model

The electrochemical model of the fuel cell can be described by the following equations:

- Nernst Potential: The standard electrode potential or the standard reduction potential at the electrodes is defined at STP. However when the conditions at the electrodes are not at STP, then the output voltage changes. This change is given by the Nernst potential, given earlier in Equation (2.6).
- Activation Losses: The activation losses are caused due to the energy required by the reaction to overcome the activation energy barrier. The current density is given by the Butler Volmer equation, which is given as follows:

$$j = j_0 \left[ \exp\left(\frac{\alpha n F \eta}{RT}\right) - \exp\left(\frac{-\alpha n F \eta}{RT}\right) \right] \quad (3.6)$$

The exchange current densities for the anode ( $j_{0a}$ ) and the cathode ( $j_{0c}$ ) along with their respective Activation energies ( $-E_{a_h}$ ) and ( $-E_{a_o}$ ) are given in [27] as :

$$j_{0a} = \gamma_a \left( \frac{p_{O_2}}{p_0} \right) \left( \frac{p_{h_2}}{p_0} \right) \exp \frac{-E_{a_h}}{RT} \quad (3.7)$$

$$j_{0c} = \gamma_c \left( \frac{p_{O_2}}{p_0} \right)^{0.25} \exp \frac{-E_{a_o}}{RT} \quad (3.8)$$

where  $\gamma_c$  is the pre-exponential factor/fit coefficient (cathode),  $\gamma_a$  is the pre-exponential factor/fit coefficient (anode),  $\alpha$  is the charge transfer coefficient,  $\eta$  is the activation Overpotential,  $T$  is the cell temperature,  $p_0$  is the ambient pressure,  $p_{O_2}$  is the partial pressure of oxygen at the cathode,  $p_{h_2}$  is the partial pressure of hydrogen at the anode and  $p_{h_2O}$  is the partial pressure of steam at the anode

The charge transfer coefficient  $\alpha$  is usually taken as 1/2 in order to assume a symmetric electron charge transfer at the electrode-electrolyte interface. Using this value the Butler-Volmer equation can be simplified to the following equation by using  $\frac{(e^x + e^{-x})}{2} = \text{asinh}(x)$ .

$$j = 2j_{0a} \left( \sinh \frac{nF\eta}{RT} \right) \quad (3.9)$$

$$j = 2j_{0c} \left( \sinh \frac{nF\eta}{RT} \right) \quad (3.10)$$

Thus the overpotential at each electrode  $\eta$  is:

$$\eta_a = \frac{RT}{nF} \left( \text{asinh} \left( \frac{j}{2j_{0a}} \right) \right) \quad (3.11)$$

$$\eta_c = \frac{RT}{nF} \left( \text{asinh} \left( \frac{j}{2j_{0c}} \right) \right) \quad (3.12)$$

The total activation loss ( $V_{act}$ ) is  $\eta_h + \eta_o$ :

$$V_{act} = \frac{RT}{F} \left( \text{asinh} \frac{j}{2j_{0a}} + \text{asinh} \frac{j}{2j_{0c}} \right) \quad (3.13)$$

- Ohmic Losses: The Ohmic losses occur in the fuel cell due to the ohmic resistance of the electrodes and the electrolyte. The ohmic losses are given by:

$$r_{cathode} = \frac{\delta_c}{\kappa_c} \quad (3.14)$$

$$r_{anode} = \frac{\delta_a}{\kappa_a} \quad (3.15)$$

$$r_e = \frac{\delta_e}{20500e(-9030/T)} \quad (3.16)$$

$$r_{total} = r_c + r_a + r_e \quad (3.17)$$

$$V_{ohmic} = jr_{total} \quad (3.18)$$

where  $\kappa_{cathode}$  is the electrical conductivity of cathode,  $\kappa_{anode}$  is the electrical conductivity of anode,  $\delta_{cathode}$  is the thickness of cathode,  $\delta_{anode}$  is the thickness of anode and  $\delta_{electrolyte}$  is the thickness of electrolyte. The equation for the electrolyte resistance has been taken from [38] and [42].

- Concentration/Diffusion losses: The diffusion losses occur due to the difference in the concentration of the reactants in the bulk of the electrolyte vs the surface of the electrodes. The concentration losses give rise to the limiting current density ( $j_l$ ). This is the maximum current density that can be obtained at either electrodes. The expression for the diffusion loss ( $V_{diff}$ ) is given as [46]:

$$V_{diff} = -\frac{RT}{nF} \ln \left( 1 - \frac{j}{j_l} \right); \quad (3.19)$$

The final cell voltage and power density are given as:

$$V_{cell} = E_{nernst} - V_{diff} - V_{act} - V_{ohm} \quad (3.20)$$

$$P_{SOFC} = j * V_{cell} \quad (3.21)$$

Finally, the efficiency of the SOFC is given as:

$$\frac{P_{SOFC}}{m_{H_2} * LHV_{H_2}} \quad (3.22)$$

where  $m_{H_2}$  is the amount of hydrogen consumed as per equation 3.4.

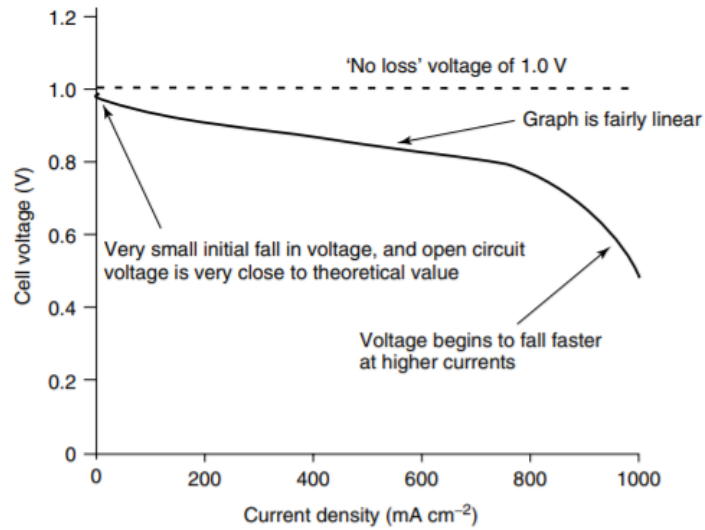


Figure 3.2: FC I-V characteristics [29]

### 3.2.4 Initialising parameters

The SOFC model has been initialized with parameters based on the commercially available Sunfire/Staxera Mk-200 SOFC shown in Figure 3.3. This SOFC housed in the Integrated Stack Module (ISM), is shown in Figure 3.3.



Figure 3.3: 60 cell Mk-200 SOFC on the left and the Integrated Stack Module for housing the SOFC on the right from Sunfire/Staxera [53]

The geometric and electrochemical properties have been taken based on the 3YSZ KeraCell II by Kerafol, that are typically used in the Sunfire/Staxera Mk-200 stack[2],[53].

<b>Geometric Parameters</b>	<b>Value</b>	<b>Units</b>
Number of Cells	60	
Current Density	0.36	$A/cm^2$
Output Current	26.2	A
Cathode Thickness	35e-4	cm
Anode Thickness	35e-4	cm
Electrolyte Thickness	90e-4	cm
Interconnect Thickness	500e-4	cm

<b>Electrochemical Parameters</b>	<b>Value</b>	<b>Units</b>
Cathode Conductivity	12.9e3	$\Omega^{-1} m^{-1}$
Anode Conductivity	30.3e3	$\Omega^{-1} m^{-1}$
Electrolyte Conductivity	20500e(-9030/T))	$\Omega^{-1} m^{-1}$
Limiting Current Density	0.36	$A/cm^2$
Contact Resistance	5e-6	$\Omega m^2$
Pre-exponential Factor (cathode)	7e8	$A/m^2$
Pre-exponential Factor (anode)	4.2e10	$A/m^2$
Activation Energy Cathode	120e3	J/mol
Activation Energy Anode	120e3	J/mol

<b>Stack Inlet Parameters</b>	<b>Value</b>	<b>Units</b>
Anode Inlet Temperature	800	$^{\circ}C$
Cathode Inlet Temperature	650	$^{\circ}C$
Cathode Outlet Temperature	850	$^{\circ}C$
Anode Outlet Temperature	850	$^{\circ}C$
Maximum Operating Temperature	850- 860	$^{\circ}C$
Fuel utilisation factor	0.85	

Table 3.1: Inlet Parameters obtained from [2]

Other assumed parameters have been taken as follows:

<b>Parameter</b>	<b>Value</b>
Oxygen utilisation factor	0.85
Anode gas inlet composition	100% Hydrogen
Cathode gas inlet composition	100% oxygen

Table 3.2: Assumed inlet Parameters

### 3.2.5 Results

Using the initial values presented above, the 0-D model of the SOFC has been designed in MATLAB using the equations presented in Section 2.4. The validation for the model has been presented in the Appendix A.2. The results of the 0-D model are as follows:

Parameter	Value	Unit
SOFC Power Output	1.15	kW
Output Voltage(cell)	0.73	V
Output Voltage(stack)	44.06	V
Inlet Mass Flow Oxygen	3.91	g/s
Inlet Mass Flow Hydrogen	0.019	g/s
Outlet Mass Flow Oxygen	3.78	g/s
Outlet Mass Flow Hydrogen	0.0029	g/s
Outlet Mass Flow Steam	0.14	g/s
SOFC efficiency	58.6	%

Table 3.3: Results of the H<sub>2</sub>-O<sub>2</sub> thermodynamic cycle

These results are the first step towards the design of the overall H<sub>2</sub>-O<sub>2</sub> cycle. The mass and energy balances can be performed to determine all thermodynamic state points. The next section describes this process of the design of the H<sub>2</sub>-O<sub>2</sub> thermodynamic cycle.

### 3.3 Thermodynamic Cycle Design

The process flow diagram of the H<sub>2</sub>-O<sub>2</sub> cycle is shown in Figure 3.4 as follows.

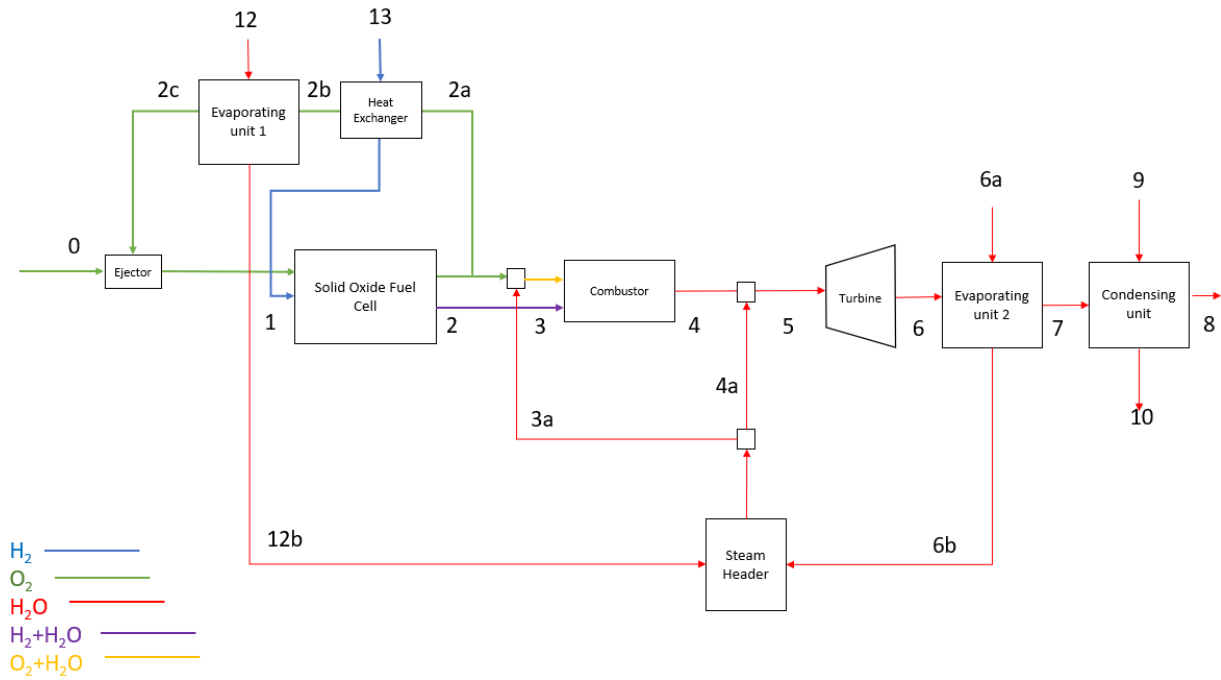


Figure 3.4: Process flow diagram of the H<sub>2</sub>-O<sub>2</sub> thermodynamic cycle

The gases have been assumed to be ideal. The enthalpy calculation has been performed using the Shomate equation[49], which is given as follows:

$$\Delta h = A + B \frac{t^2}{2} + C \frac{t^3}{3} + D \frac{t^4}{4} + \frac{E}{t} + F \quad (3.23)$$

$$\Delta h = h_T - h_{298.15} \quad (3.24)$$

$$t = \frac{T}{1000} \quad (3.25)$$

where  $A, B, C, D, E$  and  $F$  are constants which are determined experimentally and vary for each compound. The enthalpy  $\Delta h$  obtained is in  $\frac{KJ}{mol}$

From Figure 3.4, hydrogen and oxygen enter the SOFC at **1** and exit at **2**. The mass and energy balance over the SOFC can be calculated as follows:

$$(m_{H_2})_1 + (m_{O_2})_1 = (m_{H_2O})_2 + (m_{H_2})_2 + (m_{O_2})_2 \quad (3.26)$$

$$(m_{H_2} * h_{H_2})_1 + (m_{O_2} * h_{O_2})_1 = (m_{H_2O+H_2} * h_{H_2O+H_2})_2 + (m_{O_2} * h_{O_2})_2 + P_{SOFC} \quad (3.27)$$

where  $m_{H_2}, m_{O_2}, m_{H_2O}$  represent the mass flows and  $h_{H_2}, h_{O_2}, h_{H_2O}$  represent the enthalpies of hydrogen, oxygen and steam respectively. Similarly,  $P_{SOFC}$  represents the power produced by the SOFC.

To ensure complete stoichiometric combustion in the combustor, the amount of oxygen given to the combustor is kept at half the amount of hydrogen given in moles represented by  $M$  at **3**.

$$(M_{O_2})_3 = \frac{1}{2}(M_{H_2})_3 \quad (3.28)$$

The remaining oxygen at **2** is recirculated to the inlet of the SOFC using the ejector. To make sure the correct inlet temperature of the SOFC is reached, the oxygen is cooled down by passing it through a heat exchanger and an evaporator between **2a** and **2c**. The correct temperature needs to be reached at the secondary inlet of the ejector at **2c** to ensure that the desired SOFC inlet temperature is reached. This is calculated by the following mass-energy balance.

$$(m_{O_2})_{2c} = (m_{O_2})_1 - (m_{O_2})_0 \quad (3.29)$$

$$(m_{O_2} * h_{O_2})_{2c} = (m_{O_2} * h_{O_2})_1 - (m_{O_2} * h_{O_2})_0 \quad (3.30)$$

The total heat extracted ( $Q_{total}$ ) from the recirculating oxygen stream between **2a** and **2c**, is used to preheat the hydrogen to the inlet temperature of the SOFC and produce saturated steam at 1 bar. The total heat load or duty for the heat exchangers can be calculated in this manner.

$$Q_{total} = (m_{O_2} * h_{O_2})_{2a} - (m_{O_2} * h_{O_2})_{2c} \quad (3.31)$$

The remaining oxygen is mixed with steam generated in the evaporator via the steam header and sent to the combustor at **3**. By controlling the amount of the steam, the inlet temperature of the combustor can be controlled. The oxygen-steam mixture enters the combustor along with the hydrogen-steam mixture from the SOFC, and then the combustion takes place between **3** and **4**. The outlet temperature of the combustor can then be calculated from the following enthalpy balance.

$$(m_{H_2O})_4 = (m_{(O_2+H_2O)})_3 + (m_{(H_2+H_2O)})_3 \quad (3.32)$$

$$(m_{H_2O} * h_{H_2O})_4 = (m_{(O_2+H_2O)} * h_{(O_2+H_2O)})_3 + (m_{(H_2+H_2O)} * h_{(H_2+H_2O)})_3 \quad (3.33)$$

At the exit of the combustor at **4**, steam enters the turbine. The power produced by the turbine  $P_{turbine}$  at a fixed expansion ratio can be calculated as follows.

$$P_{turbine} = [(m_{H_2O} * h_{H_2O})_5 - (m_{H_2O} * h_{H_2O})_6] \quad (3.34)$$

The turbine produces power and the exit steam, having residual heat left, is passed through an evaporator at **6**, to generate more steam. This steam is then sent back to the turbine via the steam header to produce more power at **5**. This increases the mass flow of steam through the turbine, albeit at a reduced inlet temperature. The amount of steam generated depends on the duty of the heat exchanger, which is defined as:

$$Q_{evaporator} = m_{H_2O} * [h_{out} - h_{in} + h_{latent}] \quad (3.35)$$

From this, the new inlet enthalpy and mass flow at the inlet of the turbine are calculated via:

$$(m_{H_2O})_5 = (m_{H_2O})_4 + (m_{H_2O})_{4a} \quad (3.36)$$

$$(m_{H_2O} * h_{H_2O})_5 = (m_{H_2O} * h_{H_2O})_4 + (m_{H_2O} * h_{H_2O})_{4a} \quad (3.37)$$

The steam exiting the evaporator at **7**, is sent to a condenser. The condenser produces water at **8**. This is done to avoid exhausting very low pressure steam directly into the atmosphere. The heat load of the condenser can



be calculated similar to that of the evaporator as in Equation 3.35. This water can then be pumped back to the source at **12** or to a storage and can be re-introduced into the cycle if needed.

Finally, the thermal efficiency ( $\eta_{LHV}$ ) of the thermodynamic cycle can be calculated based on the Lower Heating Value (LHV) of hydrogen as follows:

$$\eta_{LHV} = \frac{P_{SOFC} + P_{turbine}}{LHV_{H_2}} \quad (3.38)$$

By iteratively solving the above equations, all the state points for thermodynamic cycle have been calculated.

### 3.3.1 Initialising Parameters

The thermodynamic cycle shown in Figure 3.4 is solved by using the following initial parameters:

SOFC Parameters	Value	Unit
Inlet Mass Flow Oxygen	3.91	g/s
Inlet Mass Flow Hydrogen	0.019	g/s
Outlet Mass Flow Oxygen	3.78	g/s
Outlet Mass Flow Hydrogen	0.0029	g/s
Outlet Mass Flow Steam	0.14	g/s
SOFC Power Output	1.15	kW

Assumed Parameters	Value	Unit
Hydrogen Inlet Temperature	15	°C
Oxygen Inlet Temperature	15	°C
Evaporator Outlet Steam Temperature	100	°C
LHV of Hydrogen	240	$\frac{kJ}{mol}$
Pressure Loss across Components	1	%
Isentropic Efficiency of Turbine	90	%

Table 3.4: Parameters for initialising the design of the H<sub>2</sub>-O<sub>2</sub> thermodynamic cycle

The SOFC parameters have been obtained from the results of the 0-D SOFC model. The inlet temperatures for hydrogen and oxygen have been kept at 15 °C, based on previous inlet temperatures taken by Schouten et al. and Evertse et al.[13]. The temperature of steam generation is kept at 100 °C since this ensures a maximum amount of steam generated for cooling at a given heat exchanger duty. The isentropic efficiency of the turbine has been kept at a high value of 90 % [17].

### 3.3.2 Results

Using these parameters, the mass-energy balances given in Section 3.3 have been solved in MATLAB and the thermodynamic cycle has been made as shown below in Figure 3.5.

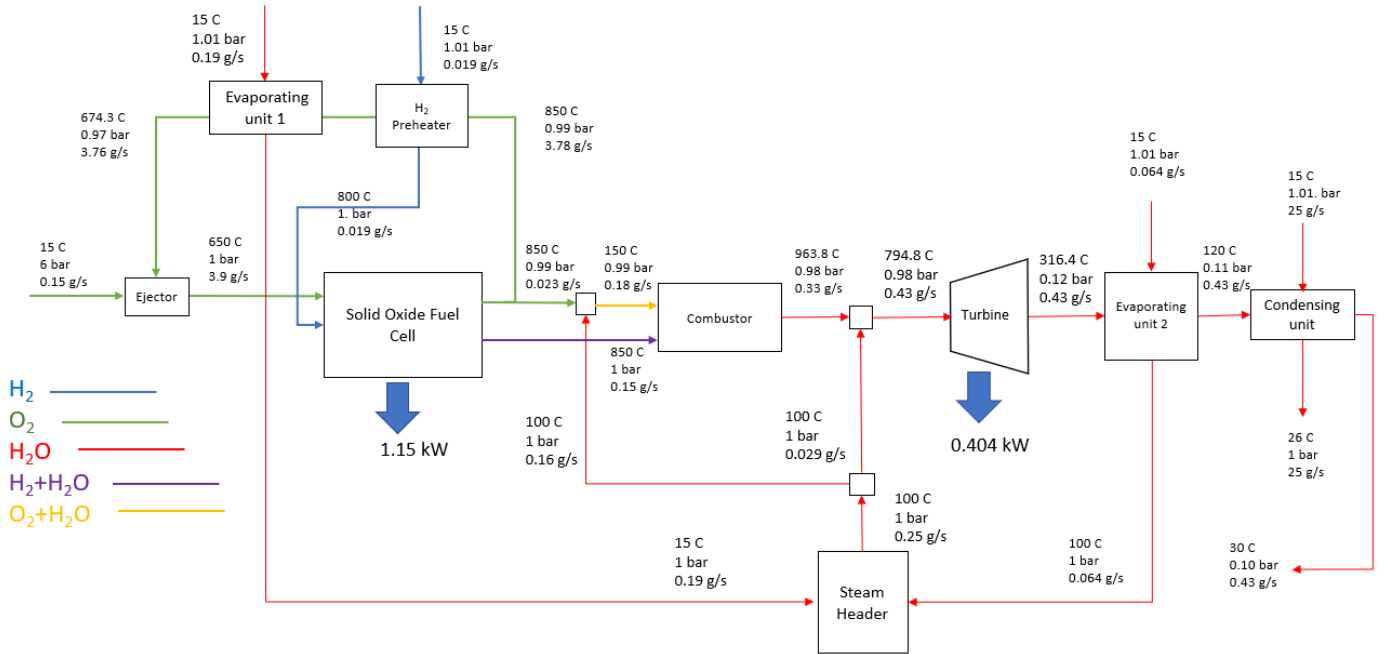


Figure 3.5: Process Flow Diagram of the designed H<sub>2</sub>-O<sub>2</sub> thermodynamic cycle

It can be observed that the cycle produces a total power of 1.56 kW and the only by-product is water. the total thermal efficiency of the cycle is 67.28 %.

Parameters	Value	Unit
SOFC Power Output	1.15	kW
Turbine Power Output	0.404	kW
SOFC Efficiency	58.6	%
Total Power Output	1.56	kW
Total Thermal Efficiency	67.28	%

Table 3.5: Results of the designed H<sub>2</sub>-O<sub>2</sub> thermodynamic cycle

# Chapter 4

## MICROMIX COMBUSTOR DESIGN

This chapter deals with the design of a micromix type H<sub>2</sub>-O<sub>2</sub> combustor. This is followed by a simple CFD simulation of the H<sub>2</sub>-O<sub>2</sub> combustor. The reference type or geometry of the H<sub>2</sub>-O<sub>2</sub> combustor has been chosen as the micromix combustor as stated in Section 2.5. This is to ensure perfect mixing of the hydrogen and oxygen in stoichiometric amounts for complete combustion.

### 4.1 Basic Requirements and Design Constraints of a Combustor

The following list of functional requirements has been summarized to show the important criteria that the H<sub>2</sub>-O<sub>2</sub> combustor should meet:

- Minimum pressure drop from SOFC outlet to turbine inlet
- Turbine inlet temperature should be reached but should not be exceeded.
- Stable flame shape should be obtained.
- Mixing of fuel and oxidiser should be perfect or close to perfect in order to have combustion at stoichiometric conditions.

As stated in Section 2.5, the micromix combustor utilises the concept of jets in crossflow. Therefore, to design and size the geometry of the micromix combustor, it is important to introduce the basic concepts behind jets in cross flow, particularly in the context of combustor applications.

### 4.2 Jets in Crossflow

Jets in crossflow is a canonical flow in fluid dynamics. It consists of 2 orthogonal fluid jets impinge into each other and mix. Usually the flow with the larger length scale is termed as the crossflow and the smaller flow is termed as the jet. This can be seen in Figure 4.2.

The earliest contributions to this topic have been made by Holdeman and Liscinsky [32],[33],[23],[24], in terms of the effects of the cross jet momentum ratios, the shape and spacing of the injectors.

The following section summarises the most important factors that affect the jets in crossflow:

- Cross jet momentum ratio: It is defined as the root of the ratio of the momentum of the jet to that of the cross flow. It is given as:

$$R = \left[ \frac{(\rho u_{jet}^2)}{(\rho u_{cf}^2)} \right]^{0.5} \quad (4.1)$$

The value of R determines the penetration depth of the jet into the cross flow. The cross jet momentum ratio is one of the most important factors impacting the mixing ability [23].

- Shape of the injectors: The shape of the injector induces turbulence into the fluid flowing through it. Salewski et al.[43] compared 4 differently shaped holes, namely, square, elliptical, circular and triangular. They noted that the maximum turbulence added was by elliptical and square holes due to their sharp edges and sudden change in curvature leading to the formation of small wakes in the flow. This was shown to increase the mixing intensity of the cross-flow due to higher entrainment. Another factor linked to the shape of the injection holes is the aspect ratio ( $AR$ ). It is defined as:

$$AR = \text{Width}/\text{Length} \quad (4.2)$$

Salewski et al. [43] noted that the high aspect ratio ellipticals, had higher mixing than their low aspect ratio counterparts.

- Total Area of injection (Area per injection hole \*number of holes): The total area of injection determines the velocity at the inlets for a fixed volume flow.

### 4.3 Geometry Design

A simple conceptual geometry was developed first to envision the  $H_2$ - $O_2$  micromix combustor. This geometry is shown in Figure 4.1

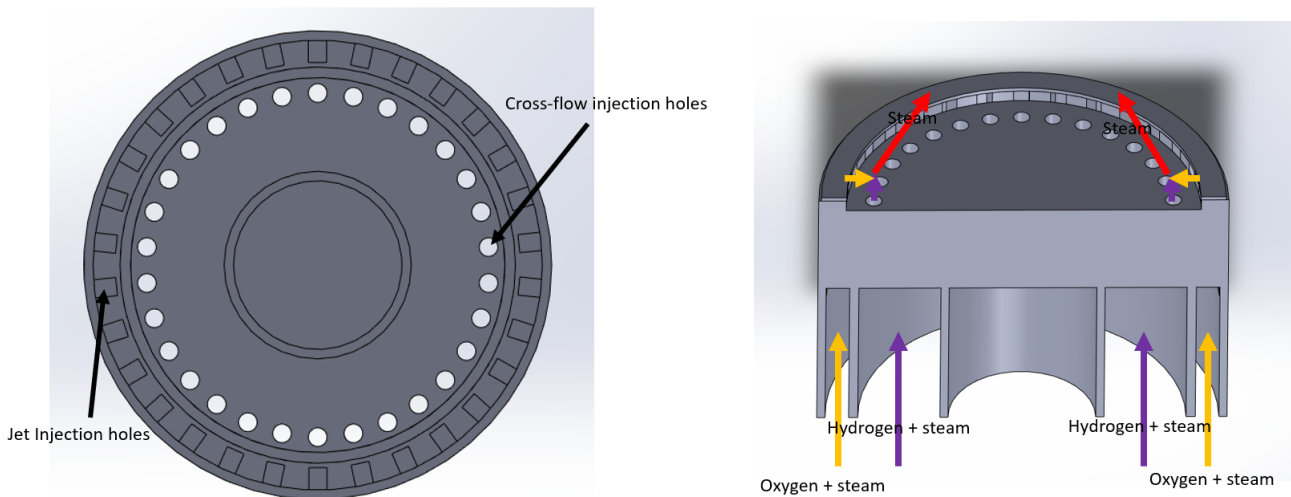


Figure 4.1: Top view (left) of the conceptual micromix combustor geometry displaying the jet injection holes and the cross-flow injection holes. The cut section (right) of the conceptual micromix combustor geometry displaying how the fuel and oxidiser streams enter the combustor through the injection holes and mix to form steam.

The conceptual geometry consists of an inner cylindrical opening through which the  $H_2+H_2O$  stream is sent to one injection holes. The outer cylinder forms an annular region through which the  $O_2+H_2O$  stream is sent to the other set of injection holes. The micro injection holes cause the mixing to occur on a micro scale. Round injection holes have been kept for simplicity. This can be seen in the following figure.

Following this conceptual design, a procedure is employed to accurately size the geometry according to the current application. The objective is to optimize the value of the cross jet momentum ratio ( $R$ ) in such a way that the jet ( $O_2 + H_2O$ ) and cross-flow ( $H_2 + H_2O$ ) mix completely to ensure stoichiometric combustion. The following design procedure is employed:

- Reference areas: First the total diameter of the combustor can be fixed according to the inlet of the turbine. Similarly, the inner ( $A_i$ ) and outer annular( $A_o$ ) areas can be fixed from the size of the outlet connections of the Integrated Stack Module of the SOFC.(Refer Figure 3.3)
- Inlet velocities : The velocity inlet for the 2 streams can be calculated from the continuity equation since the mass flows are known from the process flow diagram of the system and the inlet areas have been

fixed.

$$u_i = \frac{m_{(H_2+H_2O)}}{\rho_{(H_2+H_2O)} * [A_i]} \quad (4.3)$$

$$u_o = \frac{m_{(O_2+H_2O)}}{\rho_{(O_2+H_2O)} * A_o} \quad (4.4)$$

Using the inlet mass flow rates of the two streams, the volume flow rates ( $V_{jet}$  and  $V_{cf}$ ) can be calculated.

$$V_{jet} = \frac{m_{jet}}{\rho_{jet}} \quad (4.5)$$

$$V_{cf} = \frac{m_{cf}}{\rho_{cf}} \quad (4.6)$$

Using these volume flow rates, the velocity ratio can be found as follows:

$$\frac{V_{jet}}{V_{cf}} = \frac{u_{jet} d_{jet}^2}{u_{cf} d_{cf}^2} \quad (4.7)$$

To obtain an optimum value of  $R$ , it is imperative to correctly size the injection holes for both the jets and the cross flow. Assuming that the jet completely penetrates the cross-flow, the height or diameter of the cross-flow can be scaled with the penetration depth  $Y$ . By assuming that  $Y$  is equal to the critical penetration depth  $Y_{crit}$ , it is assumed that the jet penetrates all the way into the crossflow, which is equal to the crossflow diameter. This can be seen in the following schematic.

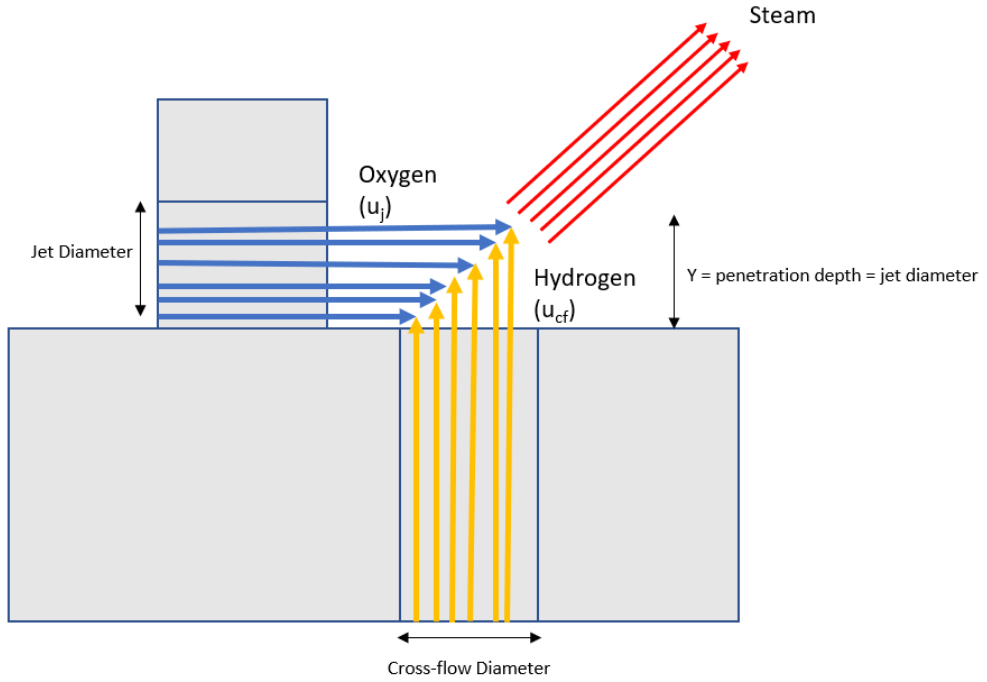


Figure 4.2: The oxygen jet with velocity  $u_j$  completely penetrates the hydrogen crossflow with velocity  $u_{cf}$ . The maximum penetration  $Y$  is equal to the crossflow diameter  $d_{cf}$ .

The penetration depth of the jet  $Y$  can be calculated via the following equation given by Lefebvre et al.[30] for a flow ejecting out of an annular liner through an orifice into a crossflow:

$$Y = 1.15 * d_j * R \sin \theta \quad (4.8)$$

$$\sin^2 \theta = \frac{C_D}{C_{D\infty}} = \theta \quad (4.9)$$

where  $d_j$  is the diameter of the jet injection hole. Here  $\theta$  is the angle formed by the jet with the vertical axis and  $C_D$  is the discharge coefficient which is calculated as:

$$C_D = \frac{1.25(K - 1)}{4K^2 - K(2 - \alpha)^2} \quad (4.10)$$

where  $K$  is the ratio of the jet velocity ( $u_j$ ) to the velocity at the inlet of the annulus ( $u_o$ ) and is known as the hole pressure loss factor. The discharge coefficient reaches its asymptotic value  $C_{D\infty}$  as  $K$  approaches infinity. This can be seen in the following figure. Here the injection holes are taken as plain holes for simplicity.

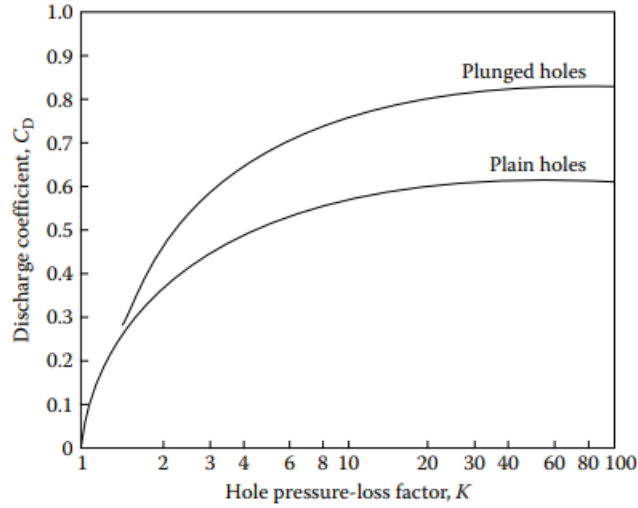


Figure 4.3: Hole pressure loss factor vs discharge coefficient

Using the above plot,  $C_{D\infty}$  is taken as 0.625.  $\alpha$  is defined as the ratio of the jet mass flow rate to the annulus mass flow rate. It is shown below:

$$\alpha = \frac{m_{jet}}{m_{annulus}} \quad (4.11)$$

Therefore, using the volume flow ratio and substituting the value of penetration depth  $Y$  in  $d_{cf}$ , the velocity ratio and the corresponding diameter ratio can be calculated by applying the continuity equation as follows:

$$\frac{V_{jet}}{V_{cf}} = \frac{u_{jet} d_{jet}^2}{u_{cf} d_{cf}^2} \quad (4.12)$$

$$\frac{u_{cf}}{u_{jet}} = \left(\frac{V_{jet}}{V_{cf}}\right) * \left(\frac{\rho_{jet}}{\rho_{cf}}\right) * (1.15^2) * (\sin\theta)^2 \quad (4.13)$$

Now by fixing the Reynolds number at the inlet of either pair of injection holes, the inlet velocities and diameters can be calculated. The geometry and the inlet conditions are now completely defined.

### 4.3.1 Results

Two configurations of the combustor have been made. These are shown in Figure 4.4

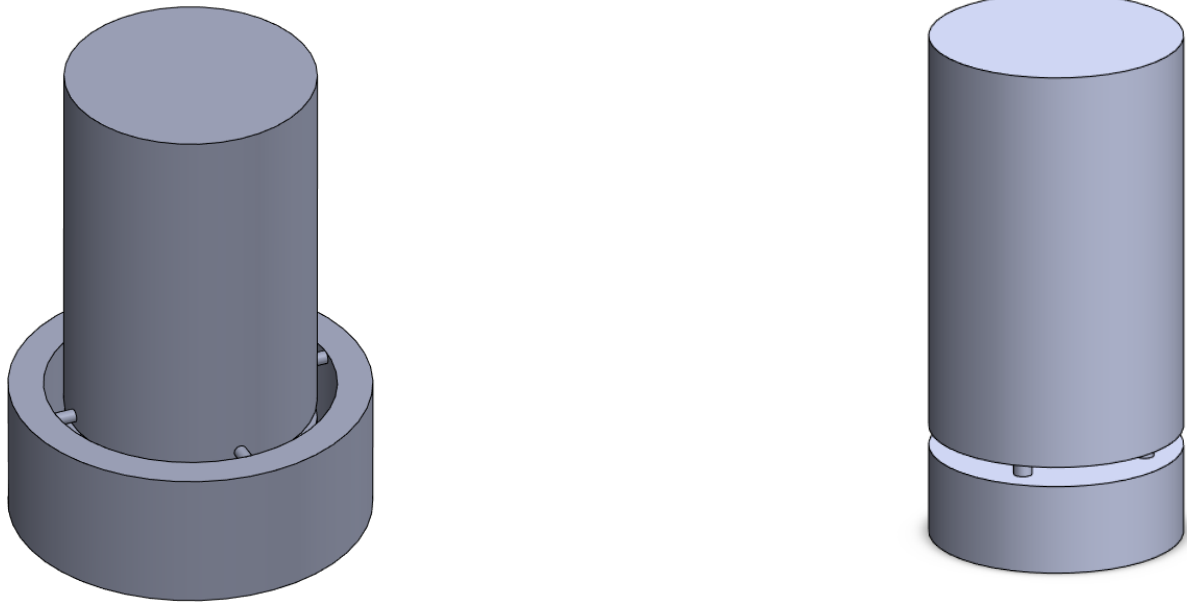


Figure 4.4: Isometric view of the Micromix combustor geometries - configuration 1 (left) and configuration 2 (right)

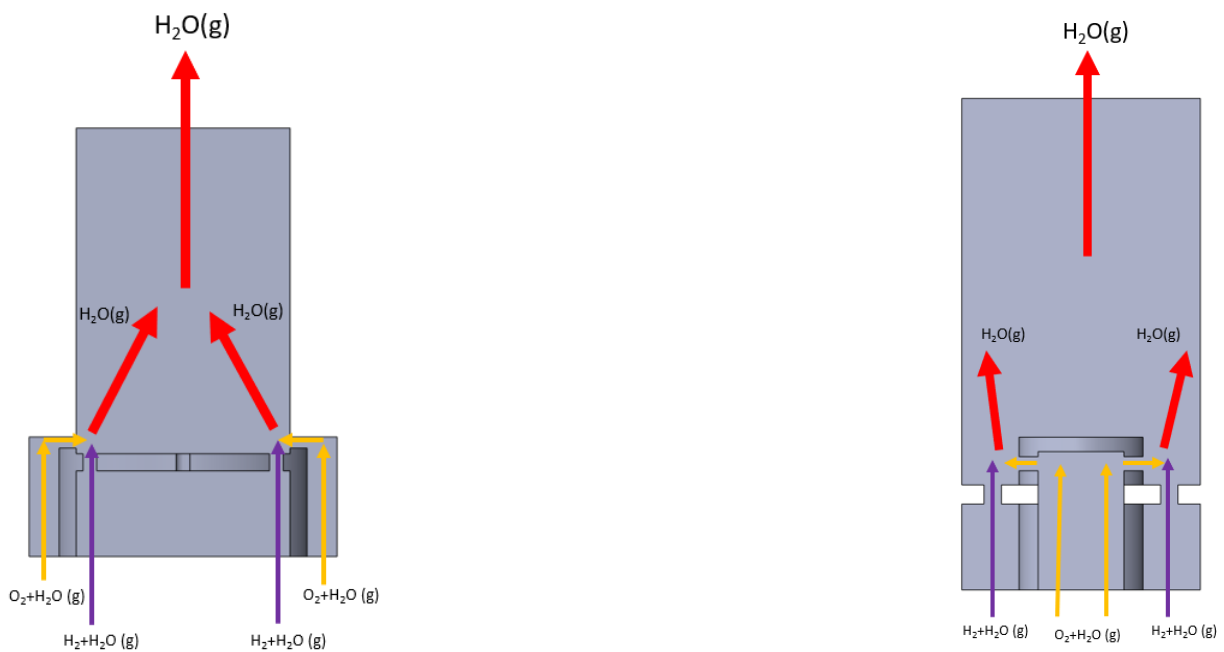


Figure 4.5: Cut-section view of the Micromix combustor geometries - configuration 1 (left) and configuration 2 (right)

Between the 2 configurations, the only difference is the position of the jet injection holes. In the first configuration, they are positioned close to the wall and in the second configuration, they are placed centrally. The diameters of the injection holes in configuration 2 are larger than the corresponding ones in configuration 1. Furthermore, distance between the injection hole pairs is also comparatively larger in configuration 2. These dimensions and the inlet conditions are summarised as follows:

<b>Geometric parameter</b>	<b>Config 1</b>	<b>Config 2</b>
Length	50 mm	51.5 mm
Total Diameter	25 mm	25 mm
Outer Annulus Diameter	36 mm	25mm
Inner Annulus Diameter	25 mm	9 mm
Jet injection diameter	1.3 mm	1.5 mm
Crossflow Inlet Diameter	1.6 mm	1.8 mm
Wall Thickness	2 mm	2 mm
Distance between Hole Pairs	1.45 mm	3.3 mm
<b>Inlet Parameter</b>	<b>Config 1</b>	<b>Config 2</b>
Inner Annulus velocity	1.91 m/s	5.81 m/s
Outer Annulus velocity	1.03 m/s	2.63 m/s

Table 4.1: Geometric and Inlet parameters of the designed H<sub>2</sub>-O<sub>2</sub> micromix combustor

Using these geometries, the CFD analysis can be performed. The aim of the analysis is to check if the designed geometries are producing perfect mixing, minimal pressure loss, a stable flame shape, the correct adiabatic flame temperature (964 °C) while avoiding the formation of local hot spots.(Refer Figure 3.5 and Section 4.1 for the functional requirements of the combustor).

## 4.4 CFD Analysis

### 4.4.1 Mesh Setup

The geometry shown in Figure 4.4 has been divided into four symmetrical parts, and the symmetry boundary condition has been applied on the walls.

To setup the mesh for the simulation for the micromix geometry, a fine tetrahedral mesh at the inlet of the jet and crossflow alongwith the mixing region has been generated. Since the aim of the simulation is to see the effective mixing, the mesh size in the mixing region has been kept fine, corresponding to a  $y^+$  value of 20. Usually a  $y^+$  value of 30 or greater is used in cases of free stream turbulence away from the walls. The  $y^+$  values at the walls are kept at 4. This has been done to resolve any boundary layer formation at the walls. Standard wall functions have been switched on.

### 4.4.2 Initialising Parameters

The inputs for the CFD analysis are as follows:

<b>Inlet Parameter</b>	<b>Config 1</b>	<b>Config 2</b>
Jet Inlet Velocity	93 m/s	73 m/s
Crossflow Inlet Velocity	155 m/s	120 m/s
Cross Jet Momentum Ratio	1.07	1.07
Inner Annulus Velocity	1.91 m/s	5.81 m/s
Outer Annulus Velocity	1.03 m/s	2.63 m/s
Crossflow Inlet Temperature	850 °C	850 °C
Jet Inlet Temperature	425 °C	425 °C
Mole Fraction Inlet Hydrogen	15 %	15 %
Mole Fraction Inlet Oxygen	7.2 %	7.2 %
Crossflow Inlet Reynolds Number	851	670
Jet inlet Reynolds Number	3910	3079.4
Inlet Turbulence Intensity	5 %	5 %

Table 4.2: Input conditions for the combustor



### 4.4.3 Results

The mesh generated for the CFD analysis can be seen in Figure 4.6

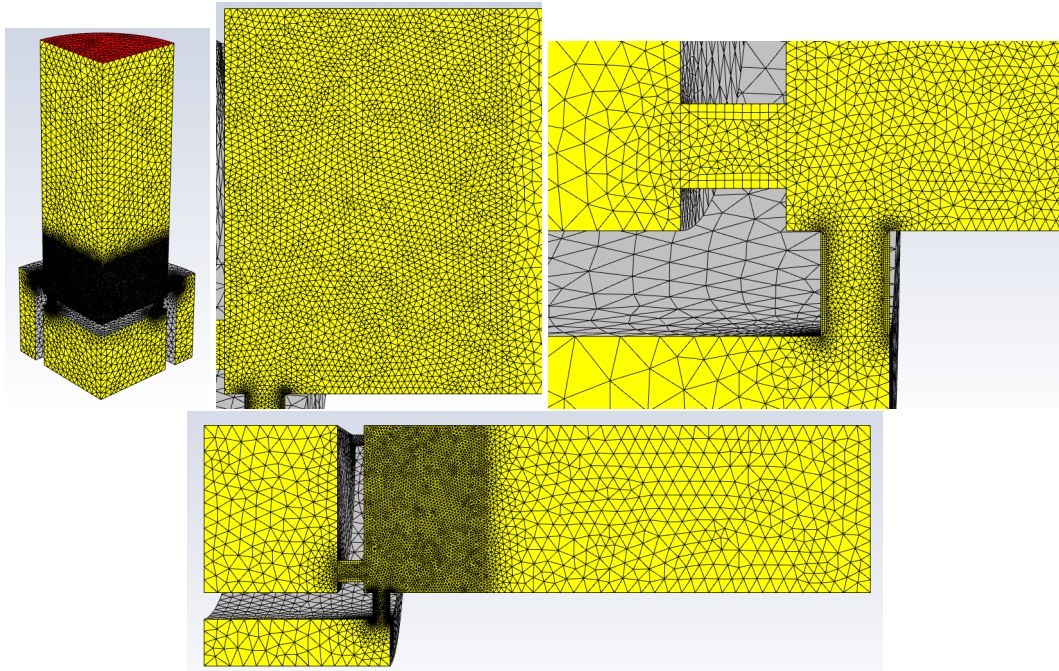


Figure 4.6: Mesh-configuration 1

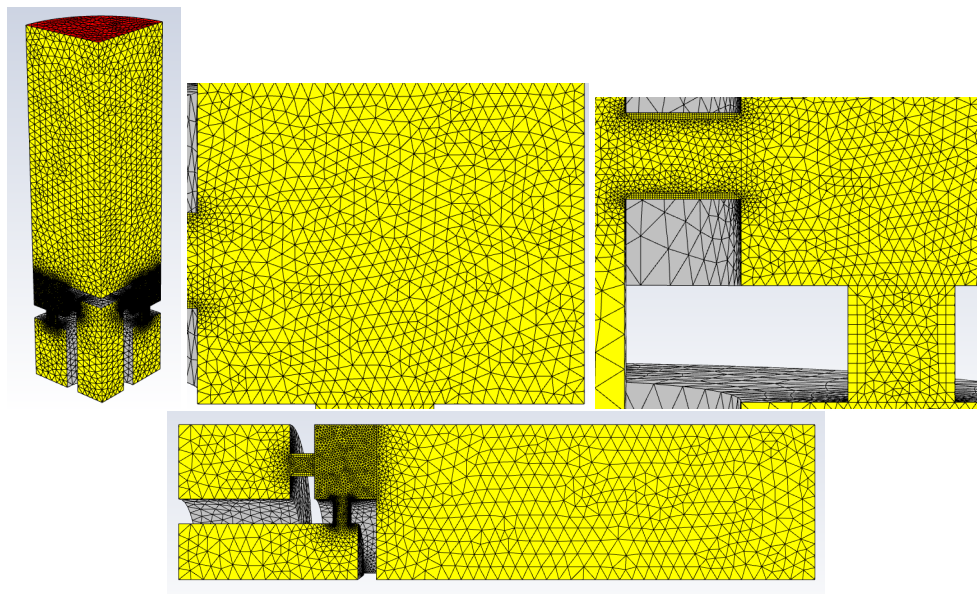


Figure 4.7: Mesh-configuration 2

The mesh statistics are as follows:

Parameter	Config 1	Config 2
Number of Elements	372612	275865
Number of Nodes	85746	69019

Table 4.3: Mesh statistics of updated geometry

After running a steady-state analysis on both the configurations, the following observations can be noted:

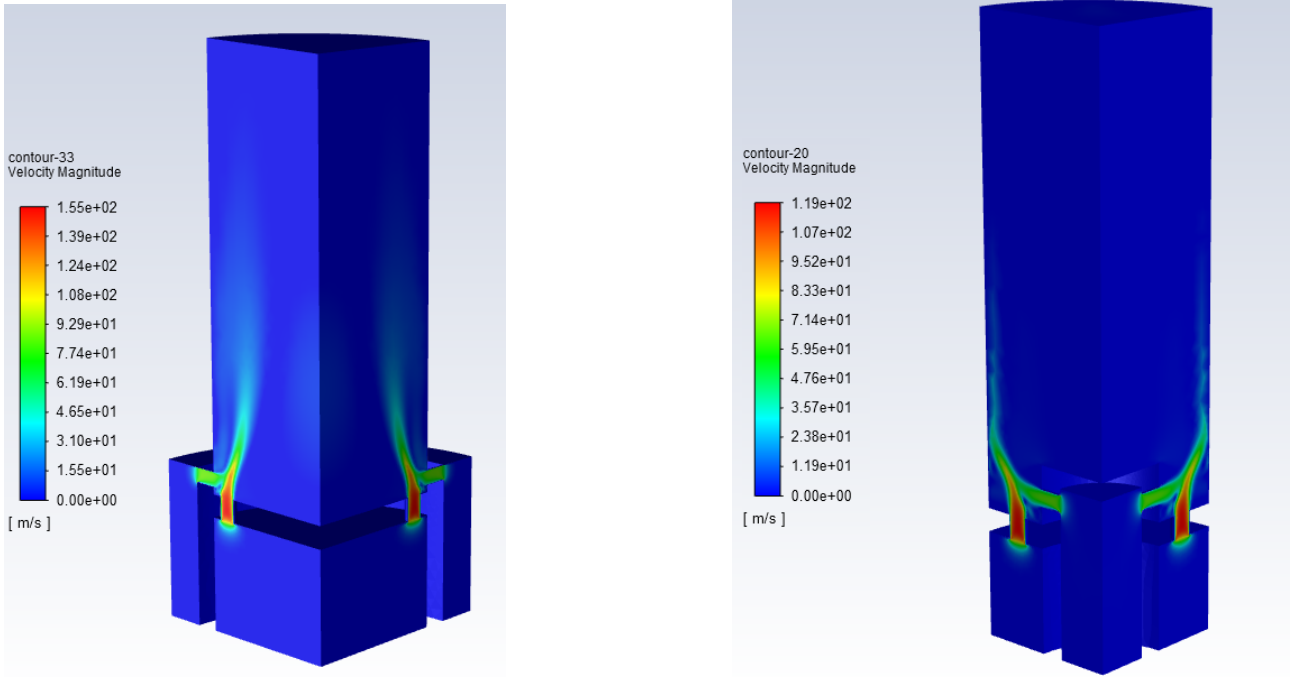


Figure 4.8: Contours of Velocity - configuration 1(left) and configuration 2(right). configuration 1 has higher velocities through the injection holes as compared to configuration 2.

- Contours of Velocity: From the contours of velocity, it can be seen that the velocity through the injection holes in configuration 1 is nearing a maximum of 155 m/s. This velocity corresponds to a Reynolds Number of 3910. Configuration 2 on the other hand has a maximum crossflow velocity of 120 m/s, a corresponding Reynolds number of 3080. This is due to the larger diameter of the injection holes in configuration 2. This has been done to lower the velocity through of the injection holes, to avoid large pressure drops, while still keeping the crossflow turbulent. The following table tabulates the total pressure drop across both configurations.

Stream	Pressure Drop	Unit
Hydrogen Config. 1	20	mbar
Oxygen Config. 1	20	mbar
Hydrogen Config. 2	11	mbar
Oxygen Config. 2	13	mbar

Table 4.4: Total pressure drop across configuration 1 and 2 for hydrogen and oxygen

It can be observed that the total pressure drop across configuration 1 higher than the total pressure drop across configuration 2. This is because of the reduced velocities of the crossflow and jet through the injection holes. Therefore, configuration 2 is preferred over configuration 1 due to the lower pressure drop.

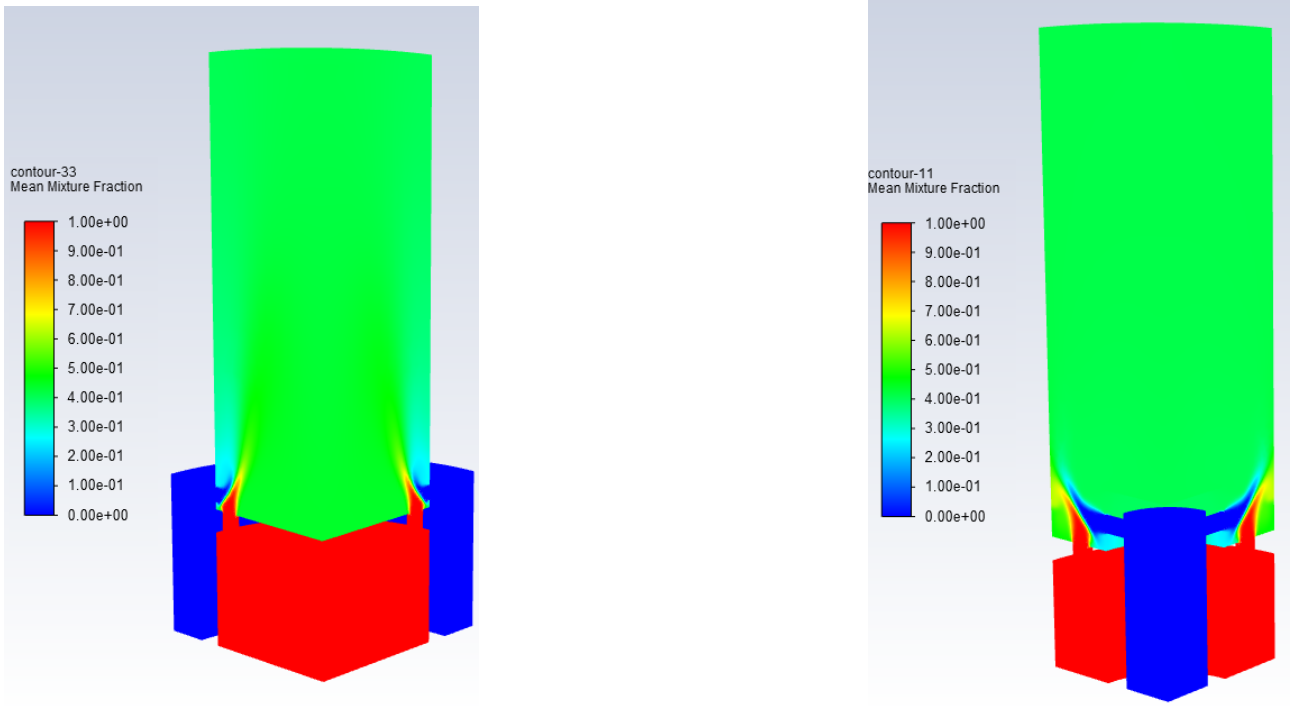


Figure 4.9: Contours of Mixture Fraction- configuration 1(left) and configuration 2(right). configuration 1 has some unmixed oxygen near the walls due to the deflection of the oxygen jet. This is not present in configuration 2

- Contours of Mixture fraction: The contours of mixture fraction, for both configuration 1 and 2 indicate that a constant value of the mixture fraction is being reached, immediately after the mixing of the fuel and oxidiser. This means that complete and uniform mixing has been achieved. To see how close mixture fraction value is to the stoichiometric mixture fraction of 0.43, the following plot is presented.

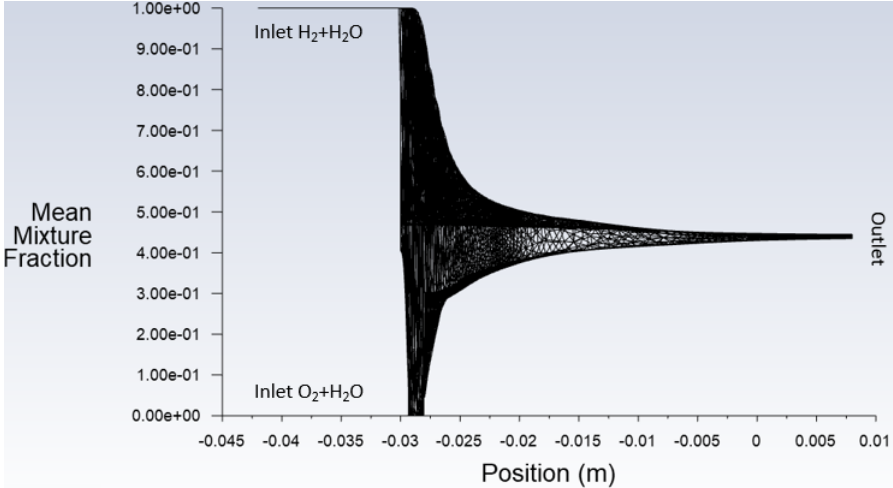


Figure 4.10: Mean mixture fraction vs axial position - configuration 1

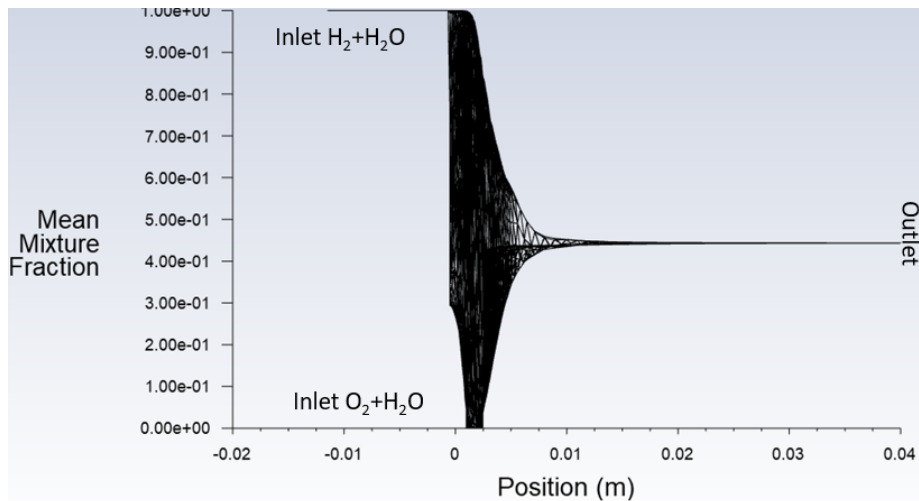


Figure 4.11: Mean mixture fraction vs axial position - configuration 2

From both the plots, it can be observed that the mixture fraction obtains a value of 0.45 along the faces of the symmetry walls of the combustor in the axial direction towards the outlet. Therefore, the requirement of stoichiometric mixing is fulfilled. The outlet of the combustor only consists of the product, which in this case is steam. Furthermore, configuration 2 has superior mixing as compared to configuration 1. This is evident from the fact that the mixture fraction converges to the value of 0.45 much faster for configuration 2 than for configuration 1. A possible reason for this could be the higher velocities through the injection holes in configuration 1 coupled with the smaller distances between the hole pairs leading to the deflection of the  $O_2$  jet. This can be seen as unmixed oxygen near the walls in Figure 4.12.

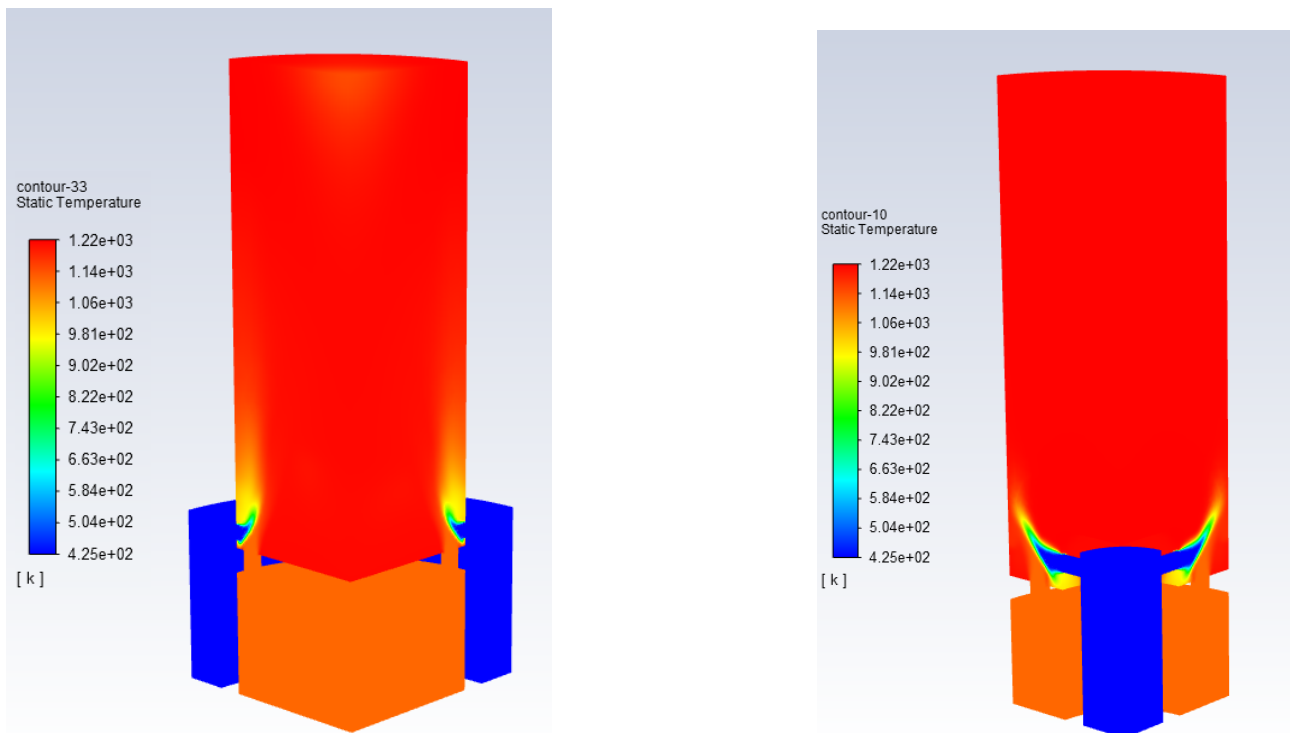


Figure 4.12: Contours of Temperature - configuration 1(left) and configuration 2(right). configuration 1 has jets placed near the combustor walls while configuration 2 has centrally mounted jets.

- Contours of temperature: The contours of temperature indicate that both the configurations reach an adiabatic flame temperature of 960 °C. However, upon comparing the two configurations, it can be observed that the in configuration 1, the flame is formed right next to the combustor walls. This is a

cause for concern, since it could lead to the formation of local hot-spots and lead to deterioration of the wall material. This issue does not exist in configuration 2 , by virtue of the centrally located injection holes. Therefore, in this case, configuration 2 is recommended over configuration 1.

In conclusion, due to the larger injection hole diameters and increased distance between the hole pairs, configuration 2 has superior mixing and a lower pressure drop as compared to configuration 1. Additionally, the centrally positioned jets, keep the flame formation away from the combustor walls.

# Chapter 5

## DESIGN OF SUPPLEMENTARY COMPONENTS

This chapter introduces the methodology used for the design of the heat exchangers, the design of the ejector and the sizing of the turbine.

### 5.1 Heat exchanger Model

#### 5.1.1 Heat Exchanger Selection

For the purposes of preheating the hydrogen and generating steam from the waste heat of re-circulation of oxygen, the appropriate type of heat exchanger must be selected. Here, a plate heat exchanger has been selected. The reason is the high scalability in size and the simple construction make the plate heat exchanger apt for this application.

Therefore, this section covers the basic design methodology behind the Plate Heat Exchanger. The heat exchangers to be designed can be seen in Figure 5.1 and 5.2 from the thermodynamic cycle. The design of these heat exchangers has been considered as a series combination of plate heat exchangers for sensible and latent heat transfer. This can be seen as follows:

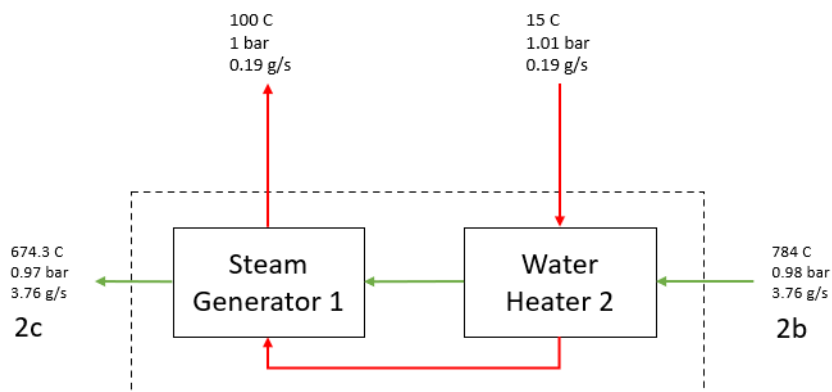


Figure 5.1: Evaporating unit 1 in the O<sub>2</sub> re-circulation loop

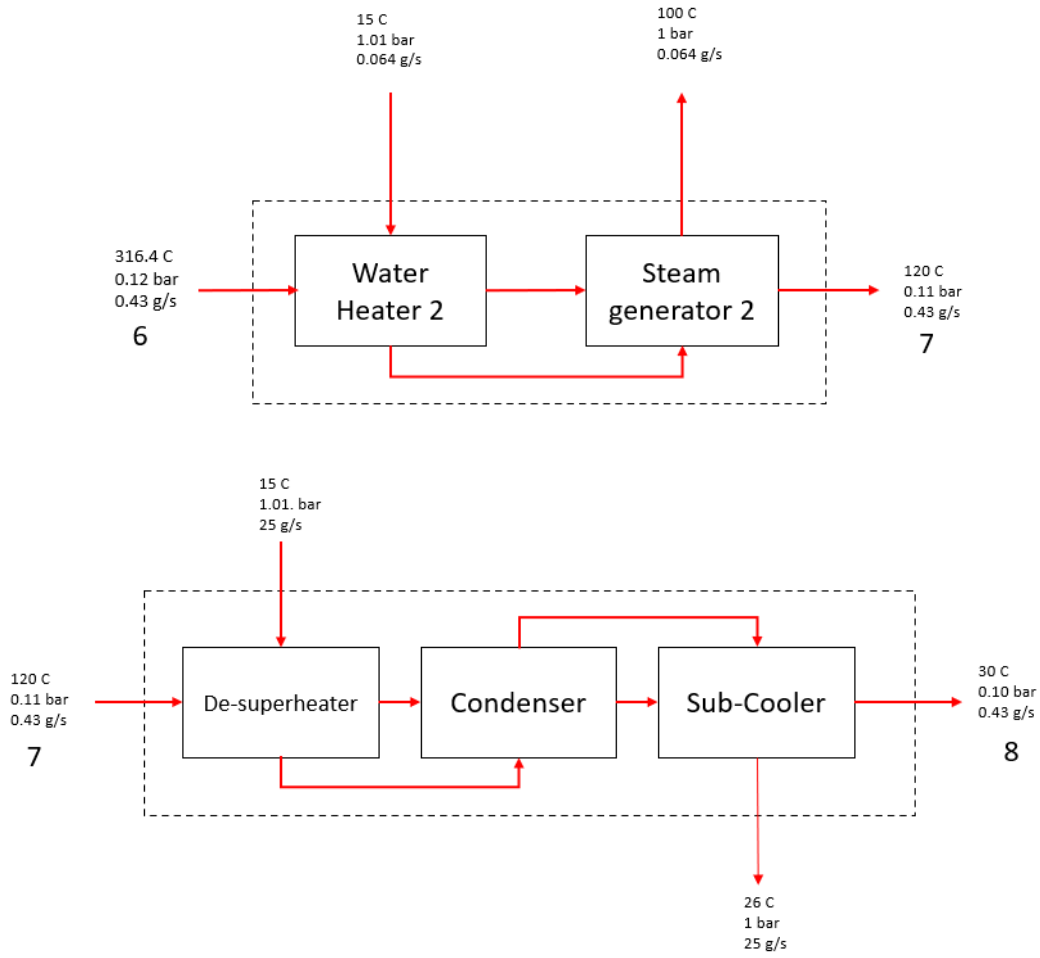


Figure 5.2: Evaporating Unit 2 downstream of the turbine (top) and condensing unit downstream of the turbine (bottom)

The basic design procedure is the same till the calculation of the total heat transfer area as given in Section 2.7.2. The steps specific to the design of the plate heat exchanger are as follows:

- Calculation of the number of plates and channels: Once the total heat transfer area ( $A$ ) has been obtained using Equation 2.38, the number of plates ( $N_{pl}$ ) can be calculated by using the area of one plate ( $a_p$ ). The number of channels ( $N_{ch}$ ) can then be calculated as

$$N_{pl} = \frac{A}{a_p} \quad (5.1)$$

$$N_{ch} = \frac{(N_{pl} - 1) + 2}{2} \quad (5.2)$$

The 2 plates added correspond to the 2 end plates.

- Calculation of the heat transfer coefficient:

The relations for the heat transfer coefficient calculation have been obtained from Sinnott and Towler [50]. The following equation are for sensible heat transfer in the range of  $Re > 2300$  and  $10 < Pr < 450$  respectively.

$$h = (0.26Re^{0.65}Pr^{0.4}) \frac{\lambda}{d_e} \quad (5.3)$$

$$h = (0.6Re^{0.51}Pr^{0.4}) \frac{\lambda}{d_e} \quad (5.4)$$

Whereas for latent heat transfer, the following equations as found in Garcia et al. [18] can be used, in the range of  $13 < Re < 230$  for the evaporator and in the range of  $50 < Re < 2000$  the condenser respectively.

$$h_{evap} = (2.7Re_l^{0.55}Pr^{0.5})\frac{\lambda_l}{d_e} \quad (5.5)$$

$$h_{cond} = (1564Re_{eq}^{-0.76}Pr_l^{0.33}0.347Re^{0.653})\frac{\lambda_l}{d_e} \quad (5.6)$$

- Calculation of Pressure drop in channels, conduits and ports: The pressure loss across the plate heat exchangers occurs in 3 places, namely; in the channels, through the conduits formed by the gaskets and through the ports upon entry and exit. The pressure loss in the conduits can be found by:

$$\Delta P_{conduit} = 8j_f \frac{L_p \rho u_p^2}{d_e} \quad (5.7)$$

$$j_f = 0.6Re^{-0.3} \quad (5.8)$$

The pressure loss in the ports can be found by:

$$\Delta P_{pt} = 1.3 \frac{\rho u_{pt}^2 N_{pl}}{2} \quad (5.9)$$

The pressure loss in the channels can be found from the following equations as in VDI Heat Atlas [51]:

$$\Delta P_{channel} = \frac{1}{2} \xi \rho u_p^2 \frac{L_p}{d_e} \quad (5.10)$$

$$\xi_0 = \frac{64}{Re} \quad (5.11)$$

$$\xi_1 = (1.8 \ln Re - 1.5)^{-2} \quad (5.12)$$

$$\left[\frac{1}{\xi}\right]^{0.5} = \frac{\cos \phi}{[0.18 \tan \phi + 0.36 \sin \phi + \frac{\xi_0}{\cos \phi}]^{0.5}} + \frac{1 - \cos \phi}{[3.8 \xi_1]^{0.5}} \quad (5.13)$$

where  $u_{pt}$  is the velocity of the fluid through the ports,  $u_p$  is the channel velocity,  $j_f$  is the pipe friction factor,  $L_p$  is the length of the plate,  $d_e$  is the hydraulic diameter and  $\xi$  is a factor which depends on the corrugation angle of the plate. The two relations given for  $\xi$  are applicable in Reynolds number ranges of less than 2000 and greater than 2000. The final relation for  $\xi$  relates it to the plate corrugation angle  $\phi$ .  $\phi$  has been taken as  $\frac{\pi}{4}$

The pressure loss in the evaporator can be found out by calculating the fanning fraction factor  $f$ , given by Yan and Lin as:

$$f_{evap} = 6.947 * 10^5 Re_{eq}^{-1.109} Re^{-0.5} \quad (5.14)$$

$$\Delta P_{channel} = 2f_{evap} \frac{G^2 L_{pl}}{\rho_{av} d_e} \quad (5.15)$$

where  $G_{eq}$  is the equivalent mass flux,  $\rho_{av}$  is the average density from the inlet and outlets.

$$G_{eq} = G \left[ (1-x) + x \left( \frac{\rho_l^{0.5}}{\rho_g^{0.5}} \right) \right] \quad (5.16)$$

where  $x$  is the quality of the fluid. The pressure loss in the condenser can be found by calculating the fanning friction factor using the correlation by Tao et al.[55] as:

$$f_{cond} = (4.207 - 2.673\phi^{0.46})(4200 - 5.41Bd^{1.2})Re_{eq}^{-0.95} \left( \frac{P_{sat}}{P_{cr}} \right)^{0.3} \quad (5.17)$$

where  $Bd$  is the bond number,  $P_{sat}$  is the saturation pressure at which condensation is happening, and  $P_{cr}$  is the critical pressure. The pressure drop in the channels can now be calculated using Equation 5.14.

Using the above thermodynamic state points shown in Figures 5.1 and 5.2, the design of the heat exchangers can be summarized as:



## 5.1.2 Results

The plate heat exchanger was designed using the inlet conditions given in Table 5.1 and the design procedure described above. The results are as follows:

Parameter	H <sub>2</sub> Pre-heater	Water Heater 1	Steam Generator 1
Duty	0.22 kW	0.061 kW	0.441 kW
LMTD	240 K	714.6 K	616.3 K
Port Diameter	30 mm	30 mm	30 mm
Area of single plate	50mm*20mm	27.3mm*13.6mm	59mm*29.5mm
Spacing	5mm	2.5mm	2mm
Number of Plates	14	3	5
Number of Channels per fluid	11	1	2
Overall heat Transfer Coefficient	50.2 W/mK	189.3W/mK	112.7W/mK
Pressure Drop	O <sub>2</sub> - 1.1 mbar, H <sub>2</sub> -8.5e-3 mbar	O <sub>2</sub> -4.2 mbar, H <sub>2</sub> O-1.36e-4 mbar	O <sub>2</sub> -0.5 mbar, H <sub>2</sub> O- 1.4 mbar

Table 5.1: Design specifications of the plate heat exchangers in the O<sub>2</sub> recirculation loop

Parameter	Water Heater 2	Steam generator 2	De-superheater	Condenser	Sub-Cooler
Duty	0.02 kW	0.145 kW	0.135 kW	1.03 kW	0.02 kW
LMTD	246.5 K	74.7 K	58.3 k	23	9.2 k
Port Diameter	30 mm	30 mm	30 mm	30 mm	30 mm
Area of single plate	20.4mm*10.2mm	143.3mm*71.6mm	98mm mm*49mm	98mm*49mm	98mm*49mm
Spacing	5mm	3mm	2 mm	1mm	2mm
Number of Plates	3	5	11	7	4
Number of Channels per fluid	1	3	6	6	3
Overall heat Transfer Coefficient	106.9 W/mK	32.1 W/mK	44.9 W/mK	1340 W/mk	329 W/mK
Pressure Drop	steam-13.1 mbar water-1.7e-4 mbar	steam-9.7 mbar water-2.5 mbar	steam-4.3 mbar water-0.65 mbar	steam-15.3 mbar water-7.3 mbar	water(condensate)-2.1e-2 mbar water-5.8 mbar

Table 5.2: Design specifications of the plate heat exchangers upstream of the turbine

Form the above results, the combined results for the heat exchangers can be tabulated as:

Parameter	H <sub>2</sub> Pre-heater	Evaporating Unit 1	Evaporating Unit 2	Condensing Unit
Duty	0.22 kW	0.502 kW	0.165 kW	1.185 kW
Total Area	1000 mm <sup>2</sup>	2111.7 mm <sup>2</sup>	17172 mm <sup>2</sup>	14406 mm <sup>2</sup>
Total Pressure Drop	O <sub>2</sub> -1.1 mbar H <sub>2</sub> -8.5e-3 mbar	O <sub>2</sub> -4.7 mbar H <sub>2</sub> O-1.4 mbar	steam-22.8 mbar H <sub>2</sub> O-2.5 mbar	steam-19.6 mbar H <sub>2</sub> O-13.75 mbar

Table 5.3: Combined area and pressure drop of the heat exchangers

## 5.2 Ejector

The ejector model used here is a 1-D model and is based of off the research pioneered by Keenan et al [28]. This model has been subsequently used by Sun et al.[52] and Maclay et al. [35]

The ejector is a constant pressure mixing type as explained in Section 2.6.

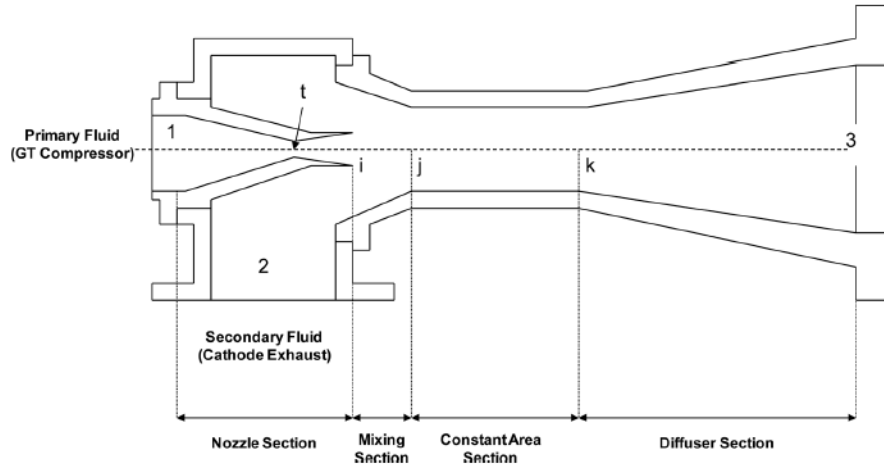


Figure 5.3: Constant Pressure Mixing type Ejector [35]

The primary fluid is accelerated through the primary nozzle and exits the primary nozzle at **i** at supersonic conditions. This causes a drop in the pressure and temperature. The temperature at the outlet of the primary nozzle at **i** is calculated using

$$T_{1a} = T_1 \left[ 1 + \frac{\eta_n (\gamma - 1) (M^2)_{1is}}{2} \right]^{-1} \quad (5.18)$$

$$p_i = p_1 \left( 1 + \frac{(\gamma - 1) M_{1is}^2}{2} \right)^{\frac{-\gamma}{\gamma - 1}} \quad (5.19)$$

where  $\eta_n$  is the nozzle efficiency, and  $P_i$  is the pressure at **i**,  $\gamma$  is the ratio of specific heats of oxygen and  $M_{1is}$  is the isentropic mach number at the outlet of the nozzle at **i**.

The actual mach number,  $M_{1ia}$  at the **i** is calculated using

$$M_{1ia} = \frac{2}{\gamma - 1} \left[ \frac{T_1}{T_{1ia}} - 1 \right]^{0.5} \quad (5.20)$$

The secondary fluid is enters the ejector at **2** as shown in Figure 5.3. The amount of secondary fluid entering defines the entrainment ratio  $\omega$  as follows:

$$\omega = \frac{m_{O_2 \text{ secondary}}}{m_{O_2 \text{ primary}}} \quad (5.21)$$

Using the entrainment ratio, the area ratio  $A_{ratio}$  can be found. It is defined as the ratio of the nozzle exit area to the secondary inlet area at **i**. This is given as:

$$A_{ratio} = \omega \frac{p_1}{p_2} \left[ \frac{\frac{p_1}{p_2} \frac{1}{\gamma} - \frac{p_i}{p_2} \frac{\gamma-1}{\gamma}}{\frac{p_1}{p_2} \frac{1}{\gamma} - \frac{p_i}{p_2} \frac{\gamma-1}{\gamma}} \right]^{0.5} \frac{T_2}{T_1} \quad (5.22)$$

where  $p_2$  is the pressure of the secondary fluid at **2**. The mixing takes place in the constant pressure section **i-j**. The mach number at the mixing junction is found using

$$M_j = \left[ \frac{2M_j^{*2}}{\gamma + 1 - 2M_j^{*2}(\gamma - 1)} \right]^{0.5} \quad (5.23)$$

where  $M_j^*$  is the sonic mach number at **j**. The full treatment of  $M_j^*$  can be found in [35]. Using the mach number at **j**, the mixing enthalpy can be calculated using the steady flow energy equation as follows

$$h_j = \frac{m_{O_2 \text{ primary}} h_{O_2 \text{ primary}} + \frac{m_{O_2 \text{ primary}} u_{O_2 \text{ primary}}^2}{2} + m_{O_2 \text{ secondary}} h_{O_2 \text{ secondary}} + \frac{m_{O_2 \text{ secondary}} u_{O_2 \text{ secondary}}^2}{2} - \frac{m_{O_2} u_j^2}{2}}{m_{O_2}} \quad (5.24)$$

The primary and secondary streams are completely mixed at **j** and the flow is sonic. Between **j** and **k**, the gas slows down to subsonic speeds, leading to the formation of transverse shocks. These shocks give rise to an increase in the static pressure and a decrease in the Mach number at **k**. This mach number is calculated from the following equation:

$$M_k = \left[ \frac{\frac{2}{\gamma-1} + M_j^2}{\frac{2}{\gamma-1} \gamma M_j^2 - 1} \right]^{0.5} \quad (5.25)$$

The corresponding increase in pressure and temperature at **k** are calculated using

$$p_k = p_j \frac{M_j \left( 1 + \frac{M_j(\gamma-1)}{2} \right)}{M_k \left( 1 + \frac{M_k(\gamma-1)}{2} \right)} \quad (5.26)$$

$$T_k = T_j \frac{1 + \frac{M_j(\gamma-1)}{2}}{1 + \frac{M_k(\gamma-1)}{2}} \quad (5.27)$$

At **k**, the flow is subsonic and a subsonic diffuser at the end provides an additional pressure rise. This pressure rise and the corresponding temperature rise at the exit of the ejector are given as

$$p_3 = p_k \left[ 1 + \frac{\eta_d(\gamma-1)(M_k^2)}{2} \right]^{\frac{\gamma}{\gamma-1}} \quad (5.28)$$

$$T_3 = T_k \left[ 1 + \frac{\eta_d(\gamma-1)(M_k^2)}{2} \right]^{\frac{\gamma}{\gamma-1}} \quad (5.29)$$

The ratio of the outlet pressure  $P_3$  and the secondary inlet pressure  $P_2$  is known as the compression ratio.

### 5.2.1 Results

The inlet parameters used for designing the ejector model, taken from the designed H<sub>2</sub>-O<sub>2</sub> thermodynamic cycle are as follows:

Parameters	Value	Unit
Primary Stream Pressure	6	bar
Secondary Stream Pressure	0.985	bar
Primary Stream Temperature	15	°C
Secondary Stream Temperature	674	°C
Entrainment Ratio	24.5	
Nozzle and Diffuser Efficiencies	0.98	%

Table 5.4: Inlet parameters used for designing the ejector

Another key inlet parameter, the isentropic inlet mach number  $M_{1is}$  of the primary stream at **i** needs to be determined. This is because the area ratio and consequently the geometry of the ejector, is a function of  $M_{1is}$ , as can be seen from Equation 5.22. Thus both the performance and the geometry need to be evaluated.

To do so, a sensitivity analysis is carried out by varying the inlet mach number from 1 to 3 while keeping the inlet pressure constant. Further, since the design is a supersonic ejector, the mach number at the the mixing junction  $M_j$  should be greater than or equal to 1. Therefore, in the analysis,  $M_j$  is observed closely and all the values of  $M_{is}$  leading to a value of  $M_j$  less than 1 are filtered out. First, a plot of the inlet mach number vs the suction pressure is made. The suction pressure is the difference between the secondary inlet pressure  $P_2$  and the pressure at the nozzle exit  $P_t$ . This is an important quantity to monitor since the suction pressure cannot be negative, because that would result in backflow. Therefore all mach numbers resulting in backflow are rejected. This can be seen in the following plot.

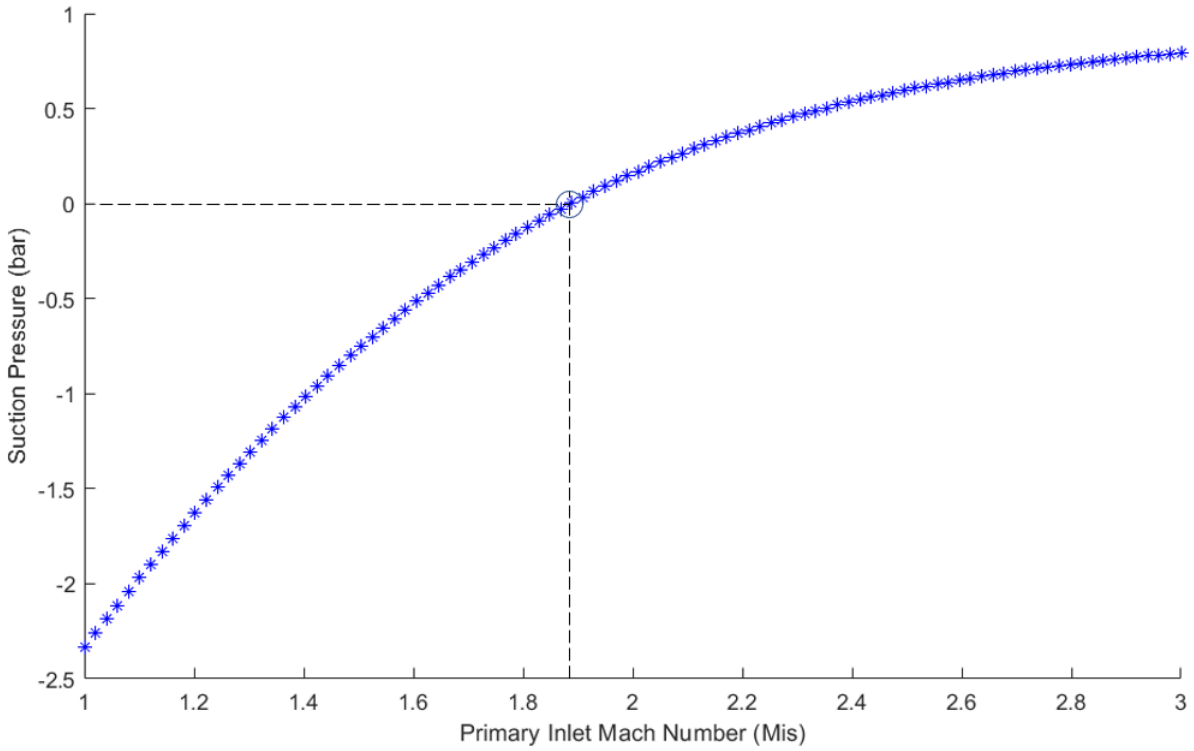


Figure 5.4: Inlet Isentropic Mach Number vs Suction Pressure

It can be observed that for a fixed inlet pressure of 6 bar, and a fixed entertainment ratio, mach number values less than 1.9 lead to backflow. Therefore, in the following plot the mach number is varied from 2 to 3 and the consequent changes in the outlet temperature ( $T_3$ ) and pressure ( $P_3$ ) are observed. This is given as follows:

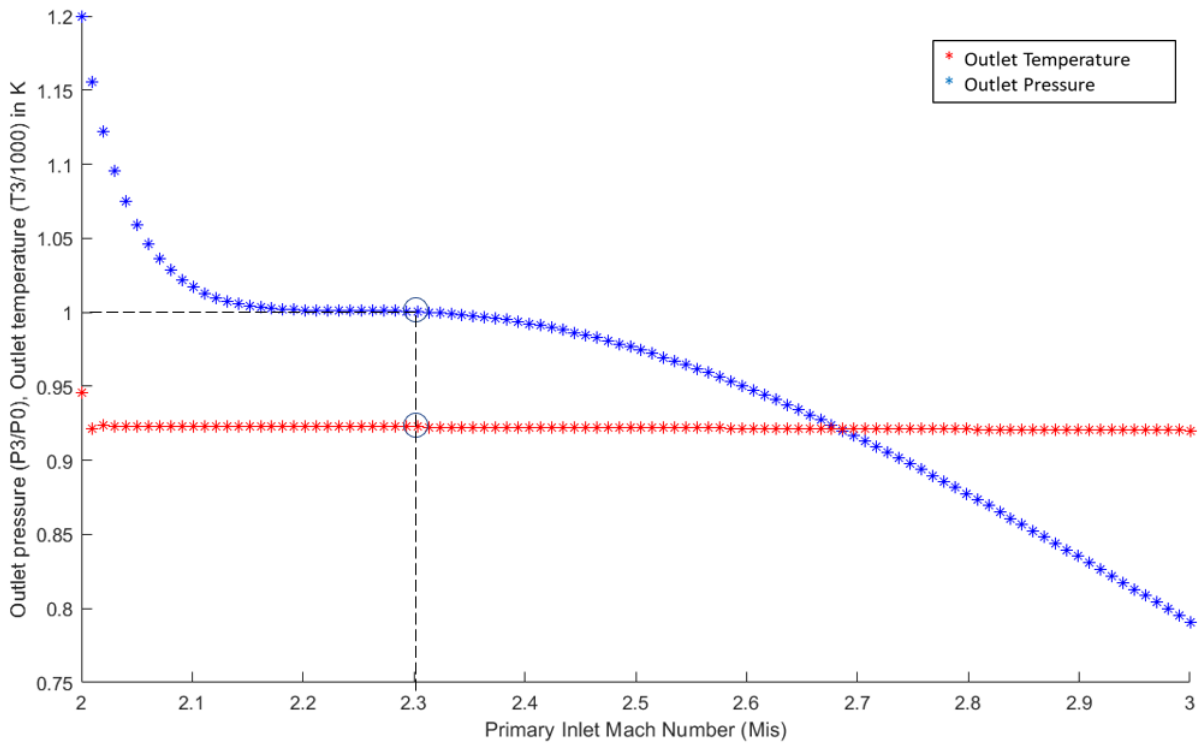


Figure 5.5: Isentropic Inlet mach number vs Outlet pressure and outlet temperature

From this curve, the maximum value of  $T_3$  (in the range of 923 to 928 K or 650 to 655 °C) having an

acceptable  $P_3$  value (atleast 1 bar) is chosen. This satisfies both the inlet pressure and temperature requirements of the SOFC. At the selected  $P_3$  and  $T_3$  values, the corresponding value of  $M_{is}$  is found. Using this value, the  $A_{ratio}$  can be calculated. Therefore, in this way, both the geometry can be calculated while ensuring the correct outlet parameters.

These results are tabulated as follows:

Parameters	Value	Unit
Outlet Pressure	1	bar
Outlet Temperature	650.1	°C
Area Ratio	122.1	
Inlet Mach number	2.3	
Compression Ratio	1.01	

Table 5.5: Ejector design results

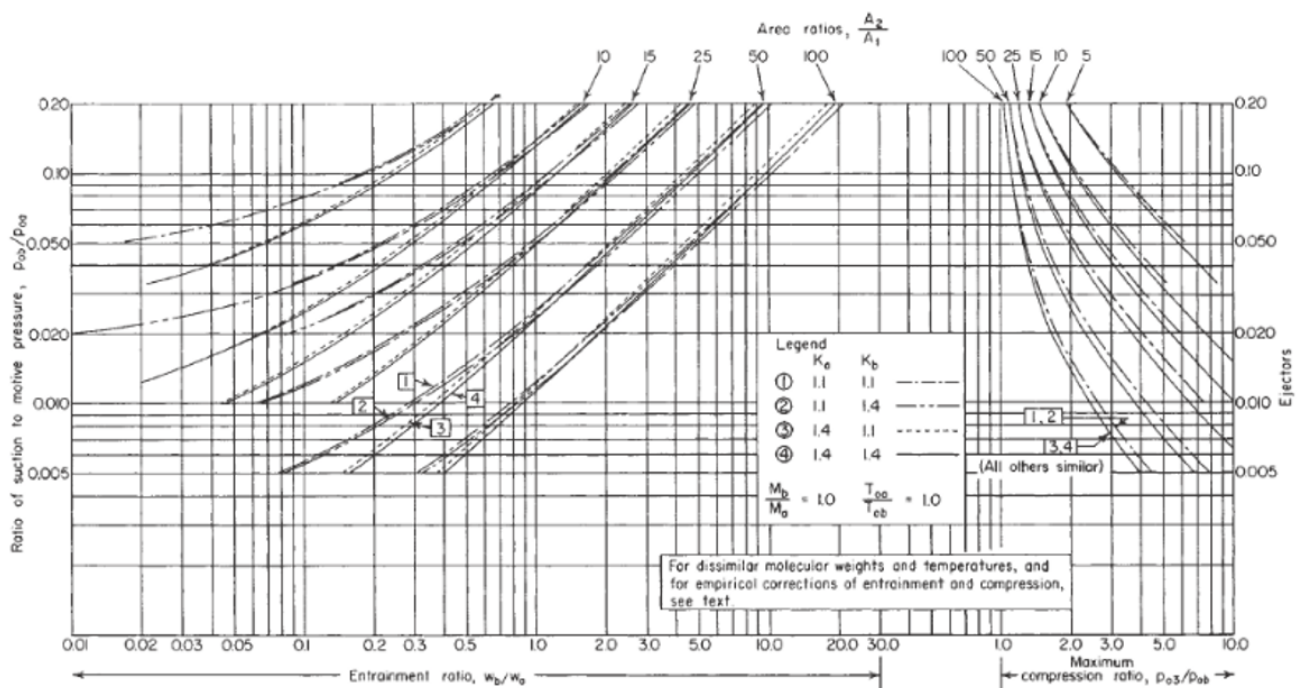


Figure 5.6: Design curves for an industrial Ejector curves[12]

The above plot by Hoerl et al[12], consists of design curves for industrial ejectors. The X axis consists of the entrainment ratio on the left side and the compression ratio on the right side. The Y axis consists of the ratio of the suction to the primary inlet pressure. The curves are plotted for various area ratios. It can be seen that the design curves predict a similar value of the area ratio for the same range of entrainment. They predict an entrainment of 20 for an area ratio of 100. Further, for these specifications, the ratio of outlet pressure to secondary inlet pressure is 1. Therefore, this is in line with the design provided above, with an area ratio of 122.1, for an entertainment of 24.5 and the compression ratio of 1.01. Therefore, this design is realistically achievable.

Based on the design curves, it can be seen that the ratio of suction pressure to motive pressure (inlet pressure) keeps increasing on the Y axis on the left as we follow a constant area ratio curve. At the same time, the entrainment keeps increasing and the compression ratio keeps decreasing on the left and right side of the X axis respectively. What this means is that as more and more fluid is entrained, it becomes harder and harder to compress the fluid to a higher pressure. Additionally, more fluid being entrained means that a higher pressure drop is needed. Therefore, with increased motive pressure at the inlet, for a fixed geometry the entrainment will approach a limit. In this case, the design conditions of 6 bar mean that the entrainment of the fluid will approach

a value of 24.5 as the inlet pressure is slowly increased to 6 bar and the outlet pressure will approach a value of 1 bar. At startup, a large suction pressure will be developed due to a low inlet pressure and atmospheric conditions at the outlet of the SOFC. Therefore, care should be taken that a vacuum like condition is not formed since the entrainment rate could be higher than 24.5 at 1 bar. Thus, the mass flow of the oxygen in the recirculation loop should be closely controlled using a flow control valve, so as to limit the entrainment ratio at lower inlet pressures. The inlet pressure should be then steadily increased to 6 bar to obtain the design conditions.

### 5.3 Turbine Sizing

To size the turbocharger, the Balje diagram can be consulted and the following procedure can be followed:

- Selection of type of turbine: From the H<sub>2</sub>-O<sub>2</sub> thermodynamic cycle presented in Figure 3.5, it can be seen that the mass flow of steam into the turbine is 0.43 g/s and the power produced is 0.404 kW. As previously stated, for such a small mass flow rate and power, only a radial turbine can be selected. Therefore a small radial turbine could be suitable for this application. The total expansion ratio is taken as 8. The typical pressure ratio of a single stage radial turbine is 4 (expansion ratio 0.25). Therefore, the turbine selected here would have 2 stages. Both stages are on the same shaft.
- Determination of the Specific speed and shaft speed: The optimum  $N_s$  range for radial turbines is from 0.1-1[17]. Therefore, for this range, the following relation of specific speed can be used to calculate the angular velocity ( $\Omega$ ). From  $\Omega$ , the actual shaft speed in RPM can be calculated.

$$N_s = \frac{m^{0.5} \Omega}{\rho_{av} \Delta h^{0.75}} \quad (5.30)$$

$$\Omega = \frac{2\pi N}{60} \quad (5.31)$$

- Determination of specific diameter: The specific diameter  $D_s$  can be found from the corresponding point on the Balje diagram connecting the  $N_s$  and the efficiency curve.
- Calculation of actual diameter: Once the value of the specific diameter has been calculated, the value of the actual impeller diameter can be found from the following equation [1]

$$D_s = \left[ \frac{d_t \Delta h^{0.25}}{\frac{m^{0.5}}{\rho_{av}^{0.5}}} \right] \quad (5.32)$$

- Calculation of pressure ratio per stage: The pressure ratio for each stage can be calculated as:

$$\frac{P_{1inlet}}{P_{1outlet}} = \frac{P_{2inlet}}{P_{2outlet}} \quad (5.33)$$

where  $P_{1inlet}$  is the pressure at the inlet of stage 1,  $P_{1outlet}$  is the pressure at the outlet of stage 1,  $P_{2inlet}$  is the pressure at the inlet of stage 2 and  $P_{2outlet}$  is the pressure at the outlet of stage 2. Since  $P_{1outlet} = P_{2inlet}$ , the pressure ratio per stage can be calculated.

#### 5.3.1 Results

The inlet parameters of the turbine are as follows:

Parameter	Value	Unit
Inlet Mass Flow	0.43	g/s
Number of Stages	2	
Expansion Ratio per Stage	0.33	

Table 5.6: Inlet values of turbine

Using the above inlet parameters, the  $N_s$ - $N$  plot was made in the range of 0.1 to 1 as given in [17]. Using this plot, the common shaft speed for both the stages were noted 5 different  $N_s$  values. This plot is shown as follows:

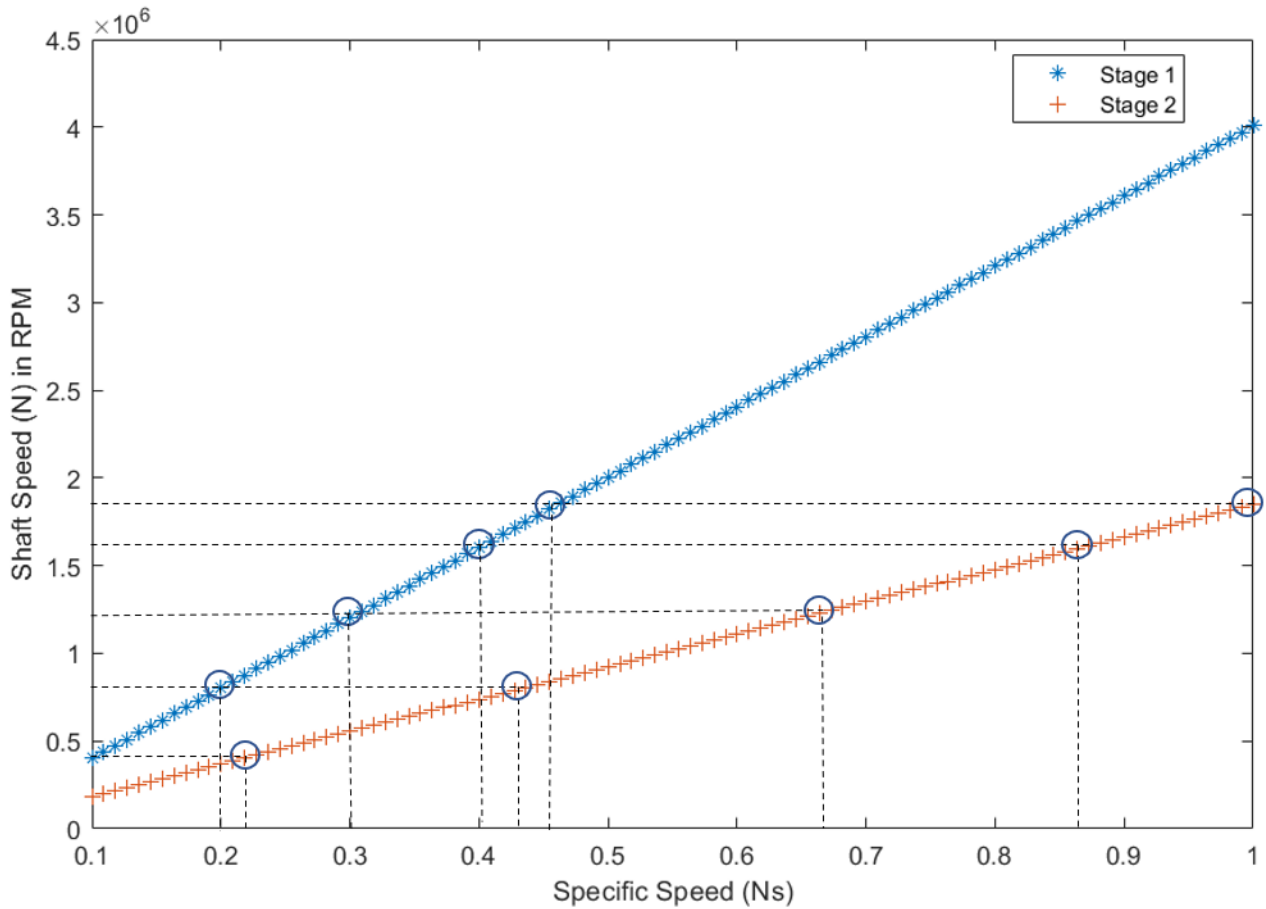


Figure 5.7: Specific Speed vs Shaft Speed plot made in the  $N_s$  range 0.1-1

From the above plot, it can be seen that there are multiple shaft speeds at which both stages could be possibly located. By plotting all the shaft speeds on the Balje daigram, the corresponding  $D_s$ , efficiency,  $d_t$ , shaft speed and Power have been tabulated as follows:

$N_{s1}$	$N_{s2}$	$D_{s1}$	$D_{s2}$	$d_{t1}$	$d_{t2}$	$\eta_1$	$\eta_2$	Total Power
0.1	0.25	10	7.5	19.3 mm	24 mm	0.7	0.8	0.331 kW
0.2	0.45	9	3.9	17.4 mm	12.5 mm	0.8	0.8	0.36 kW
0.3	0.65	7	3.5	13.5 mm	11.2 mm	0.8	0.8	0.376 kW
0.4	0.9	5	2.75	9.7 mm	8.8 mm	0.8	0.8	0.359 kW
0.45	1	3.75	2.25	7.2 mm	7.2 mm	0.9	0.7	0.371 kW

Table 5.7: Comparison of all possible shaft diameters and powers

The subscript 1 refers to stage 1 and 2 refers to stage 2. From Table 5.7, it can be seen that the turbine size with diameters 7.2 mm per stage are producing the most power. However, it is known that the smallest single stage turbocharger currently available is the VZ21 turbocharger from ECOTRONS. This turbocharger has a maximum inlet diameter of 25 mm. Therefore, upon comparison, the turbine size with  $d_{t1}$  19.3 mm and  $d_{t2}$  24 mm is the only design that seems realistic. Therefore, this size has been chosen going forward. The resulting dimensions of the selected turbine size are:

Parameter	Value	Unit
Specific Speed Stage 1	0.1	
Specific Speed Stage 2	0.25	
Specific Diameter Stage 1	10	
Specific Diameter Stage 2	7.5	
Shaft speed	4.07e5	RPM
Actual Diameter Stage 1	19.3	mm
Actual Diameter Stage 2	24	mm
Efficiency-stage 1	70	%
Efficiency-stage 2	80	%
Power Output	0.331	kW

Table 5.8: Results of Turbine Design

## 5.4 Material recommendations

This section contains material recommendations on the combustor and the heat exchangers. This is important as both these components require materials that have high temperature fatigue and creep resistance, that are readily available and economical.

### 5.4.1 Combustor

The combustor experiences the highest temperatures in a gas turbine Cycle. Therefore, to ensure desired performance at high temperatures, over the complete service life, the combustor has to be constructed out of materials that have the following properties[30]

- High melting point
- High temperature creep and fatigue strength
- Low coefficient of thermal expansion
- High weld-ability and form-ability, i.e. easy to fabricate
- Corrosion and Oxidation resistance

Traditionally, Nickel based super-alloys have been used extensively for manufacturing gas turbine combustors. Some of the most widely used ones are variants of Nimonic (Nimonic 75 and 263) , Hastelloy X and Cobalt based super-alloy HS 188 is also being used [30]. Between the three variants of Nimonic, 263 is a replacement of the older 75 and it is inferior than the 263 in term so high temperature creep strength [30]. The table shown below is a comparative representation of the properties of HS 188 and Hastelloy X mentioned above.

Material	Melting Range (C)	Creep	Thermal Conductivity	CTE	HCR
HS 188	1315 - 1410	1000 hr at 14 MPa	10.4-27.6	16.5e-6	20
X	1260-1355	1000 hr at 8.3 MPa	9.2-26.7	16.6e-6	41

Table 5.9: Comparative properties of HS188 and Hastelloy X

For the current application, a Turbine Inlet temperature of 960 °C is required. based on the simulations performed , it can be seen that the inner walls of the combustor are exposed to a temperature of 960 °C. Taking this as the initial point, it can be seen that the melting range of each material, is much higher than the TIT. Further, the high temperature creep limit, for both is much higher than the conditions of 0.095 MPa demand. Therefore, it can be safely assumed that the materials would not rupture even after 1000 hrs. However, the highest creep strength is shown by HS188. This is also why modern gas turbines are increasingly using HS188 as a replacement of Hastelloy X [30]. Even though any of the 2 materials can be safely used in this application,



HS188 shows the highest Hot corrosion resistance (HCR), lowest coefficient of thermal expansion(CTE) , and highest thermal conductivity. Therefore, out of the 2, HS188 is the optimum choice. it should also be noted that this brief comparison is not a full in-depth comparison of the 2 materials performance, but is a small comparison of the most important properties. Both materials can be welded using TIG and MIG.

### 5.4.2 Heat Exchangers

High temperature and compact welded plate heat Exchangers are available with Inconel 617 plates such as the Bosal P4 [4]. These heat exchangers have an operating range of 400-1100 °C, with an inlet mass flow range upto 10 g/s and are therefore suitable for being used in preheating the hydrogen and/or as the evaporating unit in the O<sub>2</sub> re-circulation loop.



Figure 5.8: Bosal P4 Plate Heat Exchanger [4]

# Chapter 6

## SYSTEM CONTROL

### 6.1 Updated Thermodynamic Cycle

The thermodynamic H<sub>2</sub>-O<sub>2</sub> cycle designed was based on the following assumptions:

Parameter	Value
Isentropic efficiency of turbine	90 %
Pressure drop across components	1 %

Table 6.1: Assumptions taken while designing the thermodynamic H<sub>2</sub>-O<sub>2</sub> cycle

In the previous chapter, from the results of the designed heat exchangers, ejector and the turbine, Thermodynamic H<sub>2</sub>-O<sub>2</sub> cycle can now be updated as presented in Figure 6.1

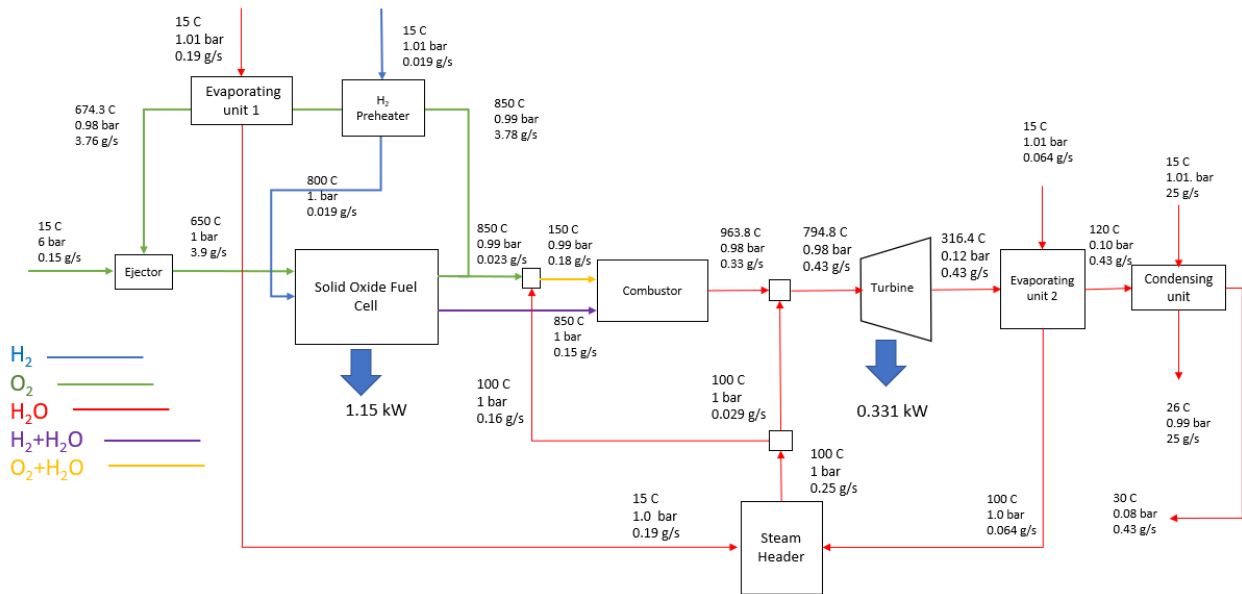


Figure 6.1: Updated Process Flow Diagram of the designed H<sub>2</sub>-O<sub>2</sub> thermodynamic cycle

It can be observed that due to the decrease in the value of the isentropic efficiency of the turbine, the efficiency of the cycle has decreased from 67.28 % to 64.09 %. The total power produced has also decreased from 1.56 to 1.48 kW.

The following table summarises these results.

Parameters	Value	Unit
SOFC Power Output	1.15	kW
Turbine Power Output	0.331	kW
Total power Output	1.48	kW
Thermal efficiency	64.09	%

Table 6.2: Results of the updated H<sub>2</sub>-O<sub>2</sub> thermodynamic cycle

## 6.2 System Control Scheme

Based on the updated H<sub>2</sub>-O<sub>2</sub> thermodynamic cycle presented in Figure 6.1, a simple way to control the system has to be devised. To do so, all the important points in the thermodynamic cycle requiring close control of pressure, temperature and mass flow have been identified. These points have been highlighted and the control parameters have been identified as given in the following figure.

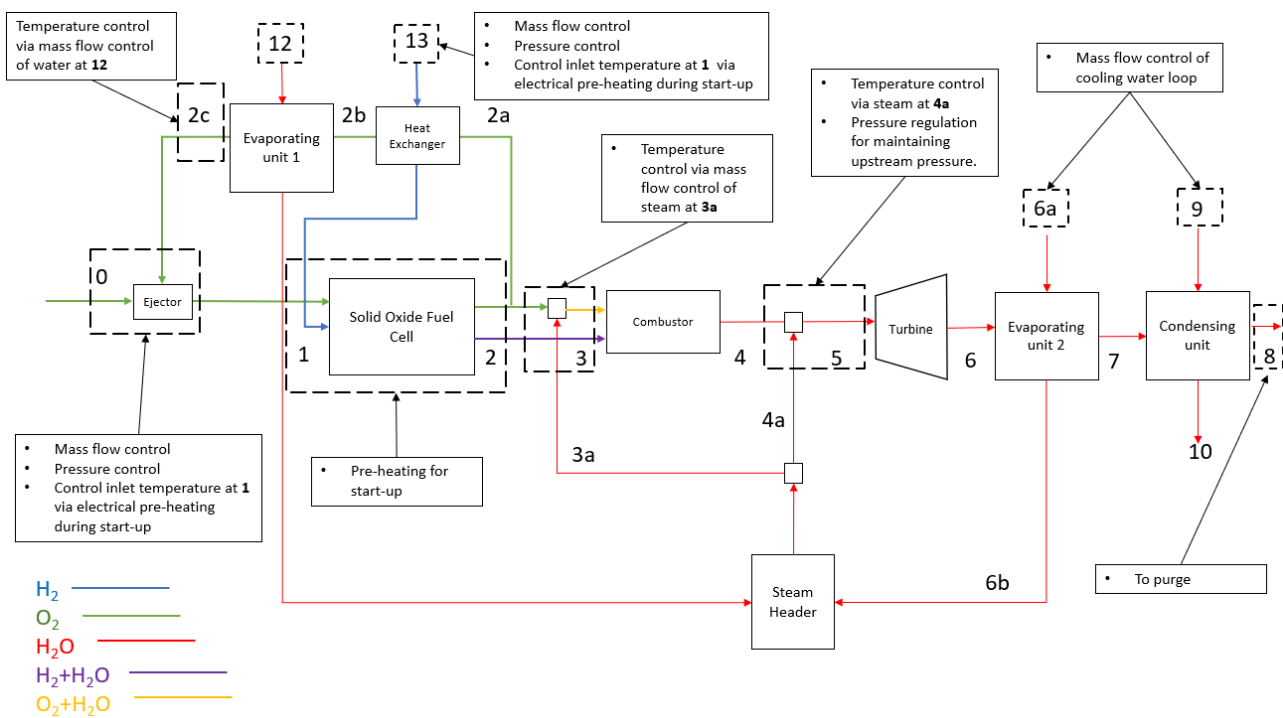


Figure 6.2: Highlighted areas of control in the Process Flow Diagram

Keeping the above points in mind, a simple control scheme has been generated as follows:

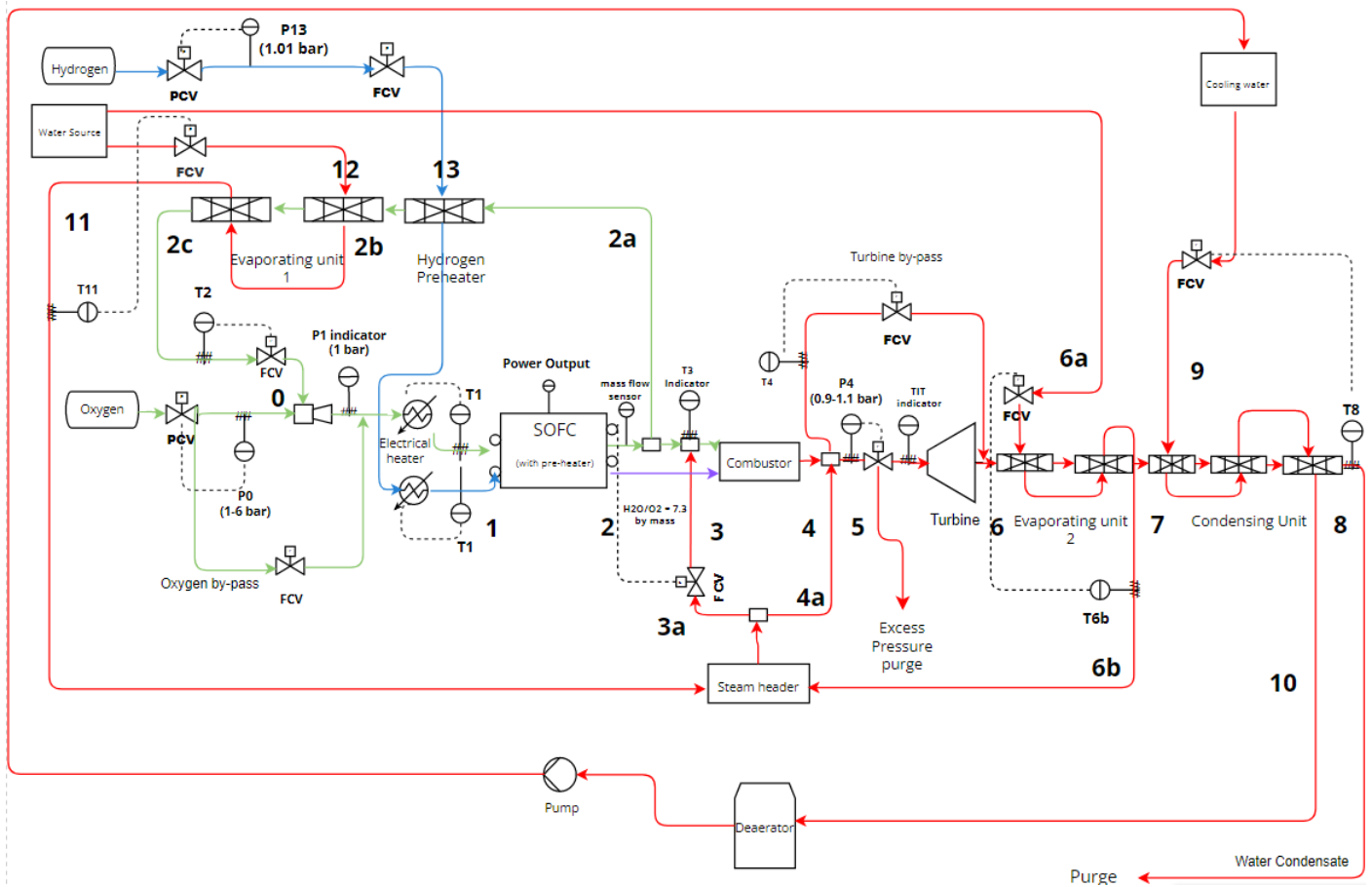


Figure 6.3: Basic instrumentation diagram of the H<sub>2</sub>-O<sub>2</sub> thermodynamic cycle

During system start-up, a pre-heater is used to heat the SOFC to around 800 °C. Once the SOFC reaches its equilibrium temperature, the mass flows of oxygen and hydrogen can be given at **0** and **13** respectively. The pressure control valves (marked as PCV in the diagram) at **0** and **13** can be used to regulate the inlet pressures. Once the desired pressures are achieved, the mass flow control valves (marked as FCV) can be used to control the inlet mass flow of oxygen and hydrogen to the SOFC at **1**. Electrical pre-heaters are provided at **1** to achieve the desired inlet temperatures for oxygen and hydrogen at 650 and 800 °C respectively. Since the re-circulation would not have started yet, to ensure that the mass flow of oxygen at the inlet of the SOFC is at design conditions, extra oxygen can be supplied using a bypass to the SOFC inlet when needed. The pressure of the inlet oxygen at **0** can be slowly increased from 1 to 6 bar in order to start the recirculation of oxygen. The amount of oxygen in the recirculation loop can be controlled by the FCV at **2c**. The temperature at **2c** is controlled by mass flow of water at **12**. Once the temperature at **2c** reaches the steady states temperature of 674 °C, and the outlet pressure of the ejector is 1 bar with an inlet pressure of 6, the by-pass valve can be fully closed. The mass flow sensor at **2** can be used to track the amount of oxygen leaving the SOFC.

Downstream of the SOFC, the mass flow sensor at **2** controls the amount of steam that combines with the outlet oxygen at **3** from the steam header. The rest of the steam enters the exit of the combustor at **4**. A back pressure regulator **P4** at **4** is used to maintain the upstream pressure of the system at an atmospheric pressure for the safe operation of the SOFC. Any excess pressure is purged. A temperature sensor **T4** controls a turbine by-pass valve. The by-pass valve is open till the correct TIT is not reached at **5**. Once it is reached, the valve opens and the steam enters the turbine.

Downstream of the turbine, the mass flow of water to the evaporating unit is controlled by the temperature sensor at **6b**, which tells the temperature of the steam produced by the evaporators. The cooling water in the condensing unit is controlled by the FCV at **9** via the temperature sensor at **8**, which senses the temperature of the water exiting the condensing unit. The water condensate is purged, and the cooling water is sent to a deaerator to then be pumped back.

## Chapter 7

# CONCLUSIONS AND RECOMMENDATIONS

### 7.1 Conclusions

The prime objective of this research was to develop the overall basic design of a small scale H<sub>2</sub>-O<sub>2</sub> test set up, consisting of a Solid Oxide Fuel Cell and a gas turbine. Throughout this report, a systematic approach to designing the test set up was employed. First, the basic thermodynamic cycle was designed. This cycle consists of an SOFC running on pure hydrogen and oxygen, followed by a combustor and a turbine. The SOFC model is based on 3YSZ Kera Cell II by KERAFOIL. The power produced by the SOFC is 1.15 kW at a fuel and oxygen utilisation of 85 % and an efficiency of 58.6 % for the LHV of consumed hydrogen. The oxygen stream is split by sending stoichiometric amount of oxygen to the combustor, where through non-premixed combustion, the leftover hydrogen (15%) is burnt with pure oxygen. To cool the SOFC, recirculative cooling is employed using the remaining oxygen via an ejector. The waste heat extracted from the oxygen is utilised to generate steam at 100 °C and 1 bar, and to preheat the inlet hydrogen to 800 °C. This steam is used to control the inlet temperatures of the combustor and the turbine. The steam exiting the turbine is further used to generate more steam at 100 °C and 1 bar. The saturated steam is sent to the inlet of the turbine increasing its power output. The exhaust steam is condensed and the cooling water is pumped and stored. The total power produced by the system is 1.48 kW and thermal efficiency is 64.09 %.

Following the design of the H<sub>2</sub>-O<sub>2</sub> thermodynamic cycle, the design of the major components of the system was done. First, a micromix type combustor was chosen as a reference design. Two geometrical configurations were designed, one with the jet injection holes near the walls (configuration 1) of the combustor and the other with centrally mounted ones (configuration 2). Both geometries were designed and scaled by using the theory of jets in crossflow, a canonical flow type. The jet momenta of both the streams were optimised to ensure complete penetration and mixing. The geometries were designed using CAD, and a CFD analysis was performed using the  $k - \epsilon$  turbulence model and the equilibrium chemistry model. The results showed the formation of a short flame, with an adiabatic flame temperature of 960 °C. The mixture fraction had a constant value of 0.45 along the mixing planes of both geometries, indicating that both the hydrogen and oxygen streams were mixing perfectly. However for configuration 2, this mixture fraction value is obtained at a shorter distance from the inlet, indicating superior mixing. Furthermore, it was noted that the position of the injection holes adjacent to the combustor wall in configuration 1 lead to the formation of the flame too close to the wall. Further, an overall pressure drop of 2 kPa (20 mbar) was observed for configuration 1 vs 1.3 kPa (13 mbar) for configuration 2. This was due to higher inlet velocities in configuration 1 due to smaller injection holes. Overall, configuration 2 was chosen due to the centrally mounted flames, superior mixing and lower overall pressure drop.

After the design of the combustor, the additional components such as the heat exchangers, ejector and the turbine were designed. The heat exchangers were designed as simple plate type exchangers for preheating the hydrogen, generating saturated steam and condensing the exhaust steam to saturated liquid.

Following this, the basic ejector geometry and operating conditions were determined by performing a sensitivity analysis between the inlet mach number, suction pressure, outlet pressure and outlet temperature. At an inlet

pressure of 6 bar, an entrainment ratio of 24.54 and an area ratio of 124.1 were determined. These value were validated against the design diagrams for industrial ejectors.

To size the turbine, a 2 stage radial turbine with a pressure ratio of 8 was selected, with both stages on the same shaft. The turbine was sized using the Balje diagram and the shaft speed was found to be 4.07e6 and the root to tip diameter of the 2 stages was found to be 19.3 mm and 24 mm respectively. The isentropic efficiency was found to be 70% for stage 1 and 80% for stage 2 and the power generated was 0.331 kW.

Finally, the HS 188 nickel based super alloy were recommended for the combustor and Inconel 617 for the heat exchangers. These were recommended based on their high melting range, high creep strength, high corrosion resistance and low coefficient of thermal expansion.

Once the final system was designed, a basic control scheme was developed to show how the system can be controlled during start-up.

## **7.2 Recommendations**

The scope of this research was to develop a a basic, overall design of the H<sub>2</sub>-O<sub>2</sub> thermodynamic cycle and its major components. This research is in no way an in-depth treatment of the development of the individual components. That being said, based on the current research, further improvements can be made in order to develop more detailed designs of the system and/or its components.

The steady state system has been designed and explored here. Therefore, only the design point have been considered. No dynamic behaviour of the thermodynamic cycle or of its components has been captured. Only a basic control scheme has been developed. Therefore, to study the transient behaviour of the system during start-up and shutdown, a dynamic thermodynamic cycle can be designed along with, dynamic modelling of each of the components to capture their transient behavior. This would give better insights into the off-design performance and control of the cycle.

The basic design of the geometry of the ejector has been provided. The geometry derived is based on experimental trends as there exists no universal method of determining the complete geometry of an ejector for each specific application. The only way this can be done is by performing a thorough CFD analysis. Therefore, to improve the ejector geometry provided here, a CFD analysis can be performed. Furthermore, if a higher pressure rise is required, a two-stage ejector can be considered.

The combustor design can be analysed in greater detail by assuming non-adiabatic, transient combustion alongside the use of relatively more accurate but computationally heavy methods such as Large Eddy Simulation instead of RANS. Furthermore, water injection in the form of aerosol, as opposed to steam injection for cooling the combustor can be explored. This will have the added advantage of simplifying the cycle as there will be no need for additional steam generators.

# Bibliography

- [1] OE Balje. “A study on design criteria and matching of turbomachines: Part a—similarity relations and design criteria of turbines”. In: (1962).
- [2] Lindert van Biert. “Solid oxide fuel cells for ships: System integration concepts with reforming and thermal cycles”. PhD thesis. Delft University of Technology, 2020.
- [3] Dieter Bohn. “Micro gas turbine and fuel cell-A hybrid energy conversion system with high potential”. In: *Micro Gas Turbines* 13 (2005), pp. 1–46.
- [4] BOSAL. *BOSAL energy*. 2022. URL: <https://www.bosal.com/en/energy>.
- [5] Roberto Bove and Stefano Ubertini. *Modeling solid oxide fuel cells: methods, procedures and techniques*. Springer Science & Business Media, 2008.
- [6] Nigel Brandon et al. *Solid oxide fuel cells: from materials to system modeling*. Royal society of chemistry, 2013. DOI: <https://doi.org/10.1098/rsta.2016.0400>.
- [7] NP Brandon and Zeynep Kurban. “Clean energy and the hydrogen economy”. In: *Philosophical Transactions of the Royal Society A: Mathematical, Physical and Engineering Sciences* 375.2098 (2017), p. 20160400.
- [8] Jinwei Chen et al. “Performance Evaluation of an SOFC-GT Hybrid System With Ejectors for the Anode and Cathode Recirculations”. In: *Journal of Electrochemical Energy Conversion and Storage* 16.4 (2019), p. 041004. DOI: 10.1115/1.4042985.
- [9] Kilian Claramunt Altimira. “Numerical simulation of non-premixed laminar and turbulent flames by means of flamelet modelling approaches”. In: (2005).
- [10] G Dahl and R Elsing. “Modification of the fuel system of a turboshaft engine from kerosene to hydrogen”. In: *9th World Hydrogen Energy Conference Proceedings*. 1992.
- [11] Günter Dahl and F Suttrop. “Engine control and low-NO<sub>x</sub> combustion for hydrogen fuelled aircraft gas turbines”. In: *International Journal of Hydrogen Energy* 23.8 (1998), pp. 695–704.
- [12] LA Defrate and AE Hoerl. “Optimum design of ejector using digital computers”. In: *Chem. Eng. Prog. Symp. Ser.* Vol. 55. 21. 1959, p. 12.
- [13] Tom Evertse. “The design of an innovative hydrogen-oxygen power system based upon a solid oxide fuel cell and an advanced thermodynamic cycle”. In: (2021). URL: <http://resolver.tudelft.nl/uuid:3425b00e-931f-4593-b10d-2aa211098b15>.
- [14] Samer Fawzy et al. “Strategies for mitigation of climate change: a review”. In: *Environmental Chemistry Letters* 18.6 (2020), pp. 2069–2094. DOI: <https://doi.org/10.1007/s10311-020-01059-w>.
- [15] Masafumi Fukuda and Yoshikazu Dozono. “Double reheat Rankine cycle for hydrogen-combustion, turbine power plants”. In: *Journal of Propulsion and Power* 16.4 (2000), pp. 562–567.
- [16] HH-W Funke et al. “Development and testing of a low NO<sub>x</sub> micromix combustion chamber for industrial gas turbines”. In: *International Journal of Gas Turbine, Propulsion and Power Systems* 9.1 (2017), pp. 27–36.
- [17] Marco Gambini and Michela Vellini. *Turbomachinery: Fundamentals, Selection and Preliminary Design*. Springer Nature, 2020.
- [18] JR Garcia-Cascales et al. “Assessment of boiling and condensation heat transfer correlations in the modelling of plate heat exchangers”. In: *International Journal of Refrigeration* 30.6 (2007), pp. 1029–1041.

- [19] Omer Genc, Serkan Toros, and Bora Timurkutluk. “Determination of optimum ejector operating pressures for anodic recirculation in SOFC systems”. In: *International Journal of Hydrogen Energy* 42.31 (2017), pp. 20249–20259.
- [20] Irvin Glassman, Richard A Yetter, and Nick G Glumac. *Combustion*. Academic press, 2014.
- [21] Md Azazul Haque et al. “Review of fuel/oxidizer-flexible combustion in gas turbines”. In: *Energy & Fuels* 34.9 (2020), pp. 10459–10485. DOI: 10.1021/acs.energyfuels.0c02097.
- [22] Klaus Hassmann. “SOFC power plants, the Siemens-Westinghouse approach”. In: *Fuel Cells* 1.1 (2001), pp. 78–84.
- [23] James D Holdeman. “Mixing of multiple jets with a confined subsonic crossflow”. In: *Progress in Energy and Combustion Science* 19.1 (1993), pp. 31–70.
- [24] James D Holdeman et al. “Mixing of multiple jets with a confined subsonic crossflow: part I—cylindrical duct”. In: (1997).
- [25] Bin-Juine Huang, CB Jiang, and FL Hu. “Ejector performance characteristics and design analysis of jet refrigeration system”. In: (1985).
- [26] HERBERT Jericha and M Fesharaki. “The Graz Cycle—1500° C Max Temperature Potential H<sub>2</sub>-O<sub>2</sub> Fired CO<sub>2</sub> Capture With CH<sub>4</sub>-O<sub>2</sub> Firing”. In: *Power* 10433.11502 (1995), p. 2495.
- [27] P Kazempoor and RJ Braun. “Model validation and performance analysis of regenerative solid oxide cells for energy storage applications: Reversible operation”. In: *international journal of hydrogen energy* 39.11 (2014), pp. 5955–5971.
- [28] Joseph Henry Keenan, Ernest Paul Neumann, and Ferdinand Lustwerk. “An investigation of ejector design by analysis and experiment”. In: (1950).
- [29] James Larminie and Andrew Dicks. *Fuel cell systems explained*. Vol. 2. 2003.
- [30] Arthur H Lefebvre and Dilip R Ballal. *Gas turbine combustion: alternative fuels and emissions*. CRC press, 2010.
- [31] Marcin Lemański and Janusz Badur. “Parametrical analysis of a tubular pressurized SOFC”. In: *Arch. Thermodyn* 25.1 (2004), pp. 53–72.
- [32] D Liscinsky, B True, and J Holdeman. “Experimental investigation of crossflow jet mixing in a rectangular duct”. In: *29th Joint Propulsion Conference and Exhibit*. 1993, p. 2037.
- [33] D Liscinsky, B Tue, and J Holdeman. “Effects of inlet flow conditions on crossflow jet mixing”. In: *32nd Joint Propulsion Conference and Exhibit*. 1996, p. 2881.
- [34] Hong Liu, Zhuoxiong Zeng, and Kaifang Guo. “Numerical investigation of the hydrogen swirl combustion flow in a micro gas turbine burner”. In: *Proceedings of the Institution of Mechanical Engineers, Part A: Journal of Power and Energy* (2022), p. 09576509221099386.
- [35] James D Maclay, Jacob Brouwer, and G Scott Samuelsen. “Development of a dynamic cathode ejector model for solid oxide fuel cell-gas turbine hybrid systems”. In: *Journal of Fuel Cell Science and Technology* 8.5 (2011).
- [36] Gaetano Maggio, Agatino Nicita, and Gaetano Squadrito. “How the hydrogen production from RES could change energy and fuel markets: A review of recent literature”. In: *International journal of hydrogen energy* 44.23 (2019), pp. 11371–11384.
- [37] United Nations. “Paris Agreement”. In: (2015).
- [38] Bart Numan. “Dynamic modelling and control of a solid oxide reversible cell for power disturbance rejection in a mixed power grid”. In: (2020).
- [39] OECD. *OECD Environmental Outlook to 2050*. 2012, p. 350. DOI: <https://doi.org/https://doi.org/10.1787/9789264122246-en>. URL: <https://www.oecd-ilibrary.org/content/publication/9789264122246-en>.
- [40] Rajendra K Pachauri et al. *Climate change 2014: synthesis report. Contribution of Working Groups I, II and III to the fifth assessment report of the Intergovernmental Panel on Climate Change*. Ippc, 2014.



- [41] E R Ray. “Westinghouse tubular SOFC technology”. In: (Dec. 1992). URL: <https://www.osti.gov/biblio/10107095>.
- [42] Jeroen Reurings. “A modeling study to investigate performance of SOFC-ICE hybrid systems for marine applications”. In: (2019).
- [43] Mirko Salewski, Dragan Stankovic, and Laszlo Fuchs. “Mixing in circular and non-circular jets in crossflow”. In: *Flow, Turbulence and Combustion* 80.2 (2008), pp. 255–283.
- [44] Wolfgang Sanz et al. “Adapting the zero-emission Graz Cycle for hydrogen combustion and investigation of its part load behavior”. In: *International Journal of Hydrogen Energy* 43.11 (2018), pp. 5737–5746.
- [45] Bram Schouten. “Thermal efficiency improvement of closed hydrogen and oxygen fuelled combined cycle power plants with the application of solid oxide fuel cells using an exergy analysis method”. In: (2020). URL: <http://resolver.tudelft.nl/uuid:e0d209d5-1cba-4e4b-b2d8-4925b71502a5>.
- [46] EG & G Services, Ralph M. Parsons Company, and Science Applications International Corporation. *Fuel Cell Handbook (Seventh Edition)*. DIANE Publishing, 2004.
- [47] Omar Z Sharaf and Mehmet F Orhan. “An overview of fuel cell technology: Fundamentals and applications”. In: *Renewable and sustainable energy reviews* 32 (2014), pp. 810–853. DOI: <http://dx.doi.org/10.1016/j.rser.2014.01.012>.
- [48] T-H Shih et al. *A new k-epsilon eddy viscosity model for high Reynolds number turbulent flows: Model development and validation*. Tech. rep. 1994.
- [49] C Howard Shomate. “A method for evaluating and correlating thermodynamic data”. In: *The Journal of Physical Chemistry* 58.4 (1954), pp. 368–372.
- [50] Ray Sinnott and Gavin Towler. *Chemical engineering design: SI Edition*. Butterworth-Heinemann, 2019.
- [51] Peter Stephan and VDI Heat Atlas. “B1 Fundamentals of Heat Transfer”. In: *VDI Heat Atlas* (2010), pp. 15–30.
- [52] Da-Wen Sun, Ian W Eames, and Satha Aphornratana. “Evaluation of a novel combined ejector-absorption refrigeration cycle—I: computer simulation”. In: *International Journal of Refrigeration* 19.3 (1996), pp. 172–180.
- [53] Sunfire. *Sunfire*. 2022. URL: <https://www.sunfire.de>.
- [54] Tom Tanneberger. “Investigation of zero-emission hydrogen oxyfuel flames”. In: (2020).
- [55] Xuan Tao and Carlos A Infante Ferreira. “Heat transfer and frictional pressure drop during condensation in plate heat exchangers: Assessment of correlations and a new method”. In: *International Journal of Heat and Mass Transfer* 135 (2019), pp. 996–1012.
- [56] Bourhan M Tashtoush, Al-Nimr Moh’d A, and Mohammad A Khasawneh. “A comprehensive review of ejector design, performance, and applications”. In: *Applied Energy* 240 (2019), pp. 138–172.
- [57] David Ting. *Basics of engineering turbulence*. Academic Press, 2016.
- [58] ZERO-CARBON GAS TURBINE. “HYDROGEN GAS TURBINES”. In: ().
- [59] Graham Walker. *Industrial heat exchangers: a basic guide*. Hemisphere Publishing Corporation, 1982.
- [60] Jurgen Warnatz et al. *Combustion*. Springer, 2006.
- [61] *The Potential of GT Combined Cycles for Ultra High Efficiency*. Vol. Volume 3: Cycle Innovations; Education; Electric Power; Fans and Blowers; Industrial and Cogeneration. Turbo Expo: Power for Land, Sea, and Air. June 2012, pp. 133–142. DOI: 10.1115/GT2012-68586. eprint: [https://asmedigitalcollection.asme.org/GT/proceedings-pdf/GT2012/44694/133/4219699/133\\_1.pdf](https://asmedigitalcollection.asme.org/GT/proceedings-pdf/GT2012/44694/133/4219699/133_1.pdf). URL: <https://doi.org/10.1115/GT2012-68586>.
- [62] Caroline Willich et al. “Pressurized Solid Oxide Fuel Cells: Operational Behavior”. In: (2011).
- [63] Farshid Zabihian and Alan S Fung. “Macro-level modeling of solid oxide fuel cells, approaches, and assumptions revisited”. In: *Journal of Renewable and Sustainable Energy* 9.5 (2017), p. 054301.

- [64] Li Zhou et al. “Performance of an anode-supported tubular solid oxide fuel cell (SOFC) under pressurized conditions”. In: *Electrochimica Acta* 53.16 (2008), pp. 5195–5198. DOI: 10 . 1016 / j . electacta . 2008 . 02 . 032.

# Appendix A

## A.1 Finite Chemistry Model

To tackle the issues the finite chemistry model, the finite chemistry model takes into consideration the RANS species concentration equation apart from the RANS momentum and the RANS mixture fraction equations. The species conservation equation is given as follows:

$$\frac{\partial \rho w_i}{\partial t} + \nabla(\rho v w_i) - \nabla(\rho D \nabla w_i) = M_i \omega_i \quad (\text{A.1})$$

where  $M_i$  = mass of generated species  $\omega_i$  = chemical reaction rate =  $-k_r[a][b]$   $-k_r$  = reaction coefficient  $[a][b]$  = concentration of reactants a and b

Together  $M_i \omega_i$  is the source of generation of species.

The RANS Species conservation equation is given as:

$$\frac{\partial \bar{\rho} \tilde{w}_i}{\partial t} + \nabla \cdot (\bar{\rho} \tilde{v} \tilde{w}_i) + \nabla \cdot (\overline{-\rho D \nabla w_i} + \overline{\rho v'' w_i''}) = \overline{M_i \omega_i} \quad (\text{A.2})$$

Now, it can be seen that the source term has been averaged as  $\overline{M_i \omega_i}$ . This term is equal to  $\overline{-k_r[a][b]}$ . But this is not equal to  $-\overline{k_r} \cdot \overline{[a]} \cdot \overline{[b]}$ . Therefore, the terms cannot be simply replaced by their average. To solve this issue, the PDF method can be applied again. First the following assumptions are taken: The turbulent flame is approximated as an ensemble of laminar flamelets each with a scalar dissipation rate  $\chi$  with their distribution arising as a consequence of the temporal and spatial fluctuations. In this way, the weight fraction of the species ( $w_i$ ), can be linked to the mixture fraction as follows:

$$w_i = w_i^f(\xi) \quad \nabla w_i = \frac{\partial w_i^f}{\partial \xi} \nabla \xi \quad (\text{A.3})$$

This relation is between the mixture fraction and the weight fraction of the species ( $w_i = w_i^f(\xi)$ ) is a unique one for each species in a reaction. It can be attained by simulating Non-Premixed laminar flames or from experimental data. Substituting back in the species conservation equation, the flamelet equation is obtained as follows:

$$-\rho D \nabla^2 \xi \frac{\partial^2 w_i^f}{\partial \xi^2} = M_i \omega_i \quad (\text{A.4})$$

Now, the average of the source term can be calculated from the PDF as follows:

$$\overline{M_i \omega_i} = -\frac{1}{2\bar{\rho}} \int_0^1 \int_0^\infty \chi \frac{\partial^2 w_i^f}{\partial \xi^2} \tilde{P}(\chi, \xi) d\chi d\xi \quad (\text{A.5})$$

Therefore, the average amount of species generated based on the rate of reactions ( $\overline{M_i \omega_i}$ ), can be calculated via this PDF approach. To solve this equation, the PDF must be known beforehand. The calculation of the PDF can be simplified by assuming that  $\xi$  and  $\chi$  are statistically independent and thus,  $\tilde{P}(\xi, \chi) = \tilde{P}(\xi) \cdot \tilde{P}(\chi)$ . Usually a log-normal distribution is chosen for  $\tilde{P}(\chi)$  and a  $\beta$  function is chosen for  $\tilde{P}(\xi)$  [60]. The PDF in this case is a

function of both  $\chi$  and  $\xi$ . The scalars are given in a similar way as above:

$$\tilde{T} = \int_0^1 (T(\xi, \chi)) \tilde{P}(\xi, \chi) d\xi d\chi \quad (\text{A.6})$$

$$\tilde{\rho} = \int_0^1 (\rho(\xi, \chi)) \tilde{P}(\xi, \chi) d\xi d\chi \quad (\text{A.7})$$

$$\tilde{T}''^2 = \int_0^1 (T(\xi, \chi) - \tilde{T})^2 \tilde{P}(\xi, \chi) d\xi d\chi \quad (\text{A.8})$$

$$\tilde{\rho}''^2 = \int_0^1 (\rho(\xi, \chi) - \tilde{\rho})^2 \tilde{P}(\xi, \chi) d\xi d\chi \quad (\text{A.9})$$

## A.2 SOFC Validation

The 0-D model has been validated against the Siemens Westinghouse SOFC data as given in [46]. The Fuel utilisation is set to 85 % . The fuel composition is 89 % hydrogen and 11 % steam. The oxidiser is air taken at 6 times the stoichiometric requirement in line with the experimental data from [46]. The following common inputs are taken:

Parameter	Value
Mass flow of Fuel	1.18 g/s
Limiting Current Density ( $j_l$ )	0.7 A/cm <sup>2</sup>
Activation Energy ( $E_a$ )	105 kJ/mol
Activation Energy ( $E_{ac}$ )	110 kJ/mol
Thickness ( $\delta_c$ )	0.22 cm
Thickness ( $\delta_a$ )	0.01 cm
Thickness ( $\delta_e$ )	0.004 cm
Conductivity ( $\kappa_c$ )	76.9 $\Omega^{-1} - cm^{-1}$
Conductivity ( $\kappa_a$ )	0.33e6 $\Omega^{-1} - cm^{-1}$
Conductivity ( $\kappa_e$ )	20500e(-9030/T)) $\Omega^{-1} m^{-1}$
Pre-exponential Factor (cathode)	7e8 A/m <sup>2</sup>
Pre-exponential Factor (anode)	4.2e10 A/m <sup>2</sup>
Fuel Utilisation Factor	0.85

Table A.1: Input values for the 0-D model

### Pressure Variation

The model was kept at a constant temperature of 1000 °C. The I-V characteristics were noted at 3 different pressures; 1 atm, 3 atm and 5 atm. The area was set to 570 cm<sup>2</sup>. The experimental curves are marked *exp*.

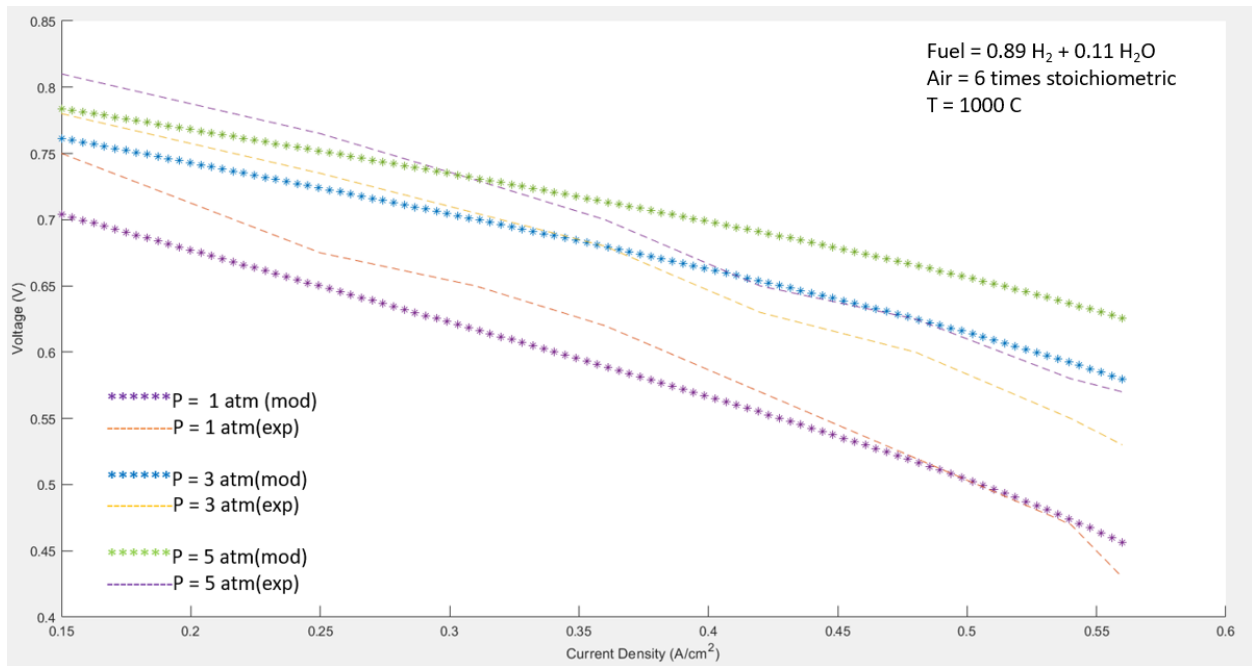


Figure A.1: SOFC I-V curves - pressure variation at a constant temperature. The experimental curves are marked *exp* and the modelled curves are marked *mod*.

From the graph shown above, it can be observed that the voltage of the SOFC increases at higher pressures. This is expected as the partial pressure of the reactants increases, increasing the Nernst Potential ( $E_{nernst}$ ) as explained in earlier Section 2.2.4. The I-V trend predicted by the model is in line with the experimental SOFC data from [46]. The slight differences in the predicted voltages and the actual results are due to the 0-D nature of the model. The Nernst potential of the cell decreases towards the outlet due to the decrease in the partial pressure of the reactants. This variation in pressure is not captured by the 0-D model as it takes only one fixed pressure value. Here the partial pressure of the gasses have been taken at the outlet, where the Nernst Potential will be the lowest. Therefore, the predicted value of the Nernst voltage is slightly lower than the actual value.

### Temperature Variation

The data for operation on constant pressure was available for a variant of the original Siemens Westinghouse SOFC. The area was changed from 570 cm<sup>2</sup> to 95 cm<sup>2</sup>. Air was set to 4 times the stoichiometric amount in line with the experimental data from [46]. The model was kept at a constant pressure of 1 atm. The I-V characteristics were noted at 3 different temperatures; 900 °C, 950 °C and 1000 °C.

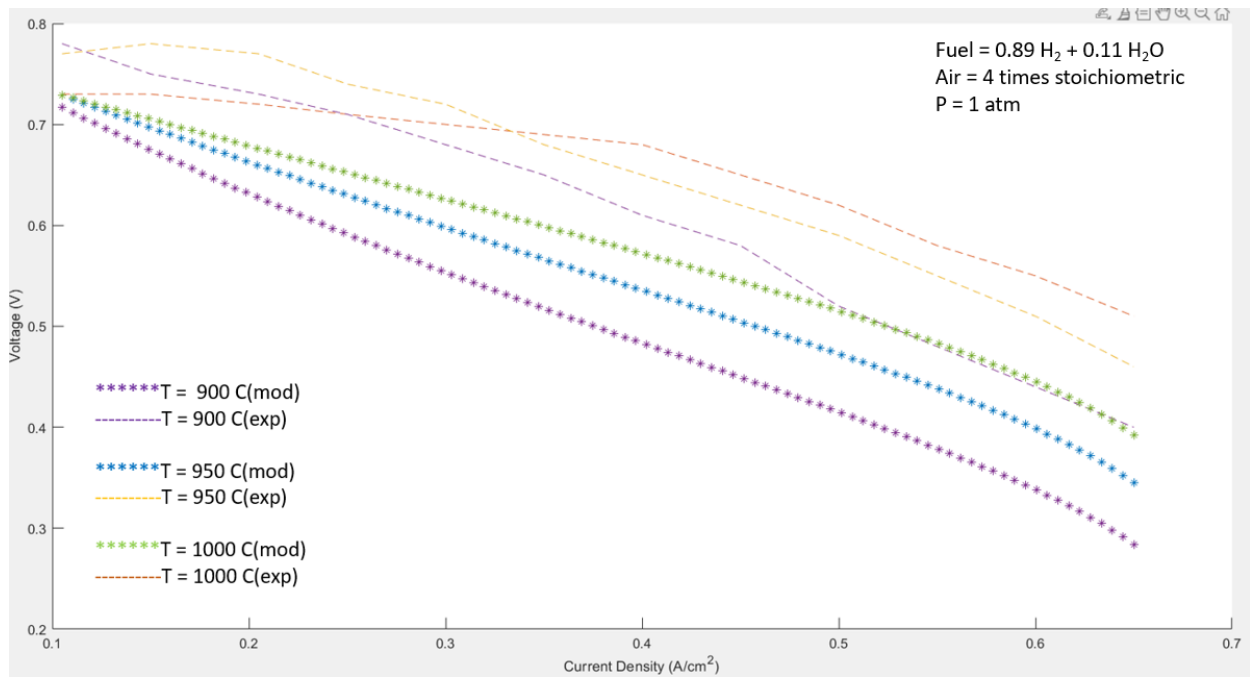


Figure A.2: SOFC I-V curves - temperature variation for a constant pressure. The experimental curves are marked *exp* and the modelled curves are marked *mod*.

From the above graph, it can be observed that even though the general trend of the predicted I-V curve is the same as the experimental values and is in line with the general expectations (refer Section 2.2.4), the predicted cell voltages are slightly lower. The reason for this is the same as explained above.

From these curves it can be said that the 0-D model predicts the output voltage under different conditions of pressure and temperature reasonably accurately.

